Interconversion of Nickel Hydroxides Studied using Dynamic Electrochemical Impedance

by

Victor Omoatokwe Aiyejuro
B.Sc, University of Ibadan

A Thesis Submitted in Partial Fulfillment of the
Requirements for the Degree of

Master of Science

in the Department of Chemistry

Interconversion of Nickel Hydroxides Studied using Dynamic Electrochemical Impedance

by

Victor Omoatokwe Aiyejuro

B.Sc, University of Ibadan

Supervisory Committee

Dr. D. A. Harrington, Supervisor (Department of Chemistry)

Dr. D. K. Hore, Departmental Member (Department of Chemistry)

Supervisory Committee

Dr. D. A. Harrington, Supervisor (Department of Chemistry)

Dr. D. K. Hore, Departmental Member (Department of Chemistry)

Abstract

The interconversion of α- and β-$Ni(OH)_2$ was studied using cyclic voltammetry and dynamic electrochemical impedance (dEIS). Holding experiments were done at 0.5 V, 0.6 V, 0.8 V and 1.0 V while subsequent cathodic holds were applied in selected experiments at -0.1, -0.2, -0.25 V. The number of thickness of $Ni(OH)_2$ formed increased with increasing anodic potential.

After α-$Ni(OH)_2$ was formed (< 0.5 V), it was easily reduced by sweeping down to -0.15 V. However, sweeping further (> 0.5 V) resulted in its "irreversible" conversion to β-$Ni(OH)_2$. Since β-$Ni(OH)_2$ was not reduced by sweeping to -0.15 V, the current, capacitance and the conductance at the α-$Ni(OH)_2$ peak (at 0.2 V) decreased as a result.

However, β-$Ni(OH)_2$ was shown to be reducible during potential holds at -0.2 V or lower. In contrast, holding at -0.1 V only resulted in partial reduction. Eventually, a link was established between the reduction of β-$Ni(OH)_2$ and hydrogen evolution. The relatively slow reduction of the β-$Ni(OH)_2$ to metallic nickel appears to inhibit the capacitance increase at -0.15 V which occurs when the potential is kept under 0.5 V. The retention of a low capacitance while β-$Ni(OH)_2$ persists suggests a blocking mechanism. A concerted adsorption-desorption step which generates adsorbed hydrogen prior to hydrogen evolution was proposed.

An exponential increase in current and capacitance occurred during the potential hold at -0.2 V. The capacitance increase suggests a reversal of the blocking (low

capacitance at -0.15 V) caused by the persistence of β-Ni(OH)$_2$.

Additionally, the exponential current decay during the hold at -0.2 V was significantly slower than the conversion of α- to β-Ni(OH)$_2$ at 0.8 V. This further demonstrates the possibility of a slow step involving surface blocking during the reduction of β-Ni(OH)$_2$.

These observations provide new information on the mechanism and kinetics of the interconversion of α-Ni(OH)$_2$ into β-Ni(OH)$_2$ and the interaction of the latter in the hydrogen evolution reaction.

Table of Contents

List of Tables

List of Figures

Nomenclature

Symbol	Meaning	Units
C	Capacitance	F cm^{-2}
C_{dl}	Double layer capacitance	F cm^{-2}
E	Potential	V
f	Frequency	Hz
I	Current	A
j	Current density	A cm^{-2}
Q	Charge	C
R_{ct}	Charge transfer resistance	Ω cm^2
R_{ct}^{-1}	Conductance	S cm^{-2}
$R_{\|\|}$	Parallel combination of resistance	Ω cm^2
R_p	Polarization resistance	Ω cm^2
R_s	Solution resistance	Ω cm^2
t	Time	s
τ	Time constant	s
v	Potential sweep rate	V s^{-1}
w	Statistical weights	S^2 cm^{-4}
Y	Admittance	S cm^{-2}
Z	Impedance	Ω cm^2
Z_{imag}	Imaginary part of impedance	Ω cm^2
Z_{Re}	Real part of impedance	Ω cm^2

Acronym	**Meaning**
AC	Alternating current
AIC	Akaike information criterion
AICc	Akaike information criterion corrected for small sample size
CNLS	complex nonlinear least squares
CPE	Constant phase element
CTR	Crystal truncation rod
DC	Direct current
dEIS	dynamic electrochemical impedance
ECSA	Electrochemically active surface area
EIS	Electrochemical impedance spectroscopy
EQCM	Electrochemical quartz crystal microbalance
EXAFS	Extended X-ray Absorption fine structure
FFT	Fast Fourier transform
HER	Hydrogen evolution reaction
IR	Infrared
KCL	Kirchoff's current law
KVL	Kirchoff's voltage law
KK	Kramers Kronig
Min.	minimum
OER	Oxygen evolution reaction
RHE	Reversible hydrogen electrode
RMS	Root mean square
TGA	Thermogravimetric analysis
XPS	X-ray photoelectron spectroscopy
XRD	X-ray diffraction

Acknowledgements

I thank my supervisor, David A. Harrington. You challenged me to learn and to grow throughout. I did not always understand, but you were ever the patient teacher. I appreciate the opportunity you gave me three years ago. More so, I appreciate the skills and the lessons I take with me now.

I thank Nickel ElectroCan, MEET-CREATE and the Canada-Norway Partnership in Electrochemical Energy Technologies (CANOPENER) for funding my research.

I thank my coworkers Tianyu, Tory, Mohammad and Natalie for sharing their knowledge. I also thank my buddies, Dare, Braydon, Marc, Manan and Alex. I'm proud of you boys and the strides we've made separately and together in the last few years.

Lastly, I thank the most important people in my life. My parents, Samson and Christianah Aiyejuro, who have supported me through the years. My father for being a stellar example of hardwork and dedication. My mother, for teaching me to persevere. I thank my sister, Francisca, for the never-ending stories of home. You made the seven thousand miles between Lagos and Victoria a lot less daunting. I thank my girlfriend, Abisoye. Your unwavering belief in me is considered weird on this planet. I love you very much.

To my Dad, my Mom and Francisca.

Chapter 1

Introduction

1.1 Background

Nickel hydroxides are important components of the surface layers which form either electrochemically or by corrosion at nickel and its alloys [1]. Since 1887 when nickel hydroxides were first suggested for use as cathodes in alkaline batteries, interest in the electrochemical activity of these unique materials has only intensified [2, 3]. Today, these materials are used as cathodes in nickel-cadmium (Ni/Cd), nickel-metal hydride (Ni-MH), nickel-iron (Ni/Fe) and nickel-zinc (Ni/Zn) batteries and are also used as nickel sources in the production of cathodes for lithium ion batteries [2–5]. Nickel hydroxides are good battery materials because their layered structure allows for fast intercalation of ions and consequently the storage of energy. Nickel-based batteries deliver high energy density and good cyclability at relatively low cost [5]. Additionally, nickel hydroxides have been keenly researched for use in supercapacitors [6–8], photocatalysis of water splitting [9,10] and electrochromic devices [11]. Needless to say these materials have been studied significantly in the last 130 years.

Here, the interconversion of nickel hydroxides is studied using dynamic electrochemical impedance (dEIS). Later in this chapter, the scope and relevance of this

work is discussed. Research questions are also proposed which seek to fill the gap in the understanding of the kinetics of the interconversion of nickel hydroxides. In chapter 2, the literature evidence for the components of the oxide/hydroxide layer formed at nickel during its electrooxidation are reviewed. Chapter 3 introduces dynamic impedance and the conditions necessary for obtaining valid data using the technique. In chapter 4, the fastest time constant which may be measured during a potential hold using the dEIS instrumentation in the 1 Hz to 13 kHz frequency range is investigated. In chapters 5 and 6 the interconversion of nickel hydroxides is studied using dEIS. In chapter 7, the major conclusions drawn from the investigation of the research questions are presented. The conclusions of this work show that dEIS provides information about the interconversion of $Ni(OH)_2$ which may not be obtainable elsewhere.

While the focus of this work is on the nickel hydroxides, it is worth mentioning that nickel converts to oxides, hydroxides and oxyhydroxides during its electrooxidation. The work described later in chapters 5 and 6, relies on an understanding of the interconversion of these species at nickel. Fig. 1.1 shows the species formed during the electrooxidation of nickel and the potentials where they interconvert. Fig. 1.2 is a typical cyclic voltammogram obtained under the conditions of this thesis that shows the reactions characteristic for the interconversion of the surface species at different potentials. This work focuses on the nickel hydroxides ($Ni(OH)_2$) which are formed during the initial stages of nickel electrooxidation. There are two well defined phases of $Ni(OH)_2$, the α- and β-$Ni(OH)_2$. Bode et al. first demonstrated the existence of these phases [12] and their work eventually led to the development of redox schemes such as fig. 1.1, which explain the redox behavior (fig. 1.2) of nickel hydroxides.

Crystallographic analysis shows that the α-species, $Ni(OH)_2.xH_2O$ ($0.41 \leq x \leq 0.7$), is elongated along the hexagonal c-axis due to the intercalation of water and cations [1, 12, 13, 19–21]. In β-$Ni(OH)_2$, most of the intercalated water is lost leading to less turbostraticity (misalignment of the basal planes in the crystal structure)

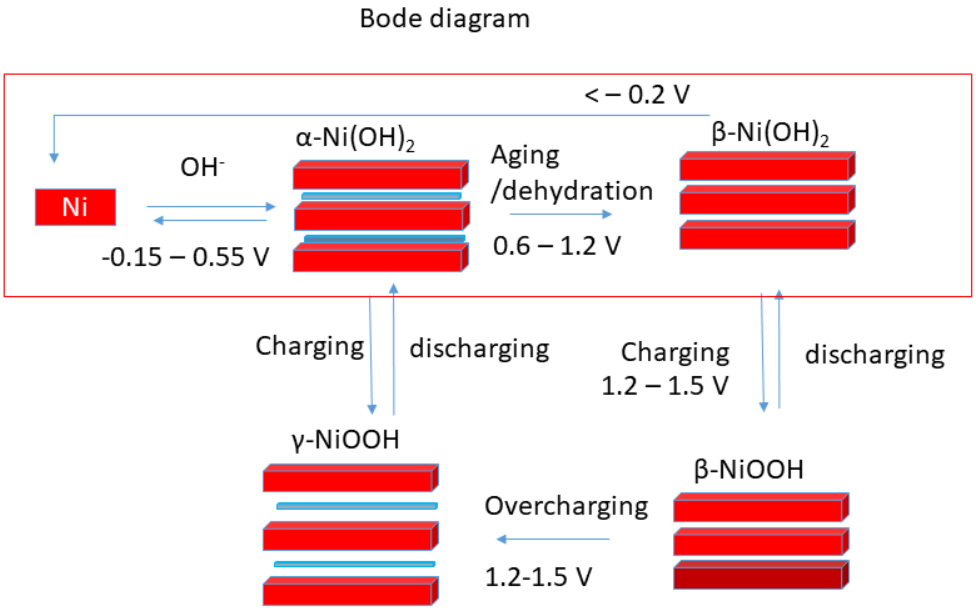

Figure 1.1: Schematic showing the hydroxide and oxyhydroxide phases generated during Ni electrooxidation [12–18].

and much better crystallinity [1, 13, 16]. However, these polymorphs are not just structurally different. In Ni-MH batteries for example, the α-Ni(OH)$_2$ / γ-NiOOH positive electrode is preferred because of its high discharge capacity compared to the β-Ni(OH)$_2$ / β-NiOOH couple [22]. Separately, Gao et al. demonstrated that α-Ni(OH)$_2$ is a highly active and durable catalyst for water splitting (oxygen evolution reaction-OER) which performs favourably compared to the state-of-the-art catalyst Ru_2O and outperforms β-Ni(OH)$_2$ [10]. However, of the two nickel hydroxide polymorphs, β-Ni(OH)$_2$ is significantly more active for hydrogen evolution than α-Ni(OH)$_2$ [23–26].

Hence, mechanistic understanding of nickel hydroxide redox behavior is especially important because of the distinct activities associated with each of its phases and is crucial as further applications are found.

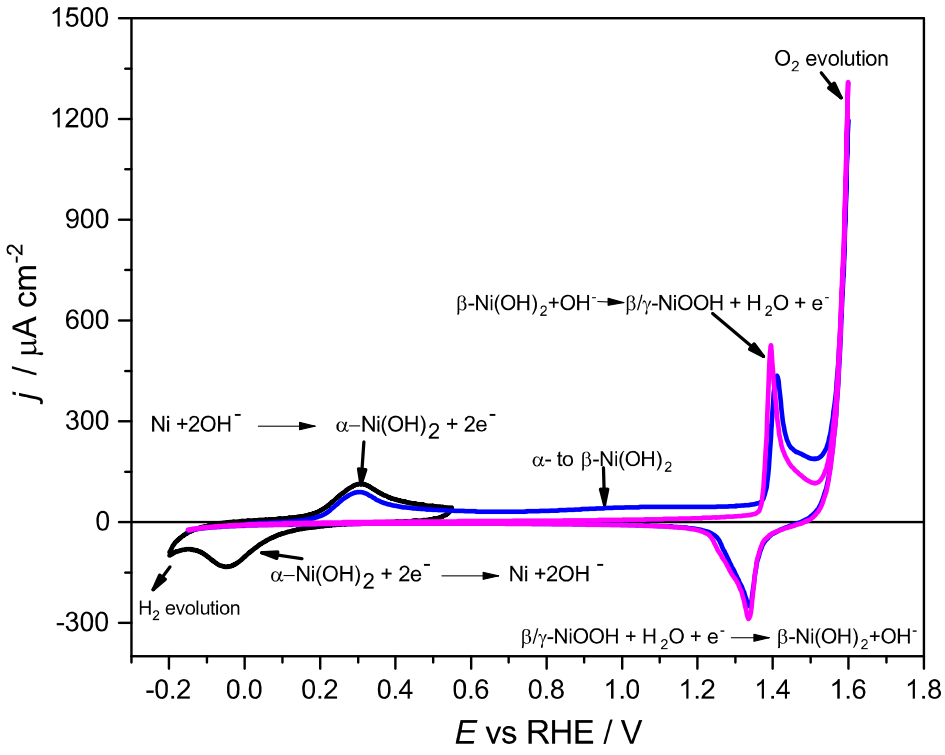

Figure 1.2: Typical voltammogram showing Ni electrooxidation in 0.5 M KOH at 50 mV s^{-1}. Black: -0.2 to 0.55 V. Blue: -0.15 to 1.6 V (first cycle). Magenta: -0.15 to 1.6 V (2nd cycle). Obtained under the conditions described in chapter 5.

1.2 Scope and relevance of this work

This work studies the interconversion of the nickel hydroxides using dynamic electrochemical impedance (Red box in fig. 1.1). Dynamic electrochemical impedance allows the behavior of the surface oxide to be characterized under pseudosteady state conditions. In this technique, impedance may be measured continuously during a slow potential sweep [27–29]. Here, the method is extended to measurement during potential hold periods. The application of dEIS in this way is new, hence, the technique is initially validated on model circuits containing standard components in order to ascertain the fastest time constants which may be measured. Subsequently, the interconversion of $Ni(OH)_2$ is studied.

The α–$Ni(OH)_2$ species is often short-lived in alkaline solution because it is irreversibly converted to β-$Ni(OH)_2$ once potential > 0.5 V is applied or by spontaneous aging in alkali [25, 30–35]. This transformation between 0.5 V and 1.2 V is characterized by a small current ("featureless" plateau, fig. 1.2), which may be difficult to measure accurately. This renders its kinetics inaccessible to techniques such as cyclic voltammetry [35–37]. Hence, the kinetics of α- to β-$Ni(OH)_2$ interconversion is still largely unstudied. Nonetheless, in situ EQCM [14, 38, 39], XPS [17, 37, 40], EXAFS [19], ellipsometry [41, 42] and vibrational spectroscopy (IR and Raman) [13, 43–47] have been used to characterize the $Ni(OH)_2$ polymporphs as they form. Separately, the kinetics of hydrogen evolution at nickel has been studied in great detail using electrochemical impedance spectroscopy (EIS) [48–52], linear sweep voltammetry [53] and cyclic voltammetry [24, 54]. The latter showed that β-$Ni(OH)_2$ catalyzes hydrogen evolution and is reduced in the process.

However, despite the agreement in the literature that the reduction of β-$Ni(OH)_2$ is slow [32, 55, 56], no time constants have been suggested. In this work, the impedances acquired over the region of interest (-0.25 V to 1.4 V) have been analyzed using equivalent circuits. Comparing the impedance spectra as the potential is slowly

changed allows the changing state of the surface species to be captured. The values of the parameters extracted (capacitance and charge transfer resistance) are related to the kinetics of the interconversion of α- and β-$Ni(OH)_2$. Crucially, time constants associated with the surface processes which occur at nickel electrodes during the inital stages of electrooxidation are extracted for the first time.

1.3 Research questions

In this work, the interconversion of nickel hydroxides is studied using dEIS. The following questions are investigated:

1. Can the conversion of α- to β-$Ni(OH)_2$ be monitored by holding at potentials between 0.6 V and 1.0 V? The technique, dEIS, gives both EIS and cyclic voltammetry data. In the literature, this system is studied predominantly using cyclic voltammetry. However, impedance obtained during the potential hold may give information about the changing state of the surface species which might otherwise be missed if cyclic voltammetry alone were used.

2. Can the mechanism of β-$Ni(OH)_2$ reduction be studied? The reduction of β-$Ni(OH)_2$ is known to be slow from the literature. However, in this work, the conditions necessary for its reduction will be investigated. Additional features which may be gleaned from the impedance may offer insight into the mechanism of reduction of β-$Ni(OH)_2$.

3. Can time constants related to the kinetics of nickel hydroxides interconversion be extracted? Time constants have not been previously reported in the literature for this system. However, in this work, impedance spectra and current decays are collected during the potential holds using dEIS. In principle, time constants may be obtained from both methods.

Chapter 2

Literature review

In this chapter, the literature evidence for the components of the oxide/hydroxide layer formed during the electrooxidation at nickel are reviewed. These components were studied using spectroscopic and surface analysis techniques. The literature reviewed here also covers the interconversion of the surface species. Additionally, the methods of determining the electrochemically active surface area (ECSA) of nickel electrodes are reviewed as a prelude to the discussion which appears in section 6.2.7.

2.1 Stages of Ni oxidation in alkali

The adsorption of hydroxyl ions (OH^-) occurs in the early stages of the anodic sweep [34, 57]. This eventually results in the conversion of metallic nickel to α-$Ni(OH)_2$, for which the peak between 0.2 and 0.5 V is observed [15,25,31,32,34–36,54]. The peak may also contain additional current as a result of hydrogen desorption [15, 23–25, 54, 57–61]. The contribution of this side reaction may be minimized by increasing the scan rate to 100 mV s^{-1} [32,36]. The α-$Ni(OH)_2$ formed reduces back to metallic nickel on the reverse sweep at -0.15 ± 0.05 V as long as the upper limit of potential is kept under 0.5 V [15, 32, 34–36].

However, between 0.6 and 1.2 V, α-$Ni(OH)_2$ is converted to the β by aging or dehydration [25, 30–35]. Over the same potential range metallic nickel may also be oxidized to NiO [17,37,40,41,43,62,63]. This region is characterized by a small, nearly constant current plateau which is often described as featureless [35–37]. However, a second look at literature shows that a small peak may be observed at 0.8 ± 0.1 V [37, 59, 64–66]. The nature of the species whose oxidation that peak represents remains unknown.

Although metallic nickel is typically passivated by NiO on exposure to air or oxygen, pretreatment of the electrode by etching or by holding the potential at -0.2 V in alkali minimizes the passivation by NiO [43, 67]. However, Alsabet et al. observed the emergence of a second cathodic peak between -0.2 and 0.5 V on increasing scan rate from 5 to 500 mV s^{-1} which they assigned to NiO [36]. Hence, it may be concluded that passivation of the nickel substrate by NiO continues over the 0 to 0.5 V range [36, 40, 41, 43, 61]. Available data is inconclusive on whether NiO oxide forms independently [37, 40] or by dehydration of $Ni(OH)_2$ during the anodic sweep [41]. Nonetheless, it has been suggested that $Ni(OH)_2$ forms first [41,43,58,64]. Afterwards, the NiO inner layer is formed at more positive potentials by dehydration of $Ni(OH)_2$ [41, 43, 58]. Other authors have suggested that air-formed NiO converts to $Ni(OH)_2$ on immersion in 1 M KOH at open circuit potential [17]. In fact Visscher suggested that the NiO is only converted to β-$Ni(OH)_2$ at 1 V [64].

Sweeping to higher anodic potentials between 1.2 and 1.5 V results in the formation of β- and γ-NiOOH species [32]. Typically, β-$Ni(OH)_2$ is oxidized to β-NiOOH. However, slower sweep rates enable the reintercalation of water in the intersheet space which results in the formation of γ-NiOOH [32]. The valency of these oxyhydroxides depends on the degree of structural disorder induced by intercalation of water, cations (e.g K^+) and H^+ [57]. Nickel atoms attain oxidation states between 3-3.75 in the γ-NiOOH species due to presence of Ni^{3+} and Ni^{4+} [13, 18, 22, 68–70]. For β-NiOOH, average oxidation state of nickel is 2.7-3.1 [18, 69]. Additionally, the NiOOH phases

may also be formed by oxidation of NiO (eq. 2.1) [40,41,71,72]. The γ- and β-NiOOH species are not discussed further as they are out of the scope for this work.

$$NiO + OH^- \rightarrow NiOOH + e^- \tag{2.1}$$

2.2 Characterizing the oxide / hydroxide film

2.2.1 X-ray photoelectron spectroscopy

X-ray photoelectron spectroscopy (XPS) can be used for compositional analysis of thin oxide / hydroxide films deposited during the oxidation of nickel [73]. The thickness and oxidation state of the species making up these films have been widely analyzed [40,73–77]. Typically, NiO and $Ni(OH)_2$ can be differentiated by comparing the binding energies at which Ni 2p and oxygen 1s peaks occur in the spectra [37,77]. The peak at 531.8 eV is characteristic for OH bound to a Ni substate [37,74]. It has also been assigned to oxygen atoms occupying positions adjacent to nickel vacancies in the oxide structure [73]. The peak at 529.3 eV is due to O^{2-} from NiO [37,73,74]. Both peaks have been observed for oxide films grown on nickel in oxygen at room temperature [74]. When NiO and $Ni(OH)_2$ are present, the oxygen 1s spectrum shows two peaks at 531.8 ± 0.4 eV and 529.3 ± 0.5 eV [37,73]. However, when $Ni(OH)_2$ is present without NiO contamination, only the peak at 531.8 eV is observed [73].

In the case of Ni 2p, the spin-orbit peaks, $2p_{\frac{3}{2}}$ and $2p_{\frac{1}{2}}$, are observed [37,77]. Since $2p_{\frac{3}{2}}$ is typically higher in intensity for nickel compounds, it is predominantly analyzed in XPS spectra [37,40,74–77]. However, when Ni^0 is present, the $2p_{\frac{1}{2}}$ from the metal overlaps with the satellite structures / shoulders of the NiO and $Ni(OH)_2$ $2p_{\frac{3}{2}}$ peaks [73,77]. Where such overlap occurs, correction for the spectral background

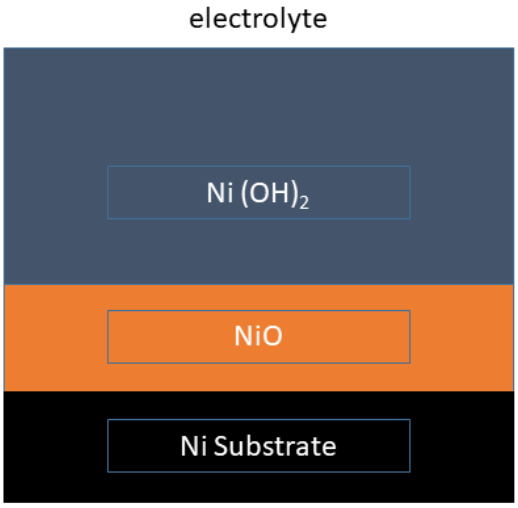

Figure 2.1: Schematic showing the composition of oxide film formed on nickel substrate in air and alkali.

may be problematic [73, 77].

Metallic nickel is typically passivated by NiO on exposure to air or oxygen [74]. It also forms a protective barrier when nickel is immersed in acid or alkali [74]. Kitakatsu et al. found that exposure of Ni(111) to 25 L of oxygen at a rate of 1.3×10^{-9} bar / second at 300 K resulted in the formation of 3 to 4 monolayers of NiO [74]. A top layer of 0.85 ± 0.1 monolayers of β-Ni$(OH)_2$ was also found. In their spectra, a peak at 858.5 ± 0.1 eV corresponding to metallic nickel was reported. They also identified a doublet at 854.1 ± 0.1 eV and 855.9 ± 0.1 eV which they assigned to Ni^{2+} in NiO. They found a peak at 856.0 ± 0.1 eV which they assigned to Ni$(OH)_2$ [74].

Exposure of Ni(111) to 1 M KOH at open circuit potential leaves only 1-2 monolayers of NiO(111) [17]. Medway et al. surmised that the thickness of the NiO film formed in air decreased once the surface was exposed to 1 M KOH. They theorized that NiO was being converted to Ni$(OH)_2$ [17] (fig. 2.1). They also found that the thickness of the NiO and Ni$(OH)_2$ layers increased simultaneously when the poten-

tial was cycled into the oxyhydroxide region [17]. Separately, it was concluded that although $Ni(OH)_2$ formed instantaneously at open circuit, further growth could be inhibited by holding at negative potentials [17]. However, Hoppe et al. found that once the barrier-like NiO was formed at potentials between 0.4 V and 1.2 V, it could not be completely reduced by applying potentials in the range of hydrogen evolution. Instead, it was thinned by conversion to $Ni(OH)_2$ [40].

Alsabet et al. studied the oxide film formed when polycrystalline nickel was polarized at 1.2 V for 2700 s in 0.5 M KOH at 298 K. At this potential NiO and β-$Ni(OH)_2$ develop [37]. They found two well defined Ni $2p_{\frac{3}{2}}$ peaks at 856.3 ± 0.3 eV and 862.3 ± 0.3 eV and a small shoulder at 853 eV [37]. They found one oxygen 1s peak at 531.8 ± 0.4 eV which is characteristic for hydroxylated nickel as described earlier. In addition to XPS, argon ion sputtering was used for analysis of thickness and oxide composition as a function of depth. The distinction between NiO and β-$Ni(OH)_2$ was established by determination of oxygen to nickel ratio (N_o / N_{Ni}) as a function of depth [37]. A large value was found at the top which they ascribed to a predominantly β-$Ni(OH)_2$ layer. The smaller value of N_o / N_{Ni} as they etched further meant NiO had become more abundant. The growth of the Ni^0 peak at 852.8 ± 0.1 eV was used as an indicator that the Ni substrate had been reached [37].

Raman and infrared spectroscopy

In situ surface-enhanced Raman spectra typically show bands around 450 cm^{-1}, 3630 cm^{-1} (sharp) and 512 cm^{-1} which are associated with Ni-OH symmetric stretch, non-hydrogen bonded OH and NiO stretch respectively [13, 43–47]. Separately, the peak around 510 cm^{-1} has been assigned to OH rotation [44]. Nonetheless, it has been described as diagnostic for the crystallinity of β-$Ni(OH)_2$ [44,47]. A peak at 310 cm^{-1} is ascribed to a Ni-OH lattice vibration [47]. Typically, the OH stretch is broad for α-$Ni(OH)_2$ and appears around 3450 cm^{-1} instead [13, 45].

Melendres et al. showed that nickel substrates could be precleaned by holding at -0.2 V for 15 minutes and 0 V for 1 h in 0.1 M NaOH without the formation of discernible oxide or hydroxide bands [43]. However, sweeping the potential to 0.25 V coincided with the emergence of Ni-OH and OH stretching bands at 450 $cm^{-1}$and 3630 cm^{-1} respectively [43]. Further sweeping the potential to 0.65 V coincided with the emergence of a peak at 512 cm^{-1} which they assigned to NiO [43]. Additionally, they found that the intensities of the Ni-OH and NiO bands increased as the potential was swept to 1 V. However, on reversal of the potential scan and holding at 0.15 V for 2 h, the intensity of the peaks at 450 and 510 cm^{-1} decreased due to the reduction of the surface oxide species, but did not disappear completely [43]. This was probably because they did not sweep far enough to reduce the α-$Ni(OH)_2$ (-0.15 ± 0.05 V). Nonetheless, they deduced that the kinetics for the reduction reaction was either slow or irreversible [43].

For the α-species, broad OH stretching vibrations occur around 640 and 470 cm^{-1} as a result of extensive hydrogen bonding with intercalated water molecules in infrared spectra. Additionally, strong absorptions between 1600 and 1000 cm^{-1} occur due to intercalated anions [78]. Several bands between 1600 and 1000 cm^{-1} may also occur in α-$Ni(OH)_2$ due to intercalated ions such as CO_3^{2-} and NO_3^- [13, 44, 78].

Overall, characterization of surface passivating films on nickel using vibrational spectroscopy based techniques such as Raman and IR can be complicated by the diversity of $Ni(OH)_2$ phases [55, 78].

2.2.2 X-ray crystallography

NiO and α- or β-$Ni(OH)_2$ may co-exist. When NiO is present, its considerably smaller interlayer spacing of 2.41 Å would be evident [17]. Furthermore, compared to the hexagonal structure adopted by α- and β-$Ni(OH)_2$, the NiO unit cell is typically cubic ($a = 4.1798$ Å) [71]. However, Hotovy et al. found that the NiO cubic cell was

distorted to a hexagonal structure when annealed at 700 °C in air [79].

Rajamathi et al. characterized an intrastratified $\alpha\beta$-$Ni(OH)_2$ pseudophase [78]. For this intermediate phase, interlayer spacings of 5.4-5.6 Å have been observed [78]. Kim et al. found that aging α-$Ni(OH)_2$ to β in 6 M KOH at 70 °C produced peaks associated with both polymorphs in the diffraction pattern [80].

Medway et al. characterized their oxide films by modeling low angle X-ray scattering and crystal truncation rod (CTR) data [17]. They observed that the presence of NiO contributed asymmetric scattering which suggested that the oxide film was either poorly ordered or being hydrolyzed to $Ni(OH)_2$ [17]. The data was fitted to models with different refractive indices which allowed the determination of mass density, layer thickness and interfacial roughness of the oxide / hydroxide film [17]. They deduced from the interfacial roughness that Ni was being transported across the Ni/NiO interface to the hydroxide film during the growth of NiO and $Ni(OH)_2$ [17].

Structural comparison of α- and β-$Ni(OH)_2$

The β phase is typically more crystalline, consisting of hexagonal layers of nickel atoms with oxygen atoms occupying octahedral sites (3 above and 3 below the plane), in an ABAB pattern [19, 39]. Ideally, protons occupy the tetrahedral sites above or below the oxygen atoms in the interlayers leaving the OH bonds parallel to the c-axis [19, 47] (fig. 2.2). In addition, water molecules and/or ions are intercalated between these sheets in the α phase [19]. For β-$Ni(OH)_2$, these slabs of nickel hydroxide are well ordered along the hexagonal c-axis.

The α phase is turbostratic since the basal planes are inherently misaligned (fig. 2.3).Its c lattice parameter can range from 7 Å to 8.5 Å depending on the packing density of the intercalated water, thermal history of the material and the presence of other ions in the interlayer space [1, 13, 21, 81]. However, it contracts by about 0.05 Å ($a = b = 3.08$ Å) in the ab direction relative to the idealized β species [1, 19, 21, 81].

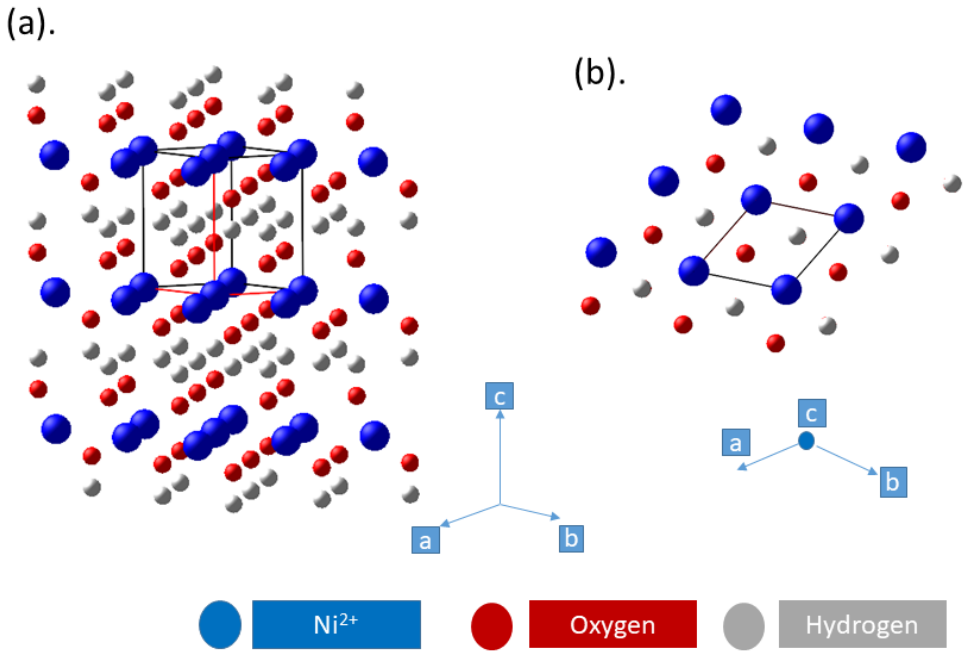

Figure 2.2: Idealized crystal structure for β-Ni$(OH)_2$. (a) ball and stick unit cell, (b) unit cell projection.

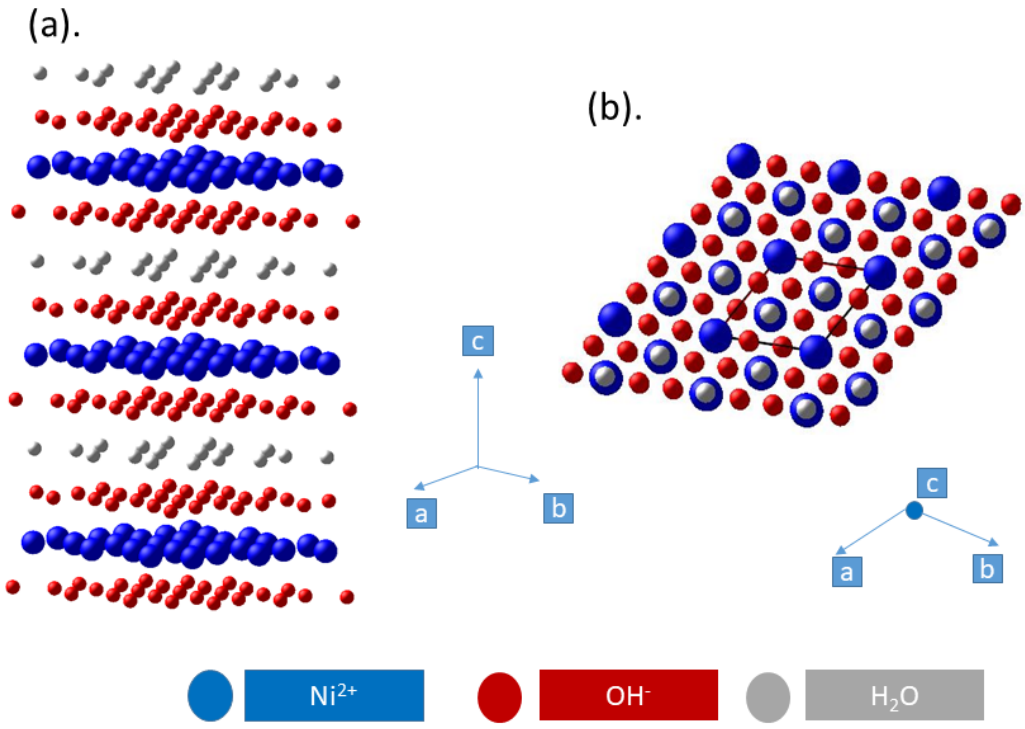

Figure 2.3: Idealized α-Ni$(OH)_2$.0.67H_2O crystal structure. (a) Layers, (b) Unit cell projection.

Note that in the representation shown in figs. 2.3 and 2.2, the a/b lattice parameter corresponds to the Ni-Ni intrasheet distance while the c parameter is the distance between the $Ni(OH)_2$ layers [13].

Ideally, well ordered β-$Ni(OH)_2$ is attainable by thermal treatment of as-prepared materials to remove interslab water and ions [1,82]. For this material, the hexagonal unit cell dimensions, $a = b = 3.126$ Å and $c = 4.605$ Å (space group: trigonal $P\bar{3}m1$, symmetry point group: D^3_{3d}) , apply [1, 19, 21, 44, 46, 82, 83]. However, aging or electrochemical conversion of α- to β-$Ni(OH)_2$ forms interstratified (mixed $\alpha\beta$) pseudophases due to progressive removal of intercalated species [45, 70, 81, 84–88]. The formation of this mixed phase during α- to β-$Ni(OH)_2$ transformation has been ascribed to a dissolution-reprecipitation mechanism [78, 81].

Thermogravimetric analyses (TGA) on such materials shows mass loss corresponding to residual intercalated (or adsorbed) water around 160 °C (eq. 2.2) [13,46,86,89]. Without intersheet water molecules, dehydration of β-$Ni(OH)_2$ begins around 200 °C (eq. 2.3) [13, 46]. Consequently, non-native stacking fault disorders may occur in β-$Ni(OH)_2$ as in the α phase [88,90]. Intermediate c spacing of 5.7 Å to 6.3 Å has been observed in literature [78, 89]. While it is difficult to ascertain the relative content of the β phase on electrodes aged or electrochemically converted from the α phase, slower scan rates and higher potentials favour the conversion to β-$Ni(OH)_2$ [45, 88]. For simplicity, the $Ni(OH)_2$ phase formed by holding at potentials between 0.6 to 1.2 V in this work will be referred to as β-$Ni(OH)_2$.

$$Ni(OH)_2.xH_2O \rightarrow Ni(OH)_2 + xH_2O \tag{2.2}$$

$$Ni(OH)_2 \rightarrow NiO + H_2O \tag{2.3}$$

2.2.3 Ellipsometry

This technique allows the dielectric properties of thin oxide films to be studied [57, 91]. Ellipsometric measurements by Kudryatseva et al. showed that a $Ni(OH)_2$ layer persists during an anodic sweep from 0.3 V to 1.35 V in 0.1 M KOH and thickens to about 20 Å corresponding to 2.5 to 3 monolayers [60]. Visscher et al. found that the refractive indices of α- and β-$Ni(OH)_2$ were $1.41 \pm 0.03 - 0i$ and $1.46 \pm 0.03 - 0i$ respectively at 546.1 nm [91]. Separately, Hopper et al. found that the real parts of the refractive indices for α- and β-$Ni(OH)_2$ are 1.52 and 1.46 respectively at 632.8 nm [30].

Paik et al. ascribed the small refractive index values between 2 and 2.5 to the presence of NiO [41]. By monitoring the changes in refractive index and and extinction coefficient with respect to time and potential, they deduced that the $Ni(OH)_2$ layer was being gradually dehydrated to NiO in the oxyhydroxide region [41]. Comparison of the relative reflectance of the film after application of passivating potential between 0.6 V and 1.4 V in 0.1 M NaOH showed that NiO film could not be reduced by cathodic treatment [41]. The reflectance never returned to its initial value [41].

2.2.4 Electrochemical quartz crystal microbalance

Electrochemical quartz crystal microbalance (EQCM) is a powerful in situ technique which is capable of monitoring changes in the mass of an electrode. It allows the monitoring of surface film formation and kinetic events at the monolayer level [61, 72, 80]. Kim et al characterized the mixed $\alpha\beta$ pseudophase formed when α-$Ni(OH)_2$ was aged in 6 M KOH at 70 °C for 30 minutes to 4 hours using EQCM [80]. They studied the change in mass and cyclic voltammograms of aged α-$Ni(OH)_2$ as a function of potential during cyclic potential sweeps between 1.2 and 1.5 V in 1 M KOH [80]. The mass change for these electrodes was also compared to that of a macroscopic mixture of α- and β-$Ni(OH)_2$ [80]. They concluded that since no inde-

pendent α - or β-Ni(OH)$_2$ behaviour was observed, the film formed was a separate intermediate phase [80].

Grden et al. found that prolonged potential holds at 0 V in 0.1 M NaOH resulted in higher oxidation charge and an accompanying decrease in mass in the subsequent anodic sweep [61]. The mass loss which results from these holding experiments was ascribed to the slow desorption of hydrogen previously adsorbed during the cathodic sweep [61].

2.3 α- and β-Ni(OH)$_2$ interconversion

Hahn et al. deduced that the electrochemical conversion of metallic nickel to α-Ni(OH)$_2$ between -0.1 V and 1.6 V in 0.1 M NaOH is fast by tracking the evolution of characteristic features for the polymorph using UV-visible reflectance spectroscopy over 350 cycles [55]. After the formation of the α phase, its electrochemical conversion to the β-Ni(OH)$_2$ is slow [32,55,56]. For example, Burke et al. required 60 cycles at 41 mV s^{-1} between -0.5 and 1.55 V (in 1 M NaOH) to achieve significant transformation to β-Ni(OH)$_2$ [32]. Briggs et al. aged freshly deposited α-Ni(OH)$_2$ in water at 100 °C for 18 h to attain complete conversion to the β phase [56].

2.3.1 Relationship between β-Ni(OH)$_2$ reduction and hydrogen evolution

Typically, the accumulation of β-Ni(OH)$_2$ on the substrate results in a decrease in the subsequent anodic charge between 0.2 and 0.5 V (α-Ni(OH)$_2$ region) [24]. However, it can be partially reduced by cycling into the hydrogen evolution region [15,24]. In fact, Burke et al. found that with the lower limit set at -0.3 V, the anodic charge could be recovered for every cycle in spite of an initial anodic sweep up to 1.55 V at 41 mV s^{-1} [32]. However, prolonged hold at negative potentials results in

the adsorption and absorption of hydrogen as well as the emergence of a shoulder at 0-0.15 V in the subsequent slow anodic scan [24, 25, 32, 59]. In an extreme case where the potential was held at -0.15 V for 30 min, most of the α-Ni(OH)$_2$ anodic charge in the subsequent sweep was actually due to hydrogen desorption [15].

Floner et al. noted that contributions from hydrogen desorption were negligible when faster sweep rates of 50 mV s^{-1} were applied [54]. However at 1 mV s^{-1}, the current for the α-Ni(OH)$_2$ peak was much higher [54]. They concluded from the cyclic voltammetric studies that hydrogen desorption was dependent on the onset of OH$^-$ adsorption (eq. 2.7) [54]. Hence, the following mechanism was proposed to account for the increase in current at slow scan rates (eqs. 2.4 - 2.7).

$$2\mathrm{Ni} + \mathrm{H_2} \rightarrow 2\mathrm{NiH(ads)} \tag{2.4}$$

$$\mathrm{Ni} + \mathrm{H_2O} \rightarrow \mathrm{NiOH(ads)} + \mathrm{H^+} + \mathrm{e^-} \tag{2.5}$$

$$\mathrm{NiOH(ads)} + \mathrm{H^+} \rightarrow \mathrm{Ni^{2+}} + \mathrm{H_2O} + \mathrm{e^-} \tag{2.6}$$

$$\mathrm{NiH(ads)} + \mathrm{NiOH(ads)} \rightarrow 2\mathrm{Ni} + \mathrm{H_2O} \tag{2.7}$$

Additionally, the accumulation of β-Ni(OH)$_2$ coincides with an increase in hydrogen evolution activity compared to the α-Ni(OH)$_2$ [24–26]. Choquette et al found that exchange current density increased and charge transfer resistance (R_{ct}) decreased when β-Ni(OH)$_2$ was present on the surface [24]. The increased activity diminishes as the generation of NiOOH commences at 1.6 V due to the latter's poor activity for adsorption of hydrogen [24]. The perceived catalytic activity of β-Ni(OH)$_2$ was lost when the electrode was held at negative potentials [24]. Hence, it was established that β-Ni(OH)$_2$ is reduced during the hydrogen evolution reaction (HER) [25]. The reduction of β-Ni(OH)$_2$ and the regeneration of α-Ni(OH)$_2$ in subsequent cycles coincides with a decrease in hydrogen evolution activity [24]. In general, the mechanism of hydrogen evolution at nickel in alkali has been described as following these three steps: [49, 53, 54, 92]

$$Ni + H_2O + e^- \rightleftharpoons NiH(ads) + OH^- \qquad \text{Volmer} \qquad (2.8)$$

$$2NiH(ads) \rightleftharpoons 2Ni + H_2 \qquad \text{Tafel} \qquad (2.9)$$

$$NiH(ads) + H_2O + e^- \rightleftharpoons Ni + H_2 + OH^- \qquad \text{Heyrovsky} \qquad (2.10)$$

Kreysa et al. found that at high current densities (above 1 A cm^{-2}), the Heyrovsky reaction could be ignored [53]. They concluded that the low activation energy of the forward Tafel reaction indicated that the diffusion of adsorbed hydrogen was the rate determining step in hydrogen evolution [53]. On the other hand, studies on the kinetics of hydrogen evolution at Ni-Al and Ni-Zn electrodes in 1 M NaOH proposed the Volmer-Heyrovsky mechanism [49, 92]. For the latter, the Volmer reaction was suggested as rate determining [49, 52].

2.3.2 Impedance spectra and extraction of capacitance

Lasia and coworkers found only one semicircle in the impedance spectra for Ni-Al electrodes in 1 M KOH at -0.46 V. The impedance was fitted to the circuit in fig. 2.4a [49], where R_s is the solution resistance, C_1 is the double layer capacitance, C_2 is the pseudocapacitance , R_1 is the charge transfer resistance of the electrode, R_2 is referred to as the superficial mass transfer resistance of H(ads) and CPE_1 is a constant phase element (non-ideal capacitor) [48, 52]. A pseudocapacitance arises when adsorption with electron transfer leads to the effective storage of charge, even though there are no actual charges or electric field storing energy at the interface.

If the potential is rapidly stepped by 5-40 mV from steady state to another value, the capacitance of an electrode can be estimated from eq. 2.12 [48, 51, 93]. Hence, capacitance may be obtained as a function of potential [93]. Since the pseudocapacitance becomes negligible at negative potentials, the double layer capacitance (C_{dl})

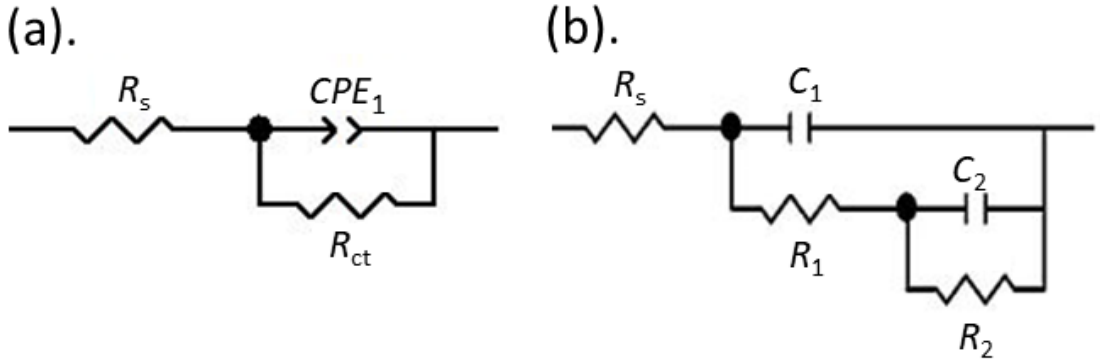

Figure 2.4: Equivalent circuits used for HER at nickel. (a) Model used by Lasia et al. [48], (b) Armstrong and Henderson equivalent circuit [52].

may be deduced [48].

$$Q = \int_0^\infty [(I(t) - I_f]\mathrm{dt} \tag{2.11}$$

$$C = C_{\Phi,\mathrm{p}} + C_{dl} \approx \frac{Q}{E_f - E_i} \tag{2.12}$$

Here $C_{\Phi,\mathrm{p}}$ is the pseudocapacitance, C_{dl} is the double layer capacitance, Q is the charge and E is the potential.

Conway et al. noted that although the same treatment could be applied for oxide films, derivation of capacitance using this method is inherently flawed for systems where thickness and coverage of adsorbed species may change during the potential step [93].

Franscheschini et al. found, while holding a nickel disk electrode at -0.4 V in 1 M KOH, that the initial decrease in current density over the first 100 seconds was followed by a gradual increase [52]. They fitted the impedance spectra to the circuit in fig. 2.4b [52].

Madou et al. observed two semicircles in their Nyquist plot at 1.1 V over a frequency range of 10^{-4} and 10^4 Hz in 0.1 M KOH [62]. At more positive potentials, the

semicircles merged with the Bode plot showing the onset of diffusional processes [62].

2.4 Determination of electrochemically active surface area of nickel electrodes

The measurement of surface area is standard in electrochemistry because it allows the electrocatalytic activity of the material to be assessed and compared [94–96]. Conceptually, the electrochemically active surface area (ECSA) represents the area of the electrode that is accessible to the electrolyte and is available for charge transfer and/or storage [97]. Its value exceeds the geometric area since solid electrodes are typically not smooth [96]. The roughness factor of the electrode is determined by taking the ratio of ECSA to the geometric (projected) area [96].

In general, the methods of determining ECSA have been reviewed by Trasatti et al. and Lukaszewski et al. [94,96]. Some methods of determining the electrochemical surface area of nickel electrodes are discussed next [95].

2.4.1 Cyclic voltammetry

Integration of α-Ni(OH)$_2$ anodic charge

The ECSA can be determined by dividing the anodic charge up to 0.5 V by 514 μC/cm^2 [36]. However, Drunen et al. suggested that contributions by double layer charging could be accounted for by using eq. 2.13 [35]. The uncertainty in the determination of C_{dl} is discussed later.

$$Q = (q_{\mathrm{Ni(OH)_2}} \times \mathrm{A_{ECSA}}) + (C_{\mathrm{dl}} \times \mathrm{A_{ECSA}} \times \Delta E) \tag{2.13}$$

Here Q is the anodic charge for α-$Ni(OH)_2$ integrated up to 0.5 V, $q_{Ni(OH)_2}$ is the charge density associated with one monolayer of α-$Ni(OH)_2$ (514 $\mu C/cm^2$), C_{dl} is the double layer capacitance (usually assumed to be 20 $\mu F/cm^2$), and ΔE is the potential range integrated [35].

$$Ni + 2OH^- \rightarrow \alpha - Ni(OH)_2 + 2e^- \tag{2.14}$$

Beden and co-workers calculated the charge densities corresponding to the low index face-centered cubic (FCC) planes of nickel: 516 $\mu C/cm^2$ (Ni (100)), 596 $\mu C/cm^2$ (Ni (111)), 364 $\mu C/cm^2$ (Ni (110)) taking $a = 3.523$ Å [34]. A coverage of two OH^- per nickel was assumed. Based on eq. 2.14, they concluded that 1 monolayer of the hydroxide forms at 0.25 ± 0.05 V in 0.1 M NaOH (50 mV s^{-1}) [34]. Machado and Avaca varied the upper limit of their potential sweep and compared the anodic and cathodic charges. Eventually the anodic charge exceeded the cathodic charge and they ascribed this to the onset of conversion of α-$Ni(OH)_2$ to β-$Ni(OH)_2$ around 0.5 V [98]. The use of 514 $\mu C/cm^2$ in the calculation of the electrochemical surface area of polycrystalline nickel electrodes assumes the 1 monolayer of $Ni(OH)_2$ formed is a mixture of the nickel low index planes. Weininger and Breiter noted that if the crystal planes are weighted according to their geometry and normalized with respect to the (100) plane, "the number of atoms per unit area are in the ratio $1/\sqrt{2}$ (110) : 1 (100) : $2/\sqrt{3}$ (111)" [99].

In theory, an estimation of the surface energy of these planes based on the broken bonds model in relation to stability reveals that Ni (111) (3 bonds broken) > Ni (100) (4 bonds) > Ni (110) (5 bonds). Clearly, Ni (111) should be the most abundant plane in any mixed grain estimation. On the other hand, Ni(111) is kinetically less stable over several cycles in 0.1 M NaOH than Ni(100) or (110) [34, 54].

One drawback of using this method is that the exact thickness of the α-$Ni(OH)_2$ layer formed has never been determined [95]. According to Beden and co-workers, two monolayers of the α-$Ni(OH)_2$ is initially formed on single crystal nickel (110) at

a sweep rate of 50 mV s^{-1} in 0.1 M NaOH. They argued that a limiting thickness of about 5 monolayers is achieved over the 0.6 V to 1.35 V potential range during the conversion of α- to β-$Ni(OH)_2$ [34] [100, 101]. Seyeux et al. studied the initial stages of nickel oxidation using scanning tunnelling microscopy (STM) and found that about 1.6 ± 0.1 monolayers (charge density of 1.6 ML = 590 ± 40 $\mu C/cm^2$) of β-$Ni(OH)_2$ (001) is formed around 0.45 V [100, 101].

The presence of NiO in this potential range as discussed earlier, may also render the method inaccurate [95]. Furthermore, electrode pretreatement and history may introduce inconsistency in the voltammetric behavior [95]. Although no consistent pretreatment method has been established in the literature, it is common practice to reduce the surface oxide by cathodic polarization at potentials less than -0.2 V [25, 30, 36, 58]. This ensures that the experiments can be started with a clean metallic nickel surface [23, 25, 30, 36, 58]. However, even small differences in electrode history and pretreatment may affect voltammetric measurements [95].

Integration of NiOOH anodic charge

Hall et al. suggested that the number of monolayers of the oxide / hydroxide film may be limited to just one monolayer at sweep rates $\geq$ 150 mV s^{-1} by the addition of oxalate salt to the alkaline electrolyte [95]. Initially, at scan rates $<$ 150 mV s^{-1}, they theorized that the composition of the oxide / hydroxide film was either oxalate-intercalated α-$Ni(OH)_2$ or a α/β-$Ni(OH)_2$ analogue of about 3 to 4 monolayers [95]. However at faster scan rates, $\geq$ 150 mV s^{-1} , one monolayer of $Ni(OH)_{2-x}(C_2O_4)_x$(ads) formed [95]. The addition of 0.08 M $C_2O_4^{2-}$ shifted the Ni^{2+} / Ni^{3+} (NiOOH) redox peak at 1.4 V by about -0.08 V and caused a decrease in peak width [95].

They argued that the charge in the NiOOH peak could be integrated accurately despite slightly overlapping with the onset of oxygen evolution [95]. They obtained a minimum NiOOH cathodic charge of 336 ± 17 $\mu C/cm^2$ at sweep rates $\geq$ 150 mV

s^{-1} [95]. The ECSA was determined by accepting a theoretical charge density of 195 μC cm^{-2} [95]. This value was calculated by assuming a coverage of 1 ML of $C_2O_4^{2-}$ on the hexagonal $Ni(OH)_2$ (001) face (1 e^- per Ni) [95].

2.4.2 Double layer capacitance

At certain potentials where the only electrochemical process occuring at the electrode/electrolyte interface is double layer charging, the characteristic capacitance may be determined [96]. For example, the double layer capacitance may be determined at -0.2 V, where the electrode is free of surface oxide [23, 25, 30, 36, 58]. Typical double layer capacitance values assumed for metallic electrodes are 20 μF cm^{-2} [49, 63, 92] or 25 μF cm^{-2} [48, 102] while 40 μF cm^{-2} [18, 103] has also been reported for oxide covered electrodes. Lasia et al. obtained 19 ± 4 μF cm^{-2} for nickel electrodes in 1 M KOH at negative potentials [48].

However, C_{dl} is potential dependent [18, 94, 95]. Lasia et al. showed that the double layer capacitance increases with increasing rate of hydrogen evolution (higher overpotentials) [49]. Therefore significant errors as high as $\pm 100\%$ may be introduced due to uncertainty in the determination of C_{dl} [94, 95]. Trasatti and Petrii warn that although a capacitance minimum is expected at the potential of zero charge ("double layer region"), its attainment may not entirely be due to the double layer [94]. Additionally, the nature and / or condition of the electrode as well as electrolyte effects may have unpredictable consequences for the accurate determination of C_{dl} [94].

2.5 Chapter summary

In this chapter, the nature of the oxide / hydroxide film formed at nickel has been discussed. Pure α- and β-$Ni(OH)_2$ phases existing in isolation at different potentials

Ref.	**Method**	**Potential / V**	**Electrolyte**	**Thickness / Å**	**Species identified**
[37]	XPS	0.8 (100 s)	0.5 M KOH	25	β-Ni(OH)$_2$ NiO
[40]	XPS	0.4 (300 s)	1 M NaOH	12 3	Ni(OH)$_2$ NiO
		0.7 (300 s)	1 M NaOH	14 14	Ni(OH)$_2$ NiO
[43]	Raman	0.25	0.1 M NaOH		Ni(OH)$_2$
		0.65	0.1 M NaOH		Ni(OH)$_2$ NiO
[17]	XRD		1 M KOH	9.0 5.4	Ni(OH)$_2$ NiO
[60]	Ellipsometry	0.49	0.1 M KOH	6.4	Ni(OH)$_2$
[41]	Ellipsometry	0.6-1.4	0.1 M NaOH		Ni(OH)$_2$ NiO
[80]	EQCM	1.2-1.4	1 M KOH		$\alpha\beta$-Ni(OH)$_2$

Table 2.1: Species present during electrooxidation of nickel at different anodic potentials. Note that $\alpha\beta$-Ni(OH)$_2$ is the interstratified pseudophase.

are not expected especially at slower sweep rates (5 mV s^{-1}) [95]. It is also evident that NiO is always present [36, 40, 41, 43, 61]. The oxide grows in the same potential range as β-Ni(OH)$_2$ [17, 37, 40, 41, 43, 62, 63]. The region from 0.6 to 1.2 V is characterized by a featureless plateau (small current) which renders the use of techniques which follow charge transfer inaccurate [35–37]. Typically, non-electrochemical techniques including XPS [37, 40], XRD [17, 80] and Raman [43, 55] have been used to study the evolution of the film. These studies showed that the gradual conversion of α-Ni(OH)$_2$ to β leads to the formation of interstratified phases bearing characteristics of both polymorphs [45, 70, 81, 84–88]. Hence, one must view the surface species in terms of relative coverage of α/β-Ni(OH)$_2$/NiO. Table 2.1 summarizes the literature evidence of the the species expected at different potentials during the electrooxidation of nickel that have been discussed in this chapter.

In the presence of the β phase, hydrogen evolution is catalyzed [23–26]. However β-Ni(OH)$_2$ also reduces in the process [15, 24].

Electrochemical impedance spectroscopy (EIS) has been used to study the kinetics of HER at nickel [48, 52]. Crucially, studies on the the kinetics of α- and β-$Ni(OH)_2$ interconversion remain scant.

Chapter 3

Dynamic electrochemical impedance spectroscopy

3.1 Introduction to EIS

Much like resistance, impedance is a measure of the ability of a circuit to resist the flow of current [104, 105]. However, the inherent assumption that Ohm's law is obeyed at all currents and voltages in the former fails to account for the contributions of reactance (inductive or capacitive). Unlike resistance, the reactance is frequency dependent. Impedance is a more inclusive term which encompasses the resistance (real part) and reactance (imaginary part).

In potential-controlled electrochemical impedance spectroscopy (EIS), a small sinusoidal potential summed with a DC component (constant or slow sweeping) is applied to the cell through the potentiostat. The current response acquired contains both AC and DC. The ratio of the AC phasors of potential and current gives the

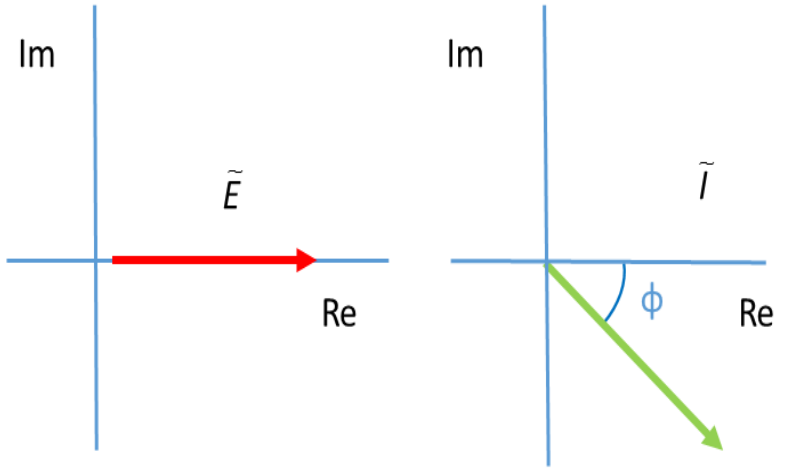

Figure 3.1: Relationship between the voltage and the current in EIS

impedance (eq. 3.1) [104]. The inverse of impedance is admittance (eq. 3.2) [104].

$$Z = \frac{\widetilde{E}}{\widetilde{I}} \tag{3.1}$$

$$Y = \frac{1}{Z} \tag{3.2}$$

Here the phasors $\widetilde{E}$ and $\widetilde{I}$ are complex numbers describing the magnitude and phase of the AC potential and AC current. In general, the current response is shifted in phase with respect to the potential (fig. 3.1). This may be extended by applying AC potentials of different frequencies. Since the different processes occuring at the electrode have different time constants, the kinetics of the system may be mapped out by plotting the impedance obtained over a series of frequencies, referred to as an impedance spectrum [104]. Additionally, the impedance spectra may be obtained over a potential range.

The term "impedance" is only applicable to linear systems. Conceptually, for a system to qualify as linear, the two rules of superposition must be obeyed [106];

1. Homogeneity: The output should scale in response to input signal. For example,

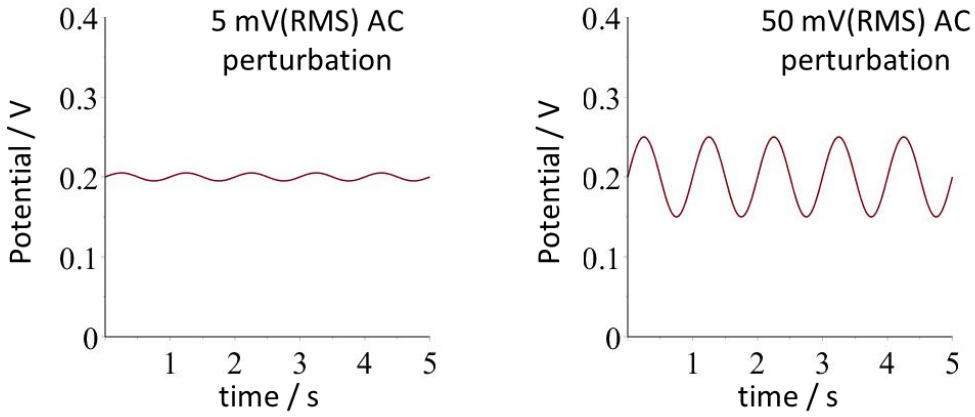

Figure 3.2: A large AC perturbation may change DC potential.

assuming $A_1(t)$ is an input (signal) and $B_1(t)$ is the output (response), if the response to $A_1(t)$ is $B_1(t)$, then $2A_1(t)$ should generate $2B_1(t)$ in response.

2. Additivity: If signals A_1 and A_2 are applied separately and generate responses individually. When A_1 plus A_2 is applied, the system response should equal the sum of the individual responses when A_1 and A_2 were applied separately.

However, despite the inherent non-linearity of electrochemical systems, using a small potential signal ensures that only a small linear portion of the response is seen during data acquisition (pseudolinearity). Additionally, keeping the AC perturbation small ensures the DC potential is not significantly changed (fig. 3.2).

It is equally important that the electrochemical system remain stable throughout the time required for acquisition of the EIS spectrum [104, 105].

One of the biggest advantages of EIS is its efficiency in the acquisition of data [104, 107]. In theory, all the characteristics of a linear electrochemical system could be obtained if the impedance were measured over an infinite frequency range [107]. EIS is typically used for the determination of the kinetic parameters of an electrochemical system and the refinement of mechanisms [104, 107]. It has also been used

for the determination of electrochemically active surface area (ECSA) [48]. Despite its advantages, EIS gives no specific chemical information and therefore should only be introduced for simple systems or circuits whose physical and electrochemical characteristics are well understood [104].

3.1.1 Potentiostatic EIS vs dEIS

In this section, it is particularly important to make the distinction between potentiostatic EIS (single frequency or multisine) and dEIS. EIS spectra may be acquired by applying sinusoidal potentials one frequency at a time in the manner already described. However, this method is slow. The speed of acquisition of data is particularly problematic when probing systems which undergo slow irreversible changes with time. Multisine potentiostatic EIS is a Fourier transform technique which shortens the spectra acquisition time by combining the sine waves and applying them all at once. As with single-frequency potentiostatic EIS, the AC perturbations are added to a constant DC potential.

In dEIS, the multisine AC perturbation is summed onto a slow sweeping or hold (fig. 3.3). Hence, impedance is collected continuously under non-stationary conditions [29]. Therefore, the processes occurring at the electrode may be studied from initial stages to completion [28, 29]. Since EIS spectra and DC voltammograms are obtained simultaneously, the behavior of the system may be followed as a function of potential [28, 108]. The additional information, e.g., charge, accessible from the CV helps with the rationalization and justification of mechanistic models.

3.2 dEIS theory

The dEIS technique is now discussed in more detail including the conditions required to make reliable, valid impedance measurements.

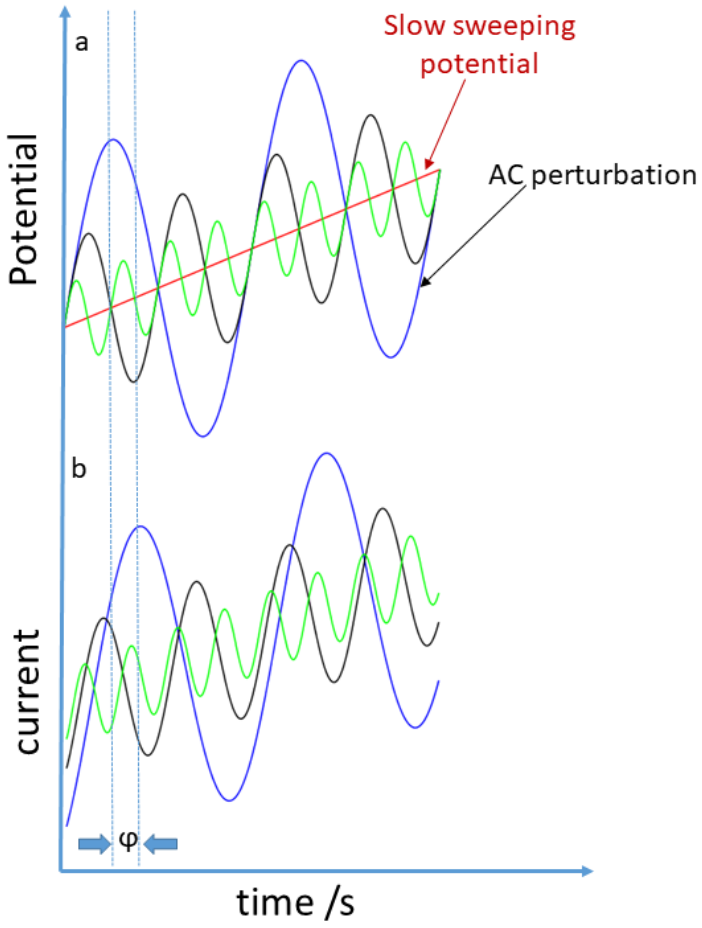

Figure 3.3: Principle of dEIS. (a) AC and DC applied to the cell, (b) current response.

3.2.1 Multisine

During the potential scan / hold, the waveform is continuously applied for a period, $T = 1/f_{\min}$. All frequencies applied are integer muliples of the minimum frequency ($f_{\min}$) in order to fit into the period (eq. 3.3) [29, 109, 110].

$$f_{n_i} = n_i f_{\min} \tag{3.3}$$

where the integer n_i is the multiple of the base frequency. The amplitudes of the sine waves are summed according to a "2:10" scheme [109, 110]. This scheme scales down the amplitude of the higher frequency sine waves, after the specified minimum frequency, logarithmically by a factor of two per decade [109, 110].

The signal applied contains a DC component which is generated separately and is summed with the multisine waveform prior to application. This is expressed as

$$E = E_{\mathrm{dc}} + \sum_{i=1}^{N\mathrm{freqs}} \sqrt{2} a_i \sin(2\pi f_{n_i} t + \psi_i). \tag{3.4}$$

where $a_i = a_{\min}.f_{n_i}^{-\log_{10}(2)}$ is the scaled root mean square (RMS) amplitude used for the higher frequency sine waves per the 2:10 rule stated earlier and E_{dc} is the DC potential (it changes during the sweep). Also, ψ_i is the phase for each frequency [29].

Similarly the current response contains AC and DC components which can be expressed as

$$I = I_{\mathrm{dc}} + \sum_{i=1}^{N\mathrm{freqs}} \sqrt{2} I_i \sin(2\pi f_{n_i} t + \varphi_i) \tag{3.5}$$

where φ_i is the phase, I_{dc} is the DC component of the current response and I_i is the amplitude of the AC component of the current response frequency (f_{n_i}) [29].

The AC components of the current response are obtained by fast Fourier transformation at each potential. Subsequently, the impedance is obtained over the de-

sired potential range by repeating the measurement as the DC potential is changed [29, 108, 109].

3.2.2 Criteria for obtaining valid results

1. In general, the amplitude of the AC pertubation must be kept small [28, 29, 110]. This should be less than about 5 mV(RMS) per frequency (about 30 mV peak to peak for the overall waveform) [29]. This condition helps preserve the pseudolinearity of the current response [28, 29, 111, 112].

2. The lowest frequency of the AC pertubation must be chosen such that DC component does not change much during the AC cycle. The condition is obtained from unit analysis of

$$2\pi f_{\min} \gg \frac{Fv}{RT} \tag{3.6}$$

where f is the lowest frequency, v is the sweep rate, F is Faraday's constant, R is the gas constant and T is the temperature [28, 29, 109]. This condition ensures that the DC potential stays approximately the same over one cycle of the lowest frequency. The violation of this rule may result in the appearance of noise in the low frequency region of the Fourier transformed data [111].

Criteria requiring small changes in DC current and coverage may also be imposed [29, 109, 111]. However, these conditions are difficult to establish since they are not known prior to experimentation [109]. Hence, they are not considered in this work but they have been discussed in detail by Sacci et al. [109].

3.2.3 Baseline correction types

The AC + DC potential is applied to the cell and both the potential applied and the current response are measured. In the case of the potential, the AC and DC components are easily separable because the initial DC potential is known. The DC potential is subtracted from the AC + DC potential using electronic amplifiers. However, for the current, such subtraction is not as straightforward because the DC current is not known. Small sections of the DC component of the signal may have a nearly constant slope. The fast Fourier transform (FFT) treats these sections as periodic (i.e a sawtooth waveform), which introduces substantial errors at the base frequency and its harmonics due to contributions from the sawtooth waveform [29, 109]. Sacci and Harrington described this as the "baseline effect" and established a software approach for correcting prior to transformation [29, 109]. Two corrections were proposed.

With internal correction, the baseline of this "constant slope section" is established as a line between the first and last points of the data to be transformed, and is subtracted off. This means that the first and last points will become zero. The DC is adjusted to compensate for this. Expectedly, the method is often subject to noise glitches since it is determined from only two points.

With extrapolation correction, the baseline is established using the value predicted by linear extrapolation of the last two successfully transformed sections in the time series. Hence, the slope of the baseline is continuously modified based on those two preceeding values. Therefore, noise glitches are unlikely to lead to inaccurate determination of the AC component [109]. However, this method is less responsive to sudden changes in the DC component.

3.2.4 Kramers Kronig compliance

The Kramers Kronig (KK) test is one of the techniques for validating impedance data. The use of the KK transforms is based on the following assumptions [104, 105, 107, 113];

1. The system response must be linear.

2. The system must relax to its initial state on removal of the AC perturbation (stable)

3. The system must not produce a response before the perturbation is applied at t_0 (Causal).

4. The response must be finite for all values of the frequency.

When these conditions are satisfied, then the imaginary part of admittance at any frequency can be calculated from the real part and vice versa, using the KK transforms [104]

$$\mathrm{Im}(Y(\omega)) = \frac{2\omega}{\pi}\int_0^\infty \frac{\mathrm{Re}(Y(x)) - \mathrm{Re}(Y(\omega))}{x^2-\omega^2}\mathrm{d}x, \tag{3.7}$$

$$\mathrm{Re}(Y(\omega)) = \mathrm{Re}(Y(0)) - \frac{2\omega}{\pi}\int_0^\infty \frac{(\omega/x)\,\mathrm{Im}(Y(x)) - \mathrm{Im}(Y(\omega))}{x^2-\omega^2}\mathrm{d}x, \tag{3.8}$$

$$\mathrm{Re}(Y(\omega)) = \mathrm{Re}(Y(\infty)) - \frac{2\omega}{\pi}\int_0^\infty \frac{x\,\mathrm{Im}(Y(x)) - \omega\,\mathrm{Im}(Y(\omega))}{x^2-\omega^2}\mathrm{d}x. \tag{3.9}$$

Note that $\mathrm{Im}(Y)$ and $\mathrm{Re}(Y)$ are the imaginary and real parts of the admittance. The KK transforms have been written in terms of admittance because admittance is the transfer function (output/input = current/potential) for potentiostatic measurements.

However, the KK transforms require the extrapolation of the impedance data from zero frequency to infinite frequency, which can be complicated. In practice, if the data

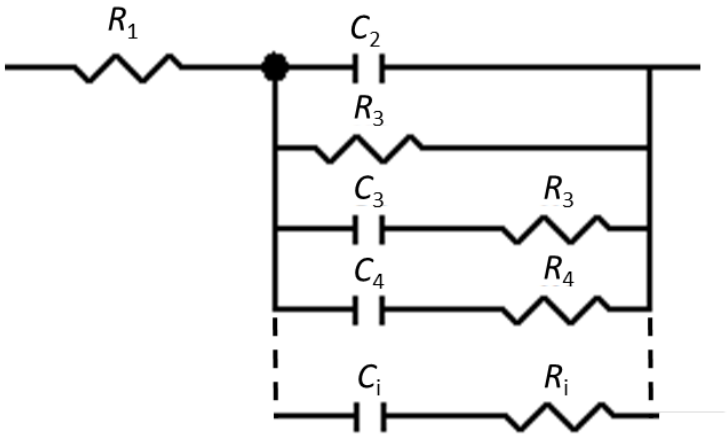

Figure 3.4: Maxwell circuit used for testing KK compliance of admittance data. Note that the circuit has many additional C_iR_i branches to enable 7 time constants per decade of frequency.

can be fitted to a stable RLC circuit, then it must be KK transformable, hence the use of the equations above can be avoided [104]. When an equivalent circuit cannot be found, the Maxwell circuit can be used to model the admittance (fig. 3.4) [104, 113].

For KK-compliant data, a random distribution of the residuals about the frequency axis is observed (fig. 3.5). Whereas, a clear trend around the frequency axis indicates the data is corrupted [113]. This may be because the system drifted during the time scale of data acquisition or perhaps too large a perturbation was applied [113].

3.3 Data presentation in EIS

The two most common graphs for visualizing impedance data are Nyquist and Bode plots. The interpretation of these plots and extraction of the values of the circuit elements are discussed here using the example of a dummy cell (fig. 3.6).

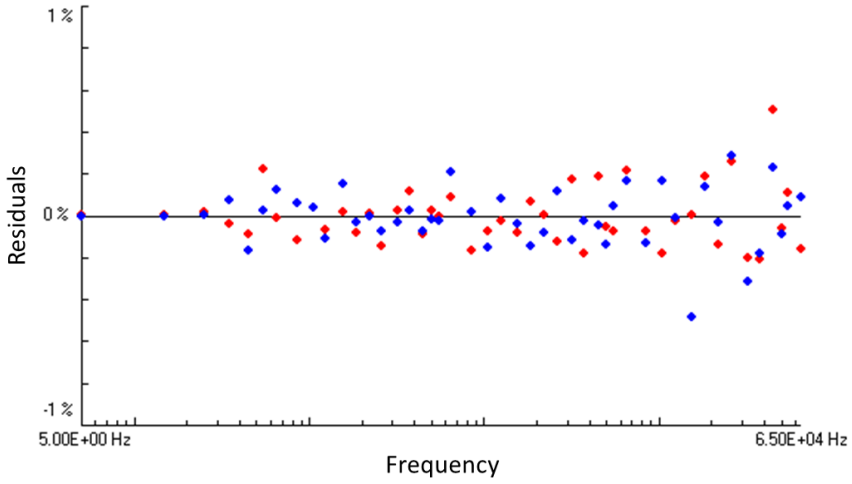

Figure 3.5: KK test demonstrating the compliance of the dummy cell. Note that the red and blue dots are the residuals of the real and imaginary parts of the admittance respectively, when fitted to the Maxwell circuit

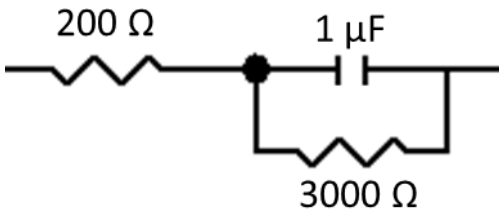

Figure 3.6: Sample equivalent circuit (dummy cell).

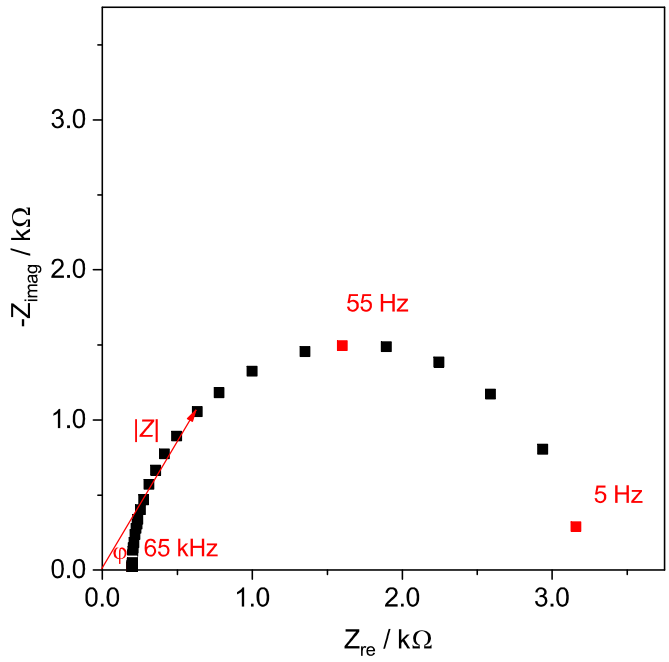

Figure 3.7: Nyquist plot for impedance obtained for the circuit in fig. 3.6

3.3.1 Nyquist plot

This is a plot of the imaginary ($-Z_{\text{imag}}$) versus the real part (Z_{Re}) of the impedance (fig. 3.7). Key points to note are:

1. Each point corresponds to the impedance at a particular frequency.

2. At high frequency, the reactance of the capacitor becomes very small and it acts like a short circuit (no voltage drop across the 3000 Ω resistor). Hence, the solution resistance is measured at high frequency (65 kHz in this case). The solution resistance is the resistance between the solution side of the electrode/electrolyte interface at the working electrode and the tip of the reference electrode [104].

3. Conversely, at low frequencies, the reactance of the capacitor becomes large and it behaves like an open circuit. The polarization resistance (200 Ω + 3000 Ω) is obtained by fitting the low frequency intercept. Note that the charge transfer

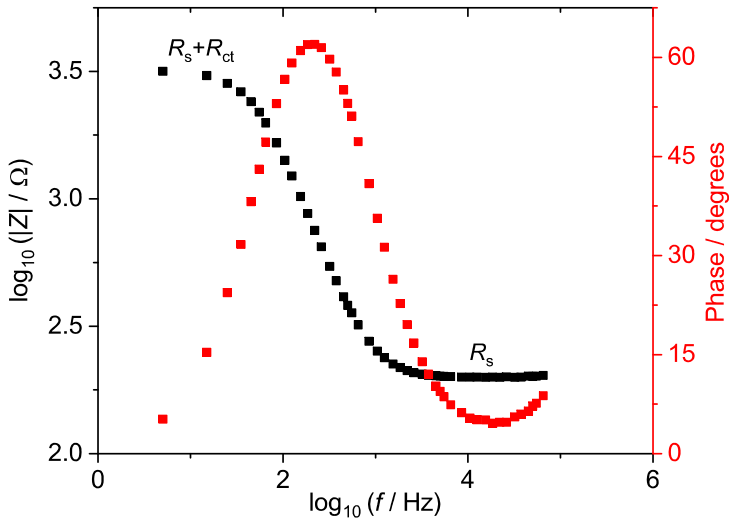

Figure 3.8: Bode plot showing the dependence of the magnitude of impedance (black) and phase (red) on log frequency for the circuit shown in fig. 3.6.

resistance (R_{ct}) is the difference between the low and high frequency intercepts.

4. The capacitance (C) may be determined from

$$C = \frac{1}{2\pi f_{top} R_{\mathrm{ct}}} \tag{3.10}$$

for a semicircle with diameter R_{ct}, where f_{top} is the frequency at the maximum reactance.

3.3.2 Bode plot

Bode plots are usually used to visualize the frequency dependence of the magnitude of impedance ($|Z|$) and the phase (φ).

Key points to note are:

1. The phase angle and $|Z|$ are determined at each frequency using

$$\varphi = \tan^{-1}\left(\frac{-Z_{\text{imag}}}{Z_{\text{Re}}}\right) \tag{3.11}$$

$$|Z| = \sqrt{Z_{\text{Re}}^2 + Z_{\text{imag}}^2} \tag{3.12}$$

2. At sufficiently high or low frequencies, resistance dominates (flat parts of the black curve). However, the straight line observed in the middle whose slope is roughly -1 is indicative of the presence of a capacitor.

3. The time constant, $\tau = R_{\text{ct}}C_{\text{dl}}$, may be determined for each process occurring in the electrochemical system. Here, R_{ct} is the charge transfer resistance and C_{dl} is the double layer capacitance.

3.4 Analysis of EIS spectra using equivalent circuits

Electrical analogs are often used to explain electrochemical data [28,104,105,107]. It has become the predominant method of analyzing impedance data in recent years partially because of the development of computer algorithms capable of fitting almost any impedance spectra, provided they are restricted to the right side of the complex plane [107, 108]. Each process occurring in an electrochemical system may be represented with a different circuit element. For example, resistors are used to represent the uncompensated resistance between the reference and the working electrode (solution resistance) or charge transfer at the electrode/electrolyte interface. Capacitors are used to represent the double layer at the electrode/electrolyte interface or adsorption of species on the electrode surface. The models used in the analysis of EIS spectra typically combine many circuit elements, which are arranged in a manner that is ideally analogous to the physico-chemical processes occuring in the system.

However equivalent circuits are not unique, since more than one model may fit the same data set. Equivalent circuits must therefore be used cautiously. Indeed certain systems may not be describable using equivalent circuits. Additionally, some system characteristics may have no simple electrical anologs, e.g., Warburg impedance [104,107], and others, e.g., constant phase element, can be difficult to justify physically [105, 107].

3.4.1 Complex nonlinear least-squares fitting

The complex nonlinear least squares (CNLS) method is predominantly used for fitting impedances [104, 105]. Essentially, the experimental impedance values are compared to those calculated for an equivalent circuit using eq. 3.13.

$$S = \sum_{i=1}^{N} w_{i,\mathrm{Re}}[\mathrm{Re}(Z_{i,\mathrm{exp}}) - \mathrm{Re}(Z_{i,\mathrm{calc}})]^2 + w_{i,\mathrm{Im}}[\mathrm{Im}(Z_{i,\mathrm{exp}}) - \mathrm{Im}(Z_{i,\mathrm{calc}})]^2 \qquad (3.13)$$

Here, S is the weighted sum of squares, $\mathrm{Re}(Z_{i,\mathrm{exp}})$ and $\mathrm{Im}(Z_{i,\mathrm{exp}})$ are the real and imaginary parts of the experimentally obtained impedance, $\mathrm{Re}(Z_{i,\mathrm{calc}})$ and $\mathrm{Im}(Z_{i,\mathrm{calc}})$ are the real and imaginary impedances calculated for the equivalent circuit, $w_{i,\mathrm{Re}}$ and $w_{i,\mathrm{Im}}$ are the statistical weights of the data and N is the number of frequencies sampled [104]. The objective of CNLS fitting is to determine the parameter values which minimize S [104, 105, 114]. The optimization was done using the nonlinear simplex algorithm as implemented in a Maple program immfit [114].

The fitting is usually carried out using iterative algorithms which require that initial guesses be provided for each of the circuit parameters. Ideally, these initial guesses should be relatively close to the experimental values in order to avoid a local minimum which can give large parameter errors [104]. Despite obtaining a good fit, Bandarenka cautions that physico-chemical justification may be required in order to

interpret the values [108].

3.4.2 Weighting schemes

Weighting is a correction technique applied in CNLS fitting of impedance spectra. These corrections are necessary in order to compensate for random instrument errors during data acquisition and non-systematic errors due to frequency range [105]. They help to improve the estimation of the values of the circuit elements and their uncertainty [115]. Two examples are discussed below.

Proportional weighting

This method assumes that the weight of the real (or imaginary) part is inversely proportional to the square of the real (or imaginary) part of the experimental point. It is particularly useful when the components of the complex impedance vary significantly in magnitude [104,114]. The weights may be based on experimental data (proportional experimental) or calculated data (proportional theory) as follows [104,114]:

$$w_{i,\mathrm{Re}} = \frac{1}{\mathrm{Re}(Z_{i,\mathrm{exp}})^2}, w_{i,\mathrm{Im}} = \frac{1}{\mathrm{Im}(Z_{i,\mathrm{exp}})^2} \qquad \text{Proportional experimental} \tag{3.14}$$

$$w_{i,\mathrm{Re}} = \frac{1}{\mathrm{Re}(Z_{i,\mathrm{calc}})^2}, w_{i,\mathrm{Im}} = \frac{1}{\mathrm{Im}(Z_{i,\mathrm{calc}})^2} \qquad \text{Proportional theory} \tag{3.15}$$

Magnitude / modulus weighting

Magnitude weighting assumes that random errors in the real and imaginary parts are similar. Hence the same weight is used for the real and imaginary parts [104]. Like proportional weighting, magnitude weighting is carried out in two ways. For magnitude experimental weighting, the weighting of the real and imaginary parts are

inversely proportional to the square magnitude of the experimental point (eq. 3.16). Magnitude theory uses the values obtained from the fitted model instead [114].

$$w_{i,\mathrm{Re}} = w_{i,\mathrm{Im}} = \frac{1}{\mathrm{Re}(Z_{i,\mathrm{exp}})^2 + \mathrm{Im}(Z_{i,\mathrm{exp}})^2} \qquad \text{Magnitude experimental} \tag{3.16}$$

$$w_{i,\mathrm{Re}} = w_{i,\mathrm{Im}} = \frac{1}{\mathrm{Re}(Z_{i,\mathrm{calc}})^2 + \mathrm{Im}(Z_{i,\mathrm{calc}})^2} \qquad \text{Magnitude theory} \tag{3.17}$$

3.4.3 Chi-square

The chi-square statistic is used to verify the quality of fit. It compares the experimental and calculated impedances [116]. It is defined as

$$\chi^2 = \sum_{i=1}^{N} \{ \frac{[\mathrm{Re}(Z_{i,\mathrm{exp}}) - \mathrm{Re}(Z_{i,\mathrm{calc}})]^2}{\sigma^2_{\mathrm{Re},i}} + \frac{[\mathrm{Im}(Z_{i,\mathrm{exp}}) - \mathrm{Im}(Z_{i,\mathrm{calc}})]^2}{\sigma^2_{\mathrm{Im},i}} \}. \tag{3.18}$$

Here $\sigma^2_{\mathrm{Re},i}$ and $\sigma^2_{\mathrm{Im},i}$ are the squares of the variances of the real and imaginary parts [104, 116].

Usually, the weighted sum of squares, S, is assumed to be proportional to χ^2 and is often quoted instead.

3.4.4 Statistical analysis for adding circuit elements

The model that best fits the data should have the smallest χ^2 value. However, models with more parameters typically give smaller χ^2 values despite the possible introduction of extraneous parameters (overfitting). Hence, further statistical analysis is necessary in order to justify the addition of circuit elements to the model. The Fisher-Snedecor test (F-Test) and the Akaike information criterion (AIC) are discussed below.

F-Test

The F-test helps decide if the addition of a new parameter to an equivalent circuit / model results in a statistically significant improvement in χ^2. The formula

$$F_{\text{exp}} = \frac{\frac{\chi^2(\text{old})-\chi^2(\text{new})}{k}}{\frac{\chi^2(\text{new})}{2N-m-k}} \tag{3.19}$$

compares the chi-square values for two models. Here, N is the number of frequencies fitted, χ^2(old) is the chi-squared for a circuit with m parameters, χ^2(new) is the chi-squared for the circuit with k additional parameters. The quantity $2N - m - k$ is the number of degrees of freedom for the new fit with $m + k$ parameters. Note that the number of parameters may not necessarily be the same as the number of circuit elements. For example, a circuit containing two resistors and one capacitor, R(CR), has 3 parameters. However, changing the capacitor to a constant phase element (CPE, non-ideal capacitor), R(QR), increases the number of parameters to 4 since the CPE has two parameters [104].

The F_{exp} calculated is compared to the theoretical values for F corresponding to a particular confidence level (typically 95% or 99%) and the number of degrees of freedom [105]. This may be done using the cumulative distribution function (CDF) in Maple. A small value (e.g. $< 1\%$) for the probability, $1 - \text{CDF}$, indicates that the decrease in χ^2 on addition of the new parameter is not by chance [104]. Hence, the new model should be accepted [104].

AIC

Ingdal et al. recently published a paper [117] demonstrating the merits of AIC for CNLS fitting of impedance or admittance data. Its advantage over the F-test is in its allowance for the comparison of non-nested models [117, 118]. Note that two models are nested if one model contains all the parameters of the other plus one

additional parameter. Cuici described the AIC as the tradeoff between the goodness of fit, which improves as the number of parameters in the model increases, and the complexity of the model [119].

$$AIC = -2\ln(L) + 2(M+1) \tag{3.20}$$

$$AICc = -2\ln(L) + 2(M+1)\left(\frac{2N}{2N-M-2}\right) \tag{3.21}$$

Here L is a likelihood estimator which is maximized when the residual sum of squares is minimized, M is the number of parameters in the model and N is the number of frequencies [114, 117, 118]. A more negative AIC is obtained for simple models for which the residual sum of squares is least [117]. The AICc corrects for small samples where number of frequencies / number of parameters ≤ 40 [117, 118].

The inherent advantage is that AIC (or AICc) values may be obtained for individual models and/or weighting schemes and comparisons can easily be made [117, 118].

Chapter 4

Validation of dEIS instrumentation using model circuits

4.1 Introduction

Earlier, it was established that dEIS has the potential to measure systems changing with time during a potential sweep or sweep-hold. Ultimately, the aim of this work is to determine the time constants (τ) for the different processes which occur during interconversion of surface hydroxides at nickel. However, capturing the time constant is dependent on both how fast the processes occurring at the surface are and the instrument response. The latter can be easily validated on model circuits.

Sacci and Harrington demonstrated using sweep experiments between -0.4 V and 0.4 V performed on dummy cells that dEIS gives results which are comparable to conventional EIS down to a frequency of 1 Hz [29]. In this chapter, the current decay and changes in the EIS spectra are monitored during potential holds done on model circuits. The aim was to determine the fastest decay which can be measured during the potential hold using dEIS.

While a single time constant (for a one step decay) may be obtained from fitting

the current decay, repeated acquisition of impedance spectra using dEIS during a potential hold allows subtle changes in the surface processes to be gleaned. In essence, a time constant may be determined at any point during the potential hold. Additionally, the features which are observable in the impedance spectra make it easier to identify the different processes which may be occurring during the hold.

4.2 Experimental conditions

The current decay as well as the impedance for these circuits were collected in order to validate the fastest time constants which may be measured during a potential hold using the dEIS instrumentation (already described in [29,109]). In the experiments shown here, the potential was swept from 0 V to ca. 0.25 V at 5 mV s^{-1} and subsequently held at ca. 0.25 V. The frequency range used was 1 Hz to 13 kHz.

4.3 Model circuits

The model circuits shown in fig. 4.1 were constructed from standard resistors and capacitors. The models have different time constants which are determined theoretically from

$$\tau = R_{||}C \tag{4.1}$$

where τ is the time constant, $R_{||}$ is the parallel combination of resistor R_1 and R_2 while C is the capacitance of the capacitor. The time constants of these circuits will be determined from the current decay and the impedance measured using dEIS. The correct measurement of the theoretical time constant shows that the instrument responds fast enough to capture processes which may occur on that time scale.

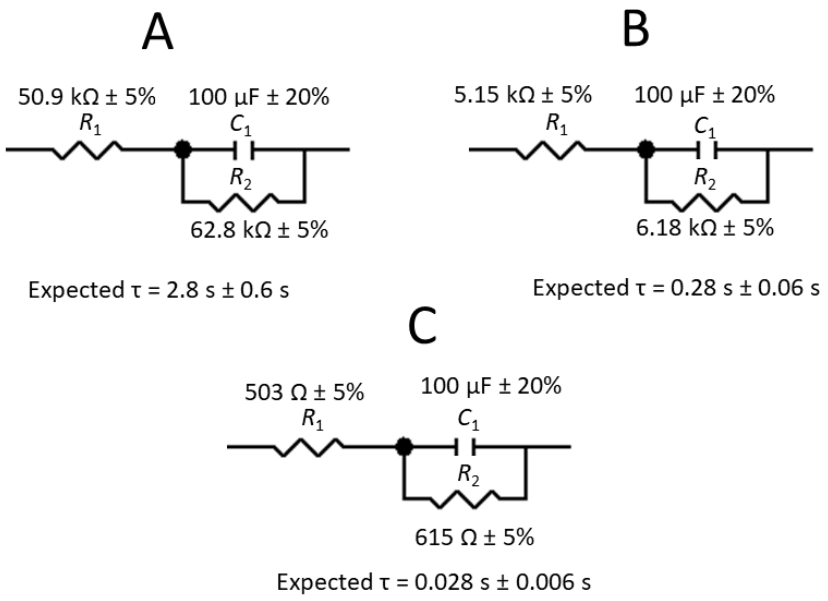

Figure 4.1: Model circuits for validation of time constants obtainable using dEIS set-up. (a) 0.028 s, (b) 0.28 s, (c) 2.8 s.

4.4 Current decay

The charging current on the capacitor may be calculated from

$$I_c = C\frac{\mathrm{d}E}{\mathrm{d}t}. \tag{4.2}$$

Where I_c is the capacitor charging current, C is the capacitance of the capacitor, $\frac{\mathrm{d}E}{\mathrm{d}t}$ is the sweep rate. During the sweep from 0 V to 0.25 V, the current increases as charges build up on the plates of the capacitor (fig. 4.2a). When the potential is held at 0.25 V, I_c tends to zero. However, the current does not reduce instantaneously. Instead it decreases exponentially (fig. 4.2b) from a value I_0 at the beginning of the hold to I_∞ at time $t = \infty$, as shown in the next section. The characteristic time constant for this exponential decay is a measure of how fast the system response (the current in this case) decays to zero.

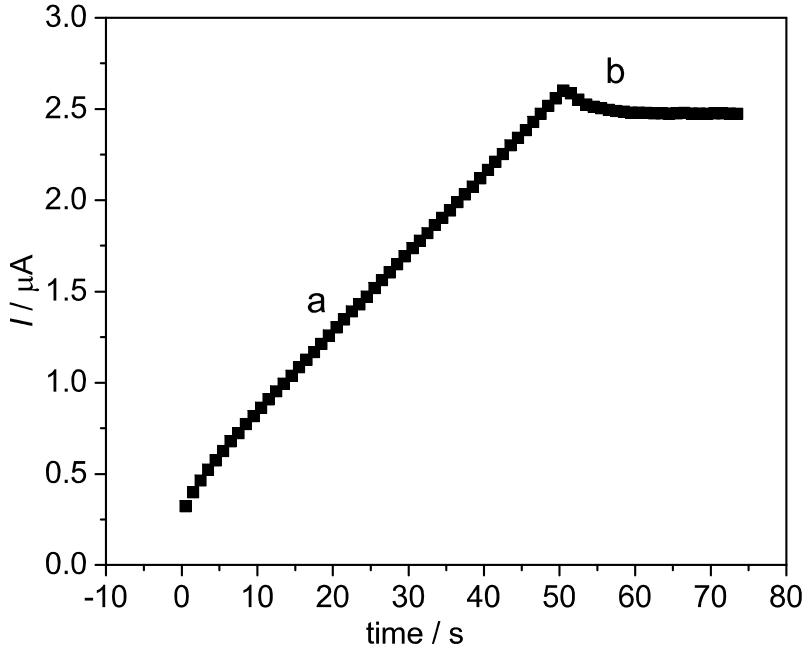

Figure 4.2: Current vs time obtained for model A during sweep-hold. (a) Increasing current during sweep between 0 V and 0.25 V at 5 mV s^{-1}. (b) Current decay during the potential hold.

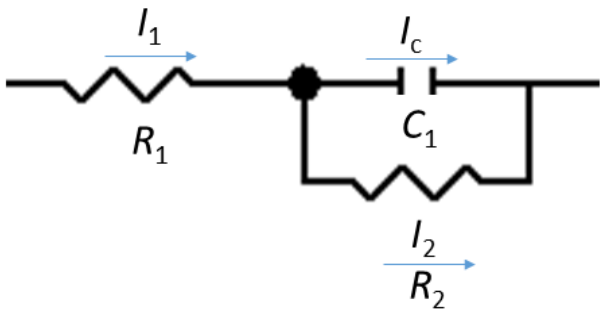

Figure 4.3: Currents through the resistors and the capacitor in the model circuit.

The time constant determined from fitting the transient current (current decay) should be the same as the theoretical value for each circuit provided the instrument response is fast enough.

4.4.1 Theory

This section describes the procedure to derive the expected current response to the sweep-hold potential. The fundamental equations are:

$$V(t) = E_1(t) + E_2(t) \text{ KVL} \tag{4.3}$$

$$I_1(t) = I_2(t) + I_c(t) \text{ KCL} \tag{4.4}$$

$$E_1(t) = I_1(t)R_1 \tag{4.5}$$

$$E_2(t) = I_2(t)R_2 \tag{4.6}$$

$$I_c(t) = C\frac{\mathrm{d}E_2(t)}{\mathrm{d}t} \tag{4.7}$$

The relationship between the currents and potentials across the circuit components can be derived from Kirchoff's voltage (KVL) and current laws (KCL) (fig. 4.3). Here

$I_1(t)$ and $I_2(t)$ are the currents while $E_1(t)$ and $E_2(t)$ are the potential differences across resistors R_1 and R_2 respectively. Note that $I_c(t)$ is the charging current for capacitor C_1. The applied potential $V(t)$ consists of the sweep from 0 V to V_0 at sweep rate v, followed by the hold at potential V_0. The initial condition is that $E_2(t)$ is zero, consistent with all the voltages and currents being zero at the beginning of the sweep. The values for R_1, R_2 and the capacitor C_1 are known (fig. 4.1). The system of differential and algebraic equations was solved in Maple. The hold part of the current response is given by:

$$I(t) = I_a(t) \exp\left(\frac{-t}{\tau}\right) + I_\infty \tag{4.8}$$

$$\tau = \frac{C R_1 R_2}{R_1 + R_2} \tag{4.9}$$

$$I_\infty = \frac{V_0}{R_1 + R_2} \tag{4.10}$$

where the time at the beginning of the hold has been defined as zero, and $I_a(t)$ is a complicated function of C, R_1, R_2, V_0 and v.

4.5 EIS Simulation

Ideally, the EIS spectra for all these model circuits should give a semicircle (like fig. 3.7 and fig. 4.4f). However, the frequency range determines how much of that semicircle will be seen in the EIS spectrum (fig. 4.4) and consequently, the values of the circuit parameters which may be obtained from the fit.

When the impedance was simulated using a frequency range of 1 Hz to 13 kHz, only a small portion of the semicircle was seen for models A and B (fig. 4.4a and c). However, when the impedance for the models was simulated with a frequency range of 0.1 Hz to 13 kHz , more of the semicircles were seen (fig. 4.4b and d).

Fig. 4.5 shows the simulated Bode phase plots expected when a frequency range of

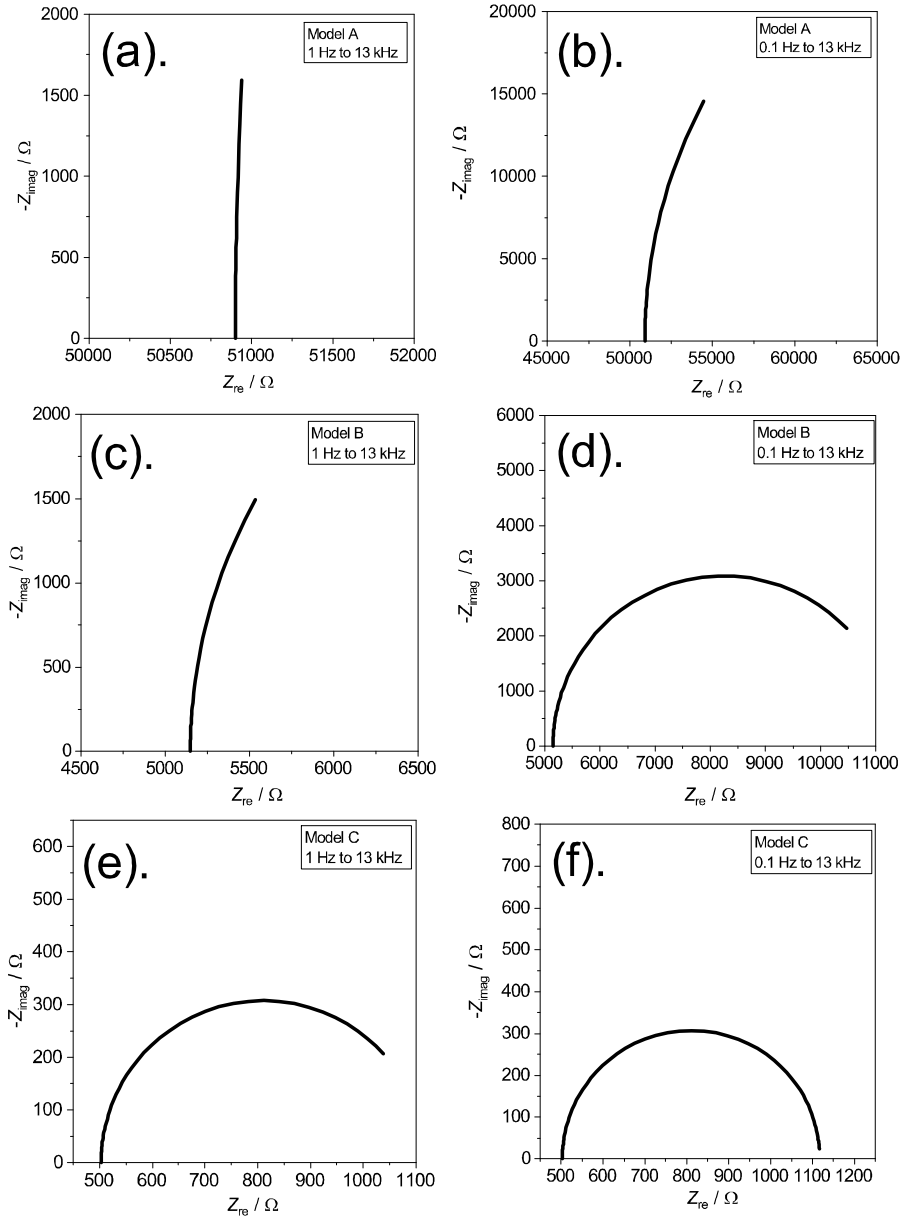

Figure 4.4: Simulated Nyquist plots for Models in fig. 4.1 showing expected features at different frequency ranges. (a) 1 Hz to 13 kHz for model A, (b) 0.1 Hz to 13 kHz for Model A, (c) 1 Hz to 13 kHz for model B, (d) 0.1 Hz to 13 kHz for Model B, (e) 1 Hz to 13 kHz for model C, (f) 0.1 Hz to 13 kHz for Model C.

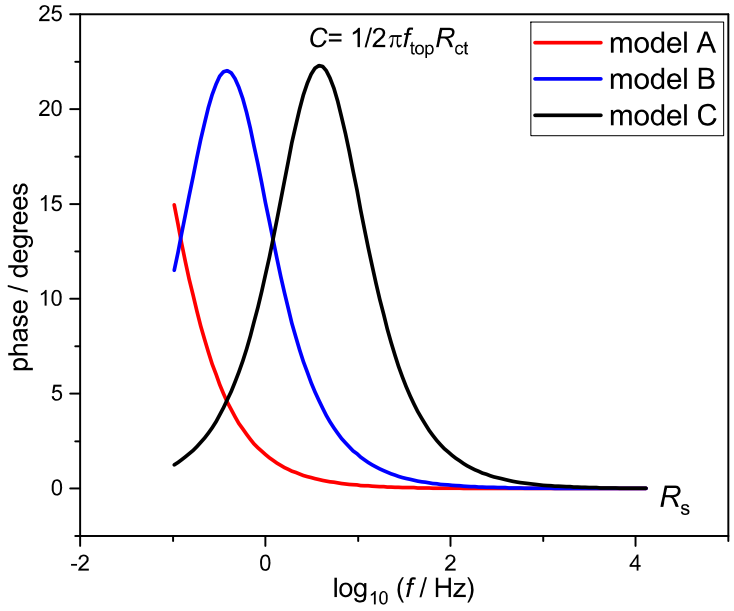

Figure 4.5: Simulated Bode phase plot in the 0.1 Hz to 13 kHz frequency range for the models in fig. 4.1.

0.1 Hz to 13 kHz was used. The plot also shows the features which may be required in order for the circuit elements in the model to be determined. Evidently, at frequencies less than 1 Hz ($\log f = 0$), less of these features appear for models A and B. Hence fitting the impedance obtained to the model circuits (fig. 4.1) may give a bad fit since not all the features expected for model are observed. Note that for model C, using the 1 Hz to 13 kHz range, all the features are expected to be determinable.

Although these simulations showed that the 0.1 Hz to 13 kHz is perhaps more suitable for measuring the EIS of the model circuits in fig. 4.1, excursions to frequencies lower than 1 Hz are not relevant to this work (interconversion of nickel hydroxides). Additionally, Sacci and Harrington already showed that impedance spectra acquired using dEIS are only equivalent to those obtainable from conventional EIS down to 1 Hz at 5 to 50 mV s^{-1} in sweep experiments done on dummy cells [29]. Hence, the results discussed next concern only decays and impedances measured during a potential hold in the 1 Hz to 13 kHz frequency range.

4.6 Results and discussion

Table 4.1 is a summary of the results which will be discussed in this section. The values for I_∞ and $I_a(t)$ were determined from the current decay by fitting to the exponential decay function in eq. 4.8. The values of R_1, R_2 and C_1 labelled "decay" were then determined by solving the equations relating them to τ, I_a and I_∞ given in section 4.4.1.

The values of R_1, R_2 and C_1 labelled "dEIS" were obtained from the impedance spectra by fitting to equivalent circuits in Maple (sections 4.6.1, 4.6.2 and 4.6.3). Since the values expected for these circuit elements are known (fig. 4.1) , the values obtained from fitting the impedance provide further validation of the data obtained. Where R_1, R_2 and C_1 were obtained from the fit, the time constant was then determined from eq. 4.1.

4.6.1 Model A

For model A, whose theoretical time constant is 2.8 seconds, the time constant (2.81±0.07 s) was determined correctly from the transient current (fig. 4.6a). This shows that the instrument responds fast enough to capture the time constant. Additionally, C_1 was correctly calculated using the derived values for I_∞ and $I_a(t)$. The value of $R_1 + R_2$ was determined correctly using eq. 4.10. However, individually the values of R_1 and R_2 could only be determined approximately (within 30%).

Since very little of the semicircle is seen in this frequency range, only R_1 (50245±200 Ω) could be extracted correctly from the impedance spectra throughout the sweep-hold (fig. 4.6b, table 4.1). The KK test was used to probe the validity of the impedance data obtained (fig. 4.6c). The random dispersion of the residuals about the frequency axis, shows that the data fulfills the criteria established earlier and is valid (fig. 4.6c). The average percentage error of 9% for the residuals is large but is not

		model A	**model B**	**model C**
potential / V		**0.257**	**0.257**	**0.254**
I_∞ / μA	**theoretical**	2.26	22.6	227
	decay	2.47	22.5	223
$I_a(t)$ / μA	**theoretical**	0.15	0.20	0
	decay	0.108	0.003	0.119
τ / s	**theoretical**	2.8±0.6	0.28±0.06	0.028±0.06
	decay	2.81±0.07	0.94±0.18	15.6±1.7
	dEIS			0.027±0.008*
R_1 / Ω	**theoretical**	50900±2545	5150±257	503±25
	decay	57600		
	dEIS	50245±200	5110±7	499.9±0.2
C_1 / μF	**theoretical**	100±20	100±20	100±20
	decay	110		
	dEIS		101±3	94.5±0.3
R_2 / Ω	**theoretical**	62800±3140	6180±309	615±31
	decay	46000		
	dEIS			604.0±2.1
R_1+R_2 / Ω	**decay**	103658	11396	
	dEIS			1103

Table 4.1: Showing the parameters determinable for each of the model circuits. "Theoretical" indicates data calculated from known values of circuit components. "Decay" indicates data obtained from fitting the current decay while "dEIS" indicates data obtained from impedance spectra.

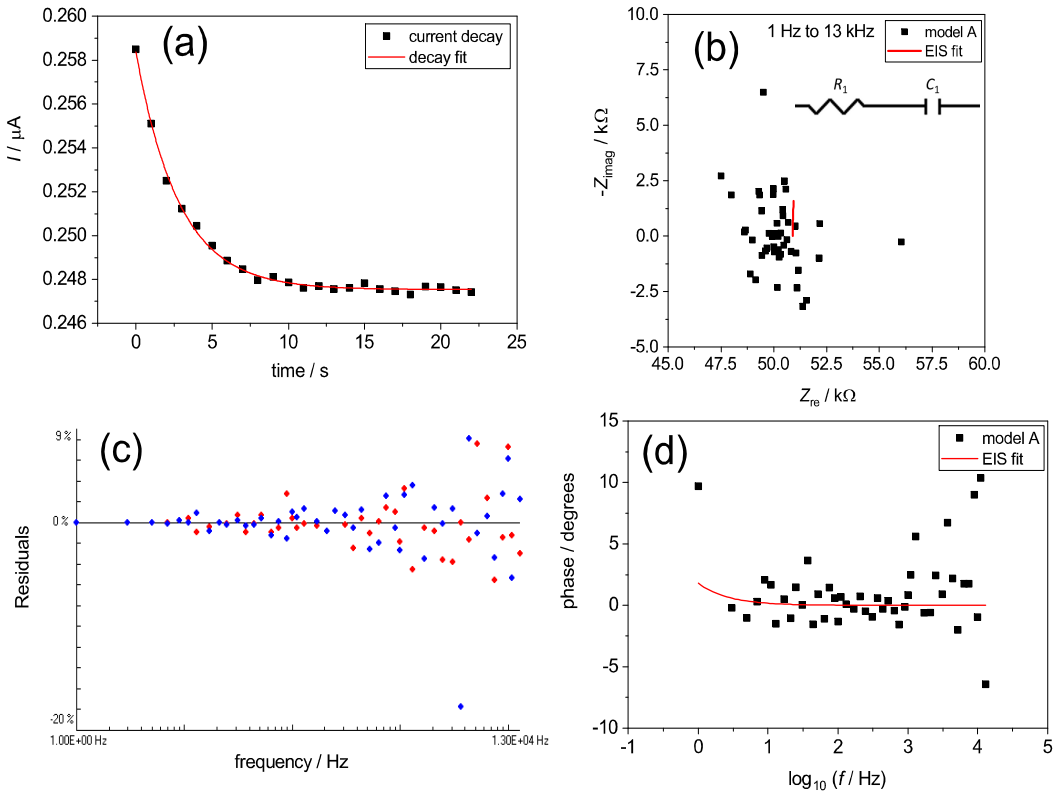

Figure 4.6: Validation of model A whose time constant is 2.8 s. (a) transient current during potential hold at 0.257 V, (b) Impedance spectrum 10 seconds into the hold between 1 Hz and 13 kHz. The spectrum was fitted to the equivalent circuit shown. (c) KK compliance of the admittance of model A, (d) Bode phase plot. Red curves are the fits.

unexpected considering the distortion of the spectrum (fig. 4.6b and d).

4.6.2 Model B

The experiment was repeated for the model B whose time constant is an order of magnitude faster (0.28 s). The time constant measured by fitting the current decay during the potential hold was 0.94 ± 0.18 s (fig. 4.7a, table 4.1). Evidently, this time constant was too fast for the instrument to measure. Additionally only the value of $R_1 + R_2$ could be determined from the calculations using the values obtained from the decay fit. The individual values of R_1 and R_2 could not even be determined approximately.

The circuit parameters, R_1 (5110±7 Ω) and C_1 (101 ± 3 μF) were obtained correctly throughout the sweep-hold (fig. 4.7b, table 4.1) from the impedance spectrum. Fig. 4.7d shows the time dependence of the capacitance during the potential hold at ca. 0.25 V. The value of R_2 could not be determined because the introduction of a second resistor resulted in a bad fit.

4.6.3 Model C

Further measurements were carried out on model C whose time constant is 0.028 s. The time constant (15.6±1.7 s) determined suggests that the instrument is not fast enough to capture the decay (fig. 4.8a, table 4.1).

However, the values of the circuit elements (499.9±0.2 Ω, 94.5±0.3 μF, 604.0±2.1 Ω) were determined correctly from the impedance spectrum (Table 4.1, fig. 4.8b). Fig. 4.8d shows that the capacitance was measured correctly thoughout the hold at ca. 0.25 V. Hence, the correct time constant (0.026±1.7 s) was determined from the impedance spectrum using eq. 4.1. This shows that the time constant 0.028 s may be measured successfully using dEIS in this frequency range (1 Hz to 13 kHz).

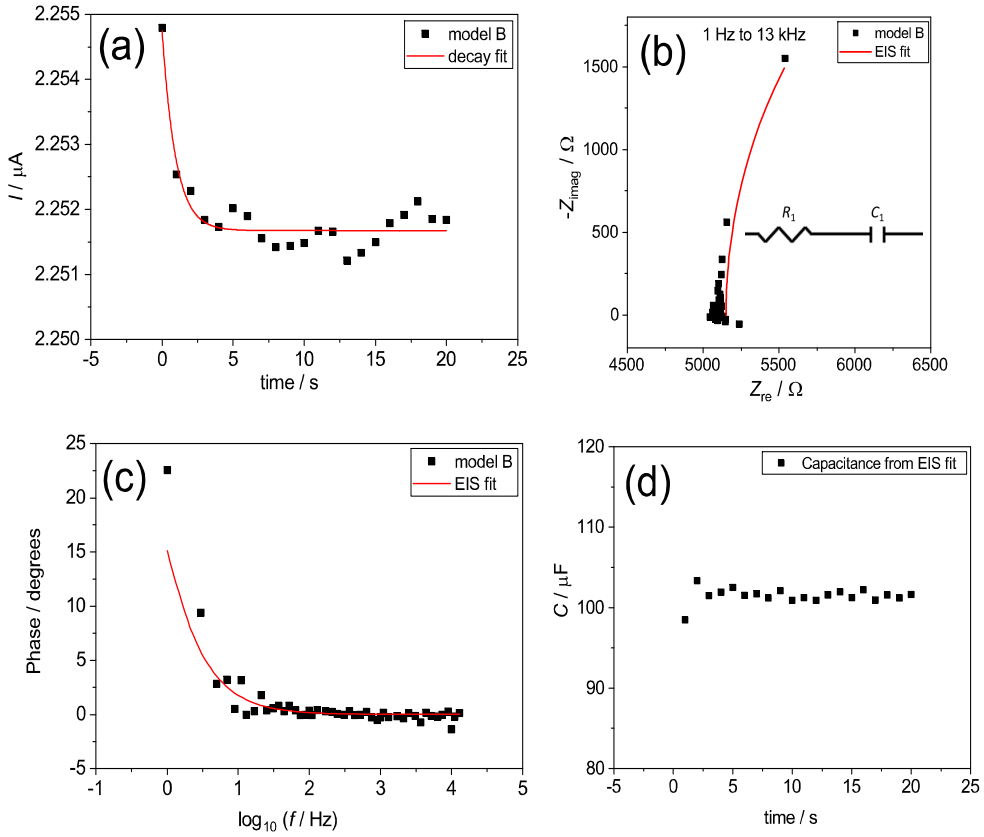

Figure 4.7: Validation of model B whose time constant is 0.28 s. (a). transient current during potential hold at 0.257 V, (b) Impedance spectrum 10 seconds into the hold between 1 Hz and 13 kHz. The spectrum was fitted to the equivalent circuit shown. (c) Bode phase plot, (d) Capacitance vs time. Red curves are the fits.

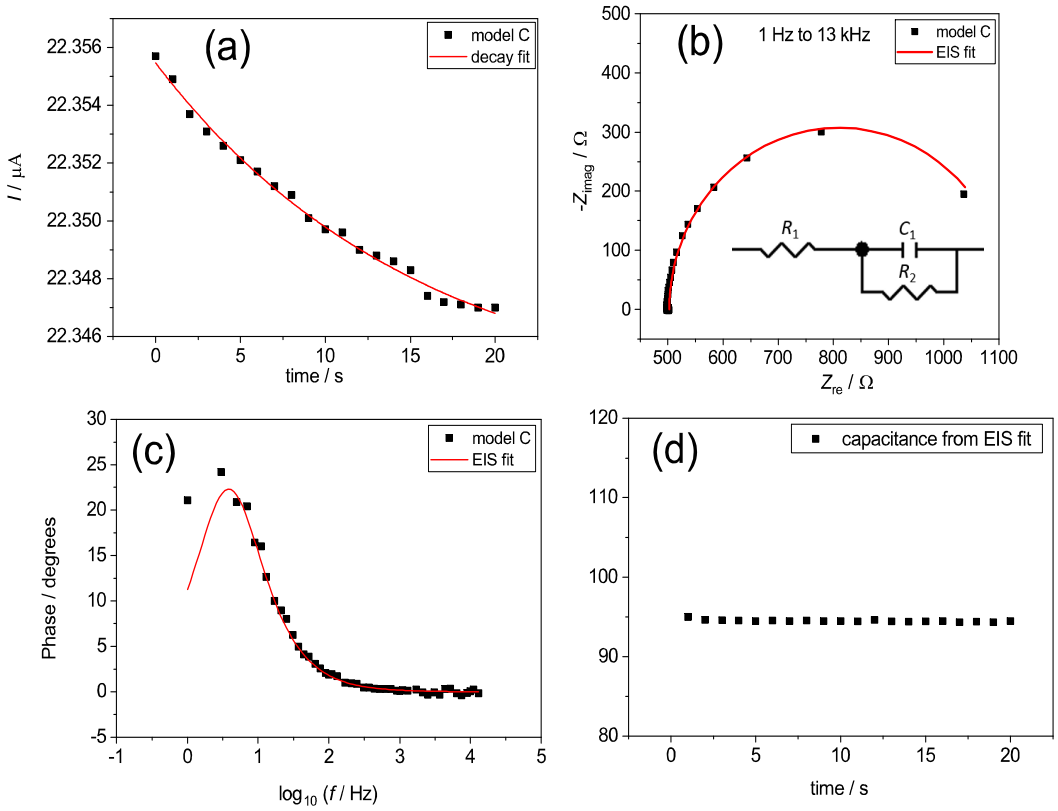

Figure 4.8: Validation of model C whose time constant is 0.028 s. (a) transient current during potential hold at 0.254 V, (b) Impedance spectrum 10 seconds into the hold between 1 Hz and 13 kHz. The spectrum was fitted to the equivalent circuit shown. (c) Bode phase plot, (d) Capacitance vs time. Red curves are the fits.

4.7 Conclusion

In this chapter, the fastest time constant which may be measured during a potential hold using the dEIS instrumentation in the 1 Hz to 13 kHz frequency range was studied. The results showed that in this range, a time constant 0.028 ± 0.06 seconds is determinable from the impedance spectrum in this frequency range. Additionally, since the impedance spectra are featureful, more information may be obtained (compared to what is obtainable from the current decay).

However, for slower systems which are unsuitable for the 1 Hz to 13 kHz range, the current decay may be determined by fitting the current decay. For such slow systems, the fastest time constant which may be determined is around 3 seconds.

Chapter 5

Experimental

5.1 Cell and instrumentation

Experiments were conducted in a three electrode glass cell. Glassware was cleaned overnight in 70 °C sulfuric acid and rinsed prior to experiments with Millipore Milli-Q water. For all experiments described here, semiconductor grade (99.99% purity) KOH from Sigma-Aldrich was used (0.5 M). Nickel wire (0.5 mm diameter, $\geq$ 99.99% purity) from Aldrich was used as working and counter electrodes. For both electrodes, the wire was sealed in Teflon (shrink) tubing from Grainger. The length of the working electrode left in contact with the electrolyte was 0.5 cm, while the counter electrode was estimated to be about 1 cm. The reversible hydrogen electrode (RHE) was used as a reference. It was made by sealing platinum wire (99.997% from Alfa Aesar) in a glass sleeve. The sleeve was filled with 0.5 M KOH and a static hydrogen bubble was generated by negatively polarizing the platinum wire in solution.

The electrolyte was purged for 30 minutes with oxygen-free nitrogen (99.998% pure) from Praxair prior to experiments. The flow of oxygen-free nitrogen was maintained throughout.

5.2 Determination of electrochemically active surface area

The surface of metallic nickel is spontaneously passivated by NiO and β-$Ni(OH)_2$ in KOH and even in moist air. Hence, pretreatment of the electrode is necessary to ensure the surface is free of oxide or hydroxide prior to experiments. Here, the nickel working electrode was electropolished in 50% v/v phosphoric acid (Fischer 70%) at constant current corresponding to ca. 1.8 A/cm^2 for 10 seconds. Afterwards, the electrode was rinsed with Millipore Milli-Q water and transferred to the cell.

Residual oxides were reduced at -0.2 V for 200 s after which a constant potential of 0 V was applied for 50 s in order to remove hydride which may have formed in the metallic nickel [35]. Following pretreatment, voltammograms between -0.15 and 0.5 V were run to determine the electrochemical surface area.

Additionally, to ensure the now metallic nickel surface was not aged to β-$Ni(OH)_2$, the working electrode was always controlled at 0 V after the sequence above was run, and prior to impedance experiments. The steps above were controlled using the Gamry Ref600 potentiostat's sequencing feature.

A critical discussion appears later in this work on the surface area correction. However, for all the results described here, 514 $\mu C/cm^2$ was assumed to correspond to a coverage of one monolayer (ML) and is used in calculating the electrochemical surface area. The anodic charge corresponding to the formation of α-$Ni(OH)_2$ (up to 0.5 V) was integrated and then divided by 514 $\mu C/cm^2$ to obtain the electrochemical surface area. The roughness factor of the electrodes here was ca. 1.5.

5.3 dEIS conditions

The generation and detection of the AC signals and conversion to impedance was done with a KUSB-3116 data acquisition system from Keithley and custom software as previously described by Sacci and Harrington [28,29,109]. The AC + DC potential was applied to the cell using a Gamry Ref600 potentiostat.

The multisine comprised 46 frequencies which added up to 30 mV amplitude (4.064 mV (rms) or less per frequency). The multisine was added to a slow sweeping potential and applied to the cell.

Data was sampled continuously and simultaneously on three channels recording the DC potential, AC potential and AC +DC current. Fourier analysis was performed on the potential and current to give the impedance spectra which were fitted to equivalent circuits later. Using this method, impedance was determined along the potential sweep.

The frequency range sampled here was 1 Hz to 13 kHz. The minimum frequency was chosen to be 1 Hz when a sweep rate of 5 mV s^{-1} was used per the rules earlier discussed.

5.4 Sweep-hold-sweep experiments

The transformation of the surface oxide/hydroxide is studied here by measuring impedance during the slow sweeping potential. The potential was swept upward from 0 V to selected potentials between 0.5 and 1.0 V at 5 mV s^{-1} and held there for 2 minutes. Recall that α-$Ni(OH)_2$ converts to β-$Ni(OH)_2$ in this region [25, 30–35]. Afterwards, the potential was swept back to -0.15 V (fig. 5.1a). In other experiments where reduction of β-$Ni(OH)_2$ was of interest, the potential was held at -0.25 V, -0.2 V, -0.1 V in the cathodic sweep of the first cycle (fig. 5.1b). The subsequent sweep

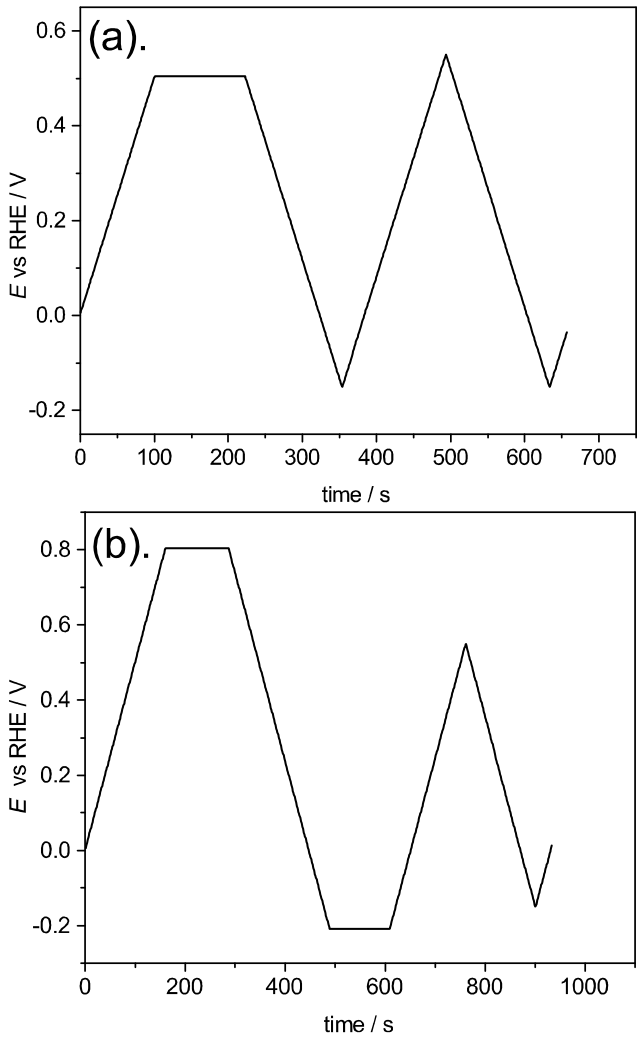

Figure 5.1: Sweep-hold-sweep experiments in 0.5 M KOH at 5 mV s^{-1}: (a) Holding at positive potential (e.g. 0.5 V) for 2 min, (b) Holding at positive (e.g. 0.8 V) and negative potential (e.g. -0.2 V).

between -0.15 and 0.55 V was compared to the first cycle for all the experiments described.

Note that the species generated at 0.5 V $< E <$ 1.2 V is described as β-Ni(OH)$_2$ purely for simplicity. It is perhaps more accurate to view the surface species as comprising different ratios of α : β-Ni(OH)$_2$ depending on the anodic potential. Earlier, it was also shown that NiO is expected to be a minor component of the film irrespective of anodic potential.

5.4.1 Baseline corrections

In this work, the effects of no baseline (shown as none here), internal baseline correction and extrapolation (already defined in section 3.2.3) were compared. Extrapolation and no baseline give comparable results for the impedance spectra when applied to the experimental data. Internal baseline resulted in noise glitches in the impedance spectra. Hence, charge transfer resistance and capacitance extracted from these noisy impedance spectra were deemed inaccurate (fig. 5.2 and fig. 5.3). Therefore, extrapolation was subsequently used for all the experiments described in this work. Note that for the current decay, all three baseline correction algorithms give the same current during the sweep and throughout the potential hold (fig. 5.3b).

5.4.2 Equivalent circuits

Complex non-linear least squares fitting was implemented in Maple. Experimental data was fitted to a function of frequency using the nonlinear simplex method [114]. The procedure is available through the Maple website [114]. The quality of fit was assessed by comparing AICc obtained for the proposed equivalent circuits [114, 117].

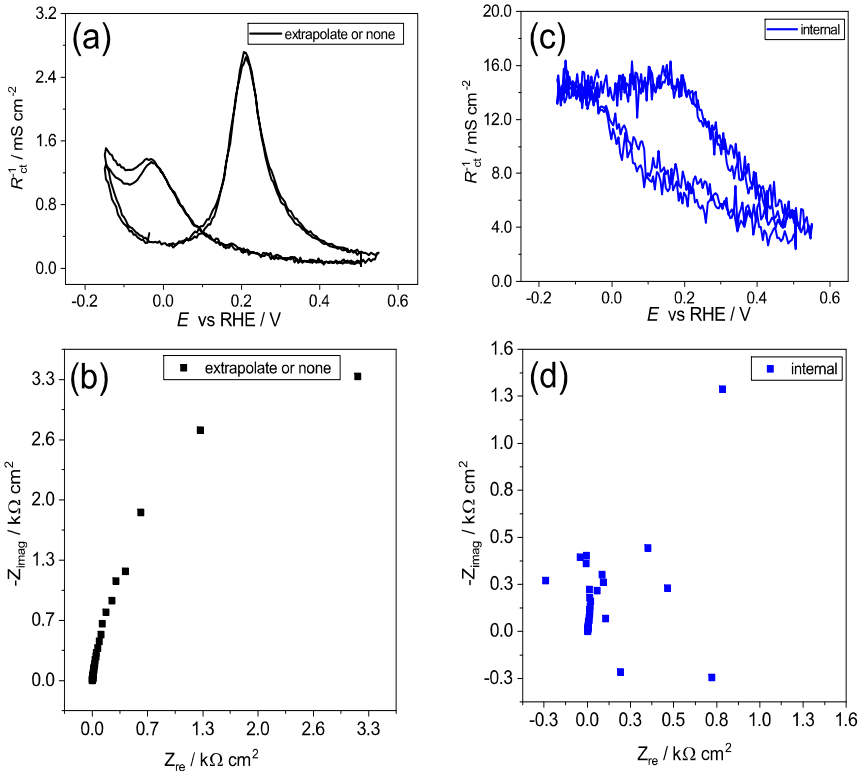

Figure 5.2: Distortion in impedance spectra and extracted charge transfer resistance as a result of baseline effects. (a) R_{ct}^{-1} vs potential between -0.15 V and 0.55 V, (b) Nyquist plot at 0.5 V obtained from extrapolation and no baseline correction, (c) R_{ct}^{-1} vs potential between -0.15 V and 0.55 V, (d) Nyquist plot at 0.5 V obtained from internal baseline correction at 5 mV s^{-1} in 0.5 M.

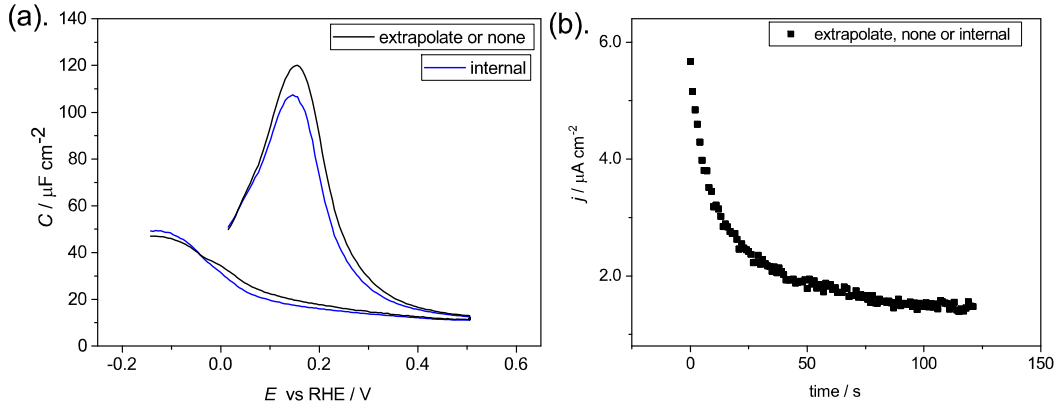

Figure 5.3: Effect of baseline correction on capacitance and current decay. (a) Capacitance obtained between -0.15 and 0.55 V in 0.5 M at 5 mV s^{-1}, (b) current decay during potential hold at 0.5 V for 2 min.

All data represented here were fitted to the circuit 5.1.

$$Z = R_s + \frac{1}{2\pi i f C_{dl} + \frac{1}{R_{ct}}} \qquad \text{RCR} \qquad (5.1)$$

$$Z = R_s + \frac{1}{2\pi i f C_{dl}} \qquad \text{RC} \qquad (5.2)$$

Here Z is the impedance, R_s is the solution resistance, C_{dl} is the capacitance, and R_{ct} is the charge transfer resistance. Magnitude exponential (magexp) weighting was used to optimize fits since it minimizes the AICc and produces the lowest standard error for the parameters to be determined (table 5.1).

However, over the 0.6 V to 1.0 V potential range, the low frequency intercept was not as obvious. Hence, AICc obtained for circuit 5.1 and circuit 5.2 were compared in order to justify the use of the former at those potentials (table 5.2).

Fits with more negative AICc were chosen. Evidence from the data presented in table 5.2 and table 5.1 justify the use of circuit 5.1 as well as the magexp weighting scheme.

potential / mV	**weighting**	**AICc**	C_{dl} / μ**F cm**$^{-2}$	R_{ct} / Ω **cm**^{2}
101	Magexp	757	94.1±2.6	1879±309
	Magtheory	763	85.3±2.3	2184±425
	Propexp	813	91.4±5.1	1709±305
201	Magexp	859	88.4±4.4	385±51
	Magtheory	884	69.3±3.1	770±127
	Propexp	888	92.2±6.1	432±76
301	Magexp	953	28.8±1.0	1110±114
	Magtheory	964	24.8±0.8	1713±202
	Propexp	981	29.7±1.5	996±136
401	Magexp	983	16.6±0.4	2836±256
	Magtheory	986	15.2±0.3	3697±371
	Propexp	1022	16.6±0.8	2465±311
501	Magexp	996	13.1±0.2	5117±480
	Magtheory	995	12.2±0.2	6173±618
	Propexp	1047	13.1±0.6	4339±570

Table 5.1: Dependence of AICc parameter on weighting scheme.

potential / mV	**RCR**		**RC**	
	AICc	C_{dl} / μ**F cm**$^{-2}$	**AICc**	C_{dl} / μ**F cm**$^{-2}$
100	690	91.9±1.8	717	93.4±2.1
200	749	127.2±4.3	806	152.7±6.9
300	889	41.4±1.3	986	52.9±3.05
500	946	16.1±1.1	1082	2.42±0.10
701	952	14.4±0.2	1081	16.2±0.6
804	960	15.3±0.2	1005	15.9±0.3
-67	929	22.6±0.6	1146	57.7±7.3
-150	809	29.5±0.7	1111	420.4±179.6

Table 5.2: Comparison of AICc for the two equivalent circuits considered for fitting experimental results.

Chapter 6

Results and discussion

6.1 Results

6.1.1 Cyclic voltammetry

Cyclic voltammograms were obtained from the DC potential and current. The redox behavior of nickel has already been studied using cyclic voltammetry [34,59,98]. Therefore as a first step, it was important to ensure that the cyclic voltammograms obtained in this work matched previously reported evidence of nickel redox behavior described in sections 2.1 and 2.5.

The interconversion of α- to β-$Ni(OH)_2$ was assessed by comparing the α-$Ni(OH)_2$ anodic charge in the first and second cycles. This method was used because between 0.5 V and 1 V, where the electrochemical conversion of α- to β-$Ni(OH)_2$ occurs, a small current plateau is observed. After prolonged polarization in this region, the current falls to very small values which are not accurately determinable [37]. Hence, it was more reliable to quantify the amount of β-$Ni(OH)_2$ indirectly by comparing the change in the α-$Ni(OH)_2$ peak charge. However, the α-$Ni(OH)_2$ anodic charge was only compared between 0.15 V and 0.3 V because of the contributions of hydrogen

adsorption current (0 V and 0.1 V) anticipated in the second cycles at 5 mV s^{-1}. Further discussion on this appears in section 6.2.1.

The α-$Ni(OH)_2$ anodic charge between 0.15 V and 0.3 V was expected to decrease in the second cycle when significant α- to β-$Ni(OH)_2$ conversion occurred (0.6 V - 1.0 V) during the two minute hold in the first cycle. However, at < 0.5 V where no significant α- to β-$Ni(OH)_2$ conversion occurs, the anodic charge was expected to remain the same. Note that this method assumes that β-$Ni(OH)_2$ is not significantly reduced by sweeping the potential to -0.15 V.

Fig. 6.1 shows holding experiments between 0.5 V and 1 V. When the potential was held at 0.5 V, the anodic charge in the subsequent sweep was unchanged. However, once the potential was swept and held at potentials higher than 0.5 V, the α-$Ni(OH)_2$ anodic charge decreased in subsequent cycles. The anodic charge in the second cycle decreased as the holding potential increased. This implies that the conversion α-$Ni(OH)_2$ to β-$Ni(OH)_2$ proceeds at a faster rate at higher potentials.

In fig. 6.2, the effect of holding at negative potentials on the reduction of β-$Ni(OH)_2$ was studied. In fig. 6.2a, the potential was initially held at 0.8 V for two minutes. On the cathodic sweep, the potential was held at -0.1 V. The α-$Ni(OH)_2$ anodic charge was not recovered in the subsequent cycle. This suggests β-$Ni(OH)_2$ was not reduced. Fig. 6.2b shows that when the potential was held at -0.2 V instead, the α-$Ni(OH)_2$ anodic charge recovers. However, when the potential was held at 1 V prior to the cathodic hold at -0.2 V, the β-$Ni(OH)_2$ was only partially reduced (Fig. 6.2c).

The formation of the β-$Ni(OH)_2$ also coincides with an increase in the hydrogen evolution activity. In fig. 6.1, the current density during the cathodic sweeps between 0 V to -0.15 V increased significantly after the potential was held at potentials higher than 0.5 V. This increased catalysis of hydrogen evolution by β-$Ni(OH)_2$ relative to α-$Ni(OH)_2$ already appears in the literature [23–26].

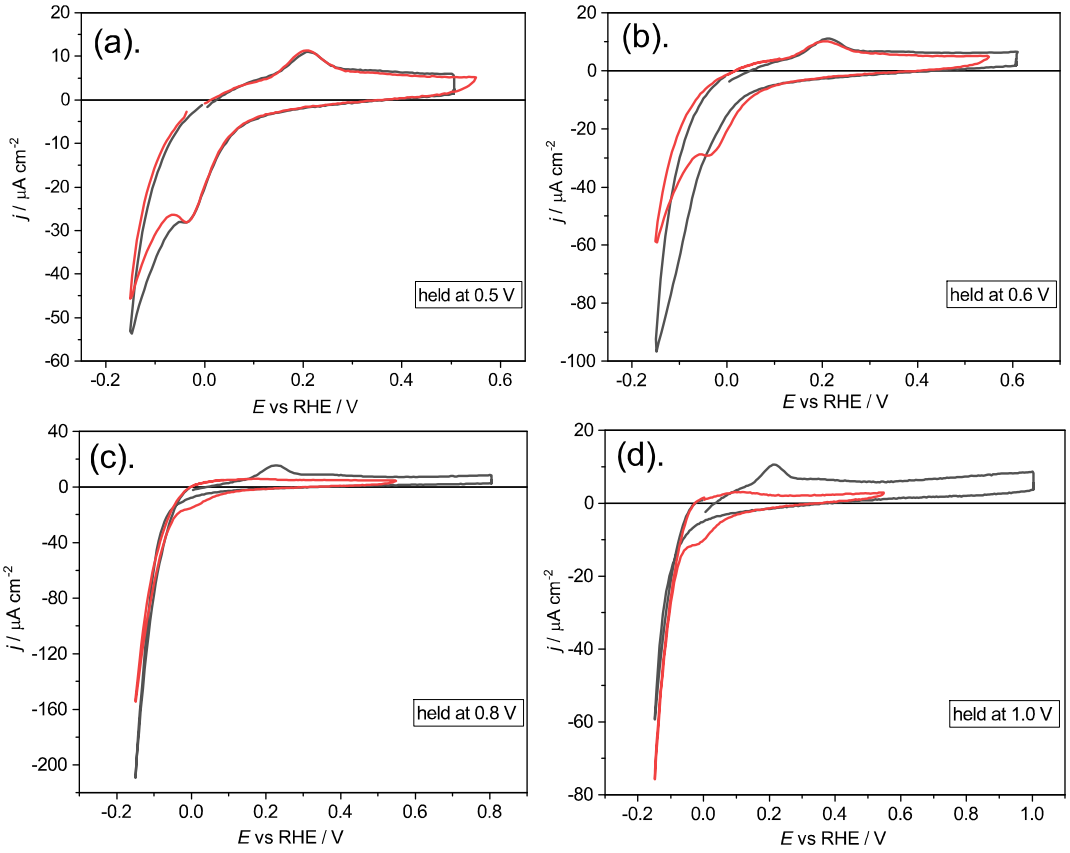

Figure 6.1: Cyclic voltammograms for sweep-hold-sweep experiments in 0.5 M KOH at 5 mV s^{-1}. (a) held at 0.5 V, (b) held at 0.6 V, (c) held at 0.8 V, (d) held at 1.0 V for 2 mins in the first cycle (black) and uninterrupted second sweeps (red) between -0.15 V and 0.55 V.

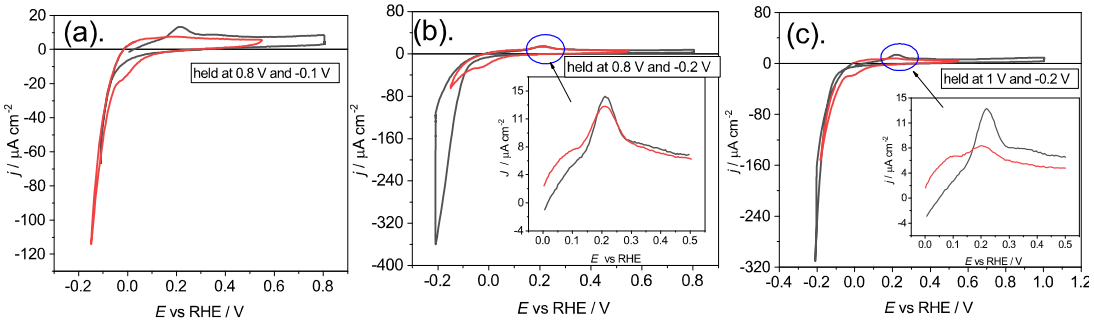

Figure 6.2: Cyclic voltammograms for sweep-hold-sweep experiments in 0.5 M KOH at 5 mV s^{-1} contd. (a) held at 0.8 V and -0.1, (b) held at 0.8 V and -0.2 V, (c) held at 1 V and -0.2 V for 2 mins in the first cycle (black) and uninterrupted second sweeps (red) between -0.15 V and 0.55 V.

Additionally, fig. 6.2b shows that once reduction of β-$Ni(OH)_2$ was accomplished at -0.2 V, the increased hydrogen evolution activity subsided. However, since β-$Ni(OH)_2$ was only partially reduced in fig. 6.2c, the increased catalysis of hydrogen evolution activity remains, albeit to a lesser extent.

A shoulder emerges around 0 V in the second cycle once the potential is swept beyond 0.5 V in the first cycle.

6.1.2 Capacitance

The capacitance, charge transfer resistance and solution resistance were obtained by fitting the impedance to circuit 5.1.

Here an increase in capacitance is assumed to correspond to the adsorption of OH^- (between 0 V and 0.4 V) or hydrogen (between 0 V and -0.25 V) onto the nickel substrate. A plateau in capacitance at a minimum value suggests that the nickel substrate is fully covered by $Ni(OH)_2$ and no further adsorption onto the nickel substrate occurs. Hence, capacitance increases as nickel is oxidized to α-$Ni(OH)_2$. Since α-$Ni(OH)_2$ is reduced back to metallic nickel by sweeping to -0.15 V, the peak capac-

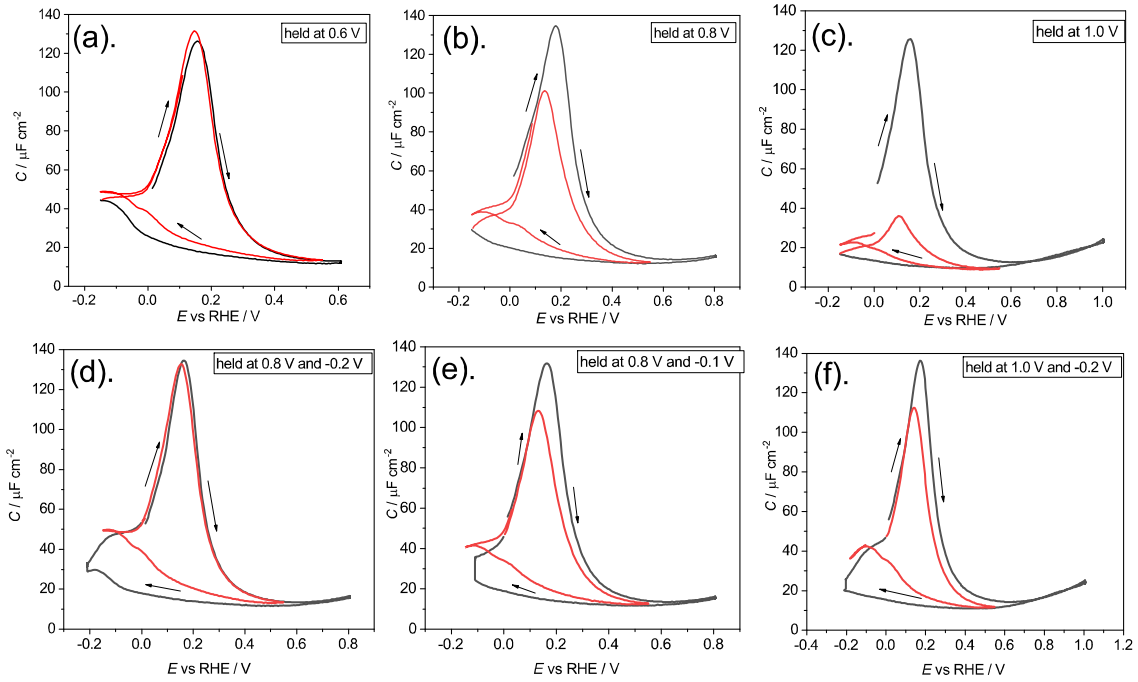

Figure 6.3: Dependence of capacitance on hold potential in 0.5 M KOH at 5 mV s^{-1}: (a) held at 0.6 V, (b) held at 0.8 V, (c) held at 1 V, (d) held at 0.8 V and -0.2 V, (e) held at 0.8 V and -0.1 V, (f) held at 1 V and -0.2 V for 2 mins in the first cycle (black) and uninterrupted second cycles between -0.15 V and 0.55 V (red).

itance is expected to be reproduced in the subsequent sweep provided the potential is kept below 0.6 V in the first cycle. However, once the potential is swept higher than 0.6 V and significant α-to β-$Ni(OH)_2$ conversion ensues, the peak capacitance is expected to decrease in the subsequent cycle since β-$Ni(OH)_2$ is not reduced by sweeping to -0.15 V.

Fig. 6.3 shows that the oxidation of the metallic nickel surface to α-$Ni(OH)_2$ between 0 V and 0.2 V coincides with an increase in capacitance as α-$Ni(OH)_2$ builds. The capacitance attains a maximum of 120 ± 4 μF cm^{-2} at 0.15 ± 0.03 V, after which it decreases until it plateaus at 15 ± 4 μF cm^{-2}. The capacitance maximum occurs at the same potential as the current maximum observed in figs. 6.1 and 6.2.

At 0.6 V no appreciable conversion from α-Ni(OH)$_2$ to β-Ni(OH)$_2$ occurs. Hence, holding at 0.6 V for 2 minutes did not result in a change in the peak capacitance in the subsequent sweep (fig. 6.3a) since α-Ni(OH)$_2$ is reduced at -0.15 V. However, β-Ni(OH)$_2$ is not reduced by sweeping to -0.15 V. Hence, fig. 6.3b shows that holding at 0.8 V, where appreciable α-Ni(OH)$_2$ to β-Ni(OH)$_2$ occurs, resulted in a decrease in peak capacitance in the subsequent sweep. A more drastic decrease in the peak capacitance occurred when the potential was held at 1 V, which effectively shows the potential dependence of the conversion of the α-Ni(OH)$_2$ to β-Ni(OH)$_2$ (fig. 6.3c).

Fig. 6.3d shows that after the potential was held at -0.2 V for 2 minutes, the capacitance returned to its peak value at 0.2 V in the subsequent cycle. This implies the β-Ni(OH)$_2$ is reduced at -0.2 V. However, fig. 6.3e shows that holding at -0.1 V did not result in the recovery of the peak capacitance. Similarly, after the potential was swept to 1 V and held for 2 minutes, holding at -0.2 V only resulted in a partial recovery of the capacitance maximum (fig. 6.3e). This suggests the conversion α-Ni(OH)$_2$ to β-Ni(OH)$_2$ at 1 V is faster than its subsequent reduction at -0.2 V.

Typically, the capacitance increases slightly between 0 V and -0.2 V during the cathodic scan. In fig. 6.3a, the capacitance peaks at 45 $\pm$ 1 μF cm^{-2} during the cathodic scan. However, this slight capacitance increase was inhibited when the potential was held at 0.8 V and 1 V (fig. 6.3b and fig. 6.3c) in the previous anodic scan. In fact, it only attains 29 μF cm^{-2} and 16 μF cm^{-2} respectively. Fig. 6.3d shows that when the potential was held at -0.2 V, the capacitance increased to 49 μF cm^{-2} in the subsequent cathodic sweep.

6.1.3 Charge transfer resistance

The charge transfer resistance (R_{ct}) is the diameter of the highest frequency semicircle, which is the only semicircle in this case. Over the course of a full sweep between -0.25 V and 0.8 V, fig. 6.4a shows how the charge transfer conductance (

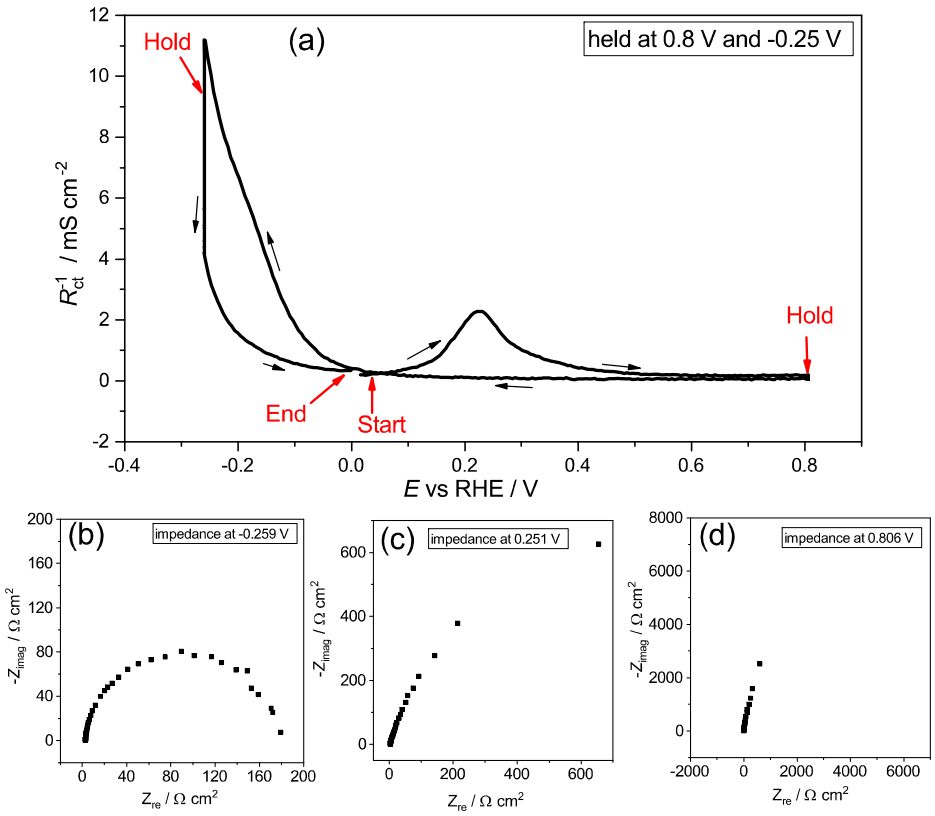

Figure 6.4: Comparison of charge transfer resistance along the potential sweep between -0.25 V and 0.8 V in 0.5 M KOH at 5 mV s^{-1}. (a) R_{ct}^{-1} vs potential and impedance at (b) -0.259 V, (c) 0.251 V and (d) 0.806 V.

R_{ct}^{-1}) changes. A higher value of the conductance indicates a faster process. Hence, it may be inferred that the processes occurring during the potential hold at -0.259 V are faster than those at 0.8 V.

The Nyquist plots (figs. 6.4b-d) show the impedance at 0.806 V (where significant α- to β-$Ni(OH)_2$ conversion takes place), at 0.251 V (around the peak of current density of α-$Ni(OH)_2$) and at -0.259 V (where hydrogen evolution and the reduction of β-$Ni(OH)_2$ occurs). Here, a smaller diameter (R_{ct}) indicates a faster process. The smallest R_{ct} was measured during the hold at -0.259 V. This also suggests that the process which occurs at -0.259 V is fast compared to the processes at 0.251 V and 0.806 V. Although full semicircles were not observed at 0.806 V and 0.251 V, it was inferred from the magnitude of the charge transfer resistance that the processes occuring at 0.251 V are faster.

The relationship between increased hydrogen evolution current and the formation of β-$Ni(OH)_2$ at > 0.5 V was investigated. As a control experiment, the potential was held at 0.5 V in the first cycle (fig. 6.5a). At this potential, only a relatively small amount of β-$Ni(OH)_2$ is expected. The lower potential limit of -0.15 V was chosen to limit hydrogen evolution. Over the -0.15 V to 0.55 V range, α-$Ni(OH)_2$ dominates and was easily reduced without holding at negative potentials. Predictably the charge transfer resistance was not significantly altered over the two cycles. When the potential was held at 0.8 V, where the conversion to β-$Ni(OH)_2$ is significant, the conductance at -0.15 V was significantly higher than in the previously described case (fig. 6.5b). Noticeably, the conductance at the α-$Ni(OH)_2$ peak decreased in the subsequent cycle, since β-$Ni(OH)_2$ was not significantly reduced by simply sweeping to -0.15 V.

Holding at -0.1 V resulted in partial reduction of the β-$Ni(OH)_2$ (fig. 6.5c). This was evident in the reduction in conductance at the α-$Ni(OH)_2$ peak. In the subsequent negative-going sweep, the conductance remains significantly higher at -0.15 V than in the control experiment. However, when the potential was held at -0.25 V following

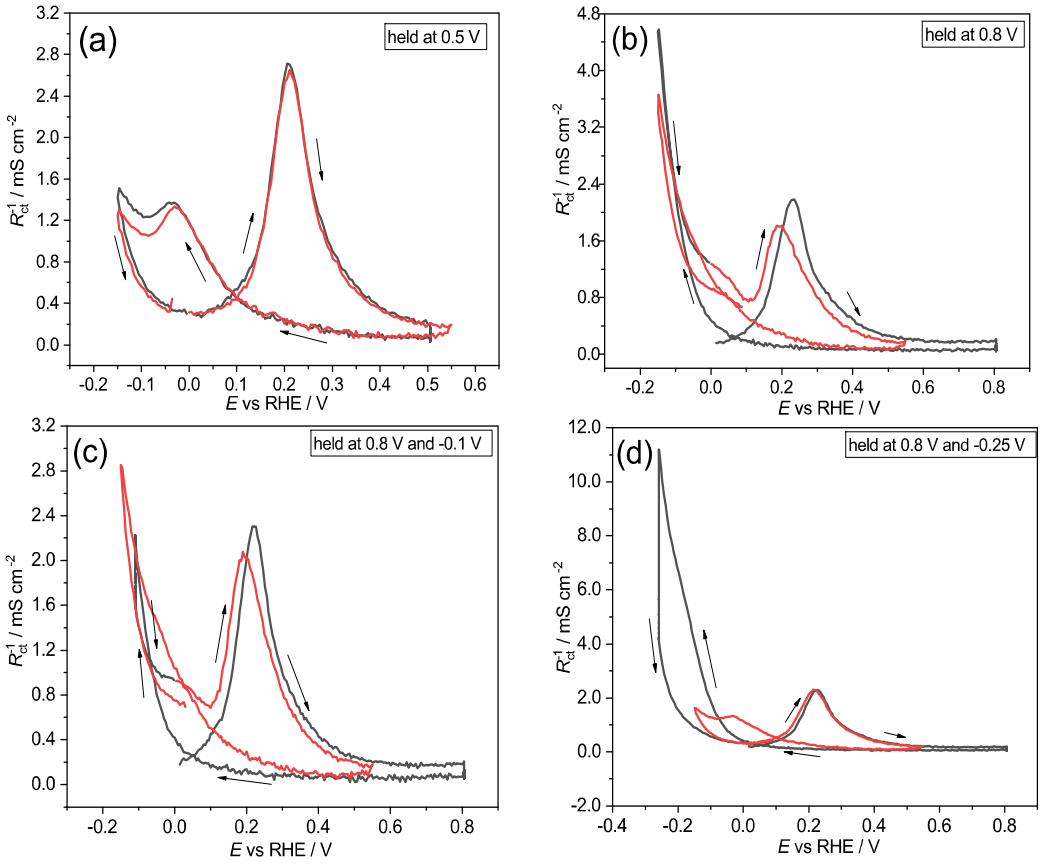

Figure 6.5: Dependence of R_{ct}^{-1} on hold potential in 0.5 M KOH at 5 mV s^{-1}. (a) held at 0.5 V, (b), held at 0.8 V, (c) held at 0.8 V and -0.1 V, (d) held at 0.8 V and -0.25 V in the first cycle (black). Second cycle between -0.15 Vand 0.55 V (red).

E / **V**	**0.8**	**-0.1 (time $<$ 25 s)**	**-0.2**
I_∞ / μA	4.12	-8.7	-1.48
I_1 / μA	6.10	1.16	-28.18
τ / s	18.4±0.4	5.4±0.2	31.7±0.7
R-square	0.9871	0.9968	0.9933

Table 6.1: Time constants extracted by fitting current during 2 minute holds at 0.8 V, -0.1 V and -0.2 V. Note that only the first 25 seconds of the hold at -0.1 V could be fitted to an exponential decay.

the hold at 0.8 V, conductance over the α-Ni(OH)$_2$ peak was unchanged (fig. 6.5d). Having reduced the β-Ni(OH)$_2$ completely, conductance at -0.15 V returned to a value which is more consistent with α-Ni(OH)$_2$ (compare red curves in fig. 6.5a and fig. 6.5d).

6.1.4 Time constant

Time constants were determined by fitting the current acquired during potential holds. Fitting was done using a built-in one step exponential decay function in Origin® according to eq. 4.8.

Current and capacitance decays were fitted for holding experiments at 0.8 V, -0.2 V and -0.1 V are shown in fig. 6.6. When the potential was held at 0.8 V for 2 minutes, the time constant was about 18 seconds. Over this period, the capacitance decreases (fig. 6.6a). However, when the voltage was held at -0.2 V afterwards, the magnitude of the current decreases exponentially, and the capacitance increases exponentially. The current decay shows that the reduction of β-Ni(OH)$_2$ occurs with a time constant of 30 seconds (fig. 6.6b).

Holding at -0.1 V, where β-Ni(OH)$_2$ is expected to persist produces less straightforward behavior. The capacitance increases over the the period of the potential hold, suggesting slow partial reduction of the β-Ni(OH)$_2$. However, the current increases rapidly (time constant was 5.4 $\pm$ 0.2 seconds) in the early stages, followed by an

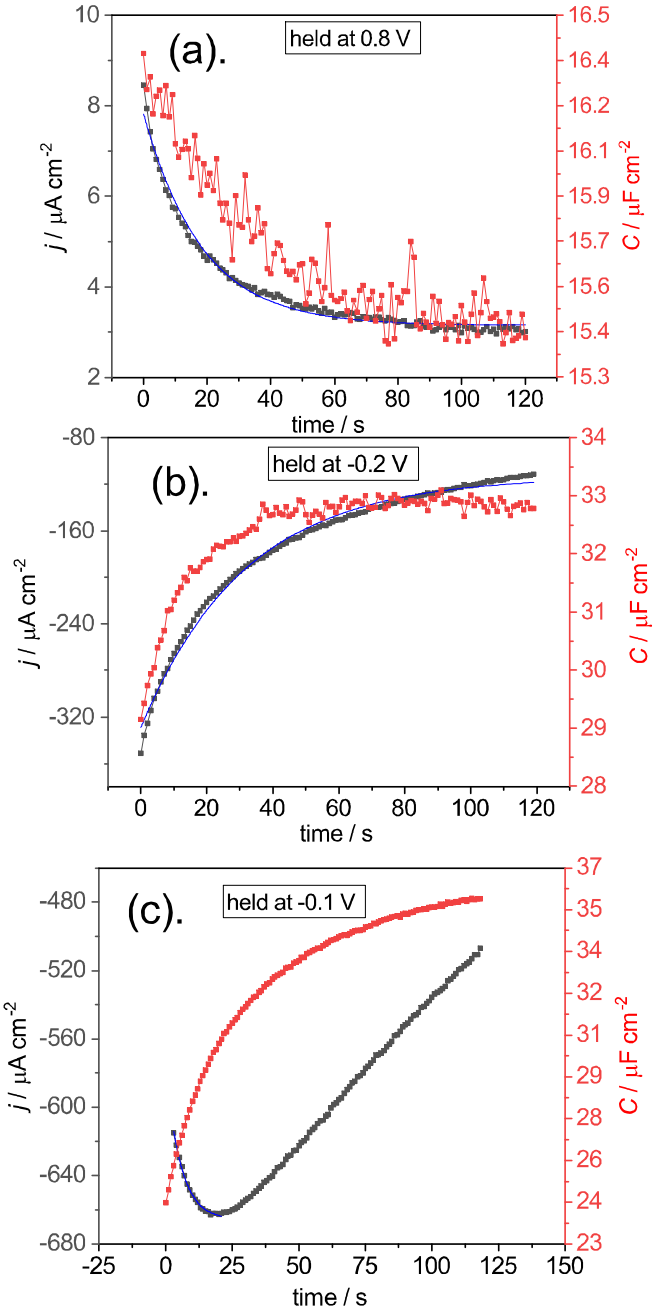

Figure 6.6: Transient current and capacitances obtained for different stages of nickel electrooxidation. (a) 0.8 V for 2 min showing α- to β-$Ni(OH)_2$, (b) -0.2 V for 2 min showing reduction of β-$Ni(OH)_2$, (c) -0.1 V for 2 min in 0.5 M KOH at 5 mV s^{-1}. Blue curve shows the fit for the transient current.

Hold potential / V	**charge density / μC cm^{-2}**	**thickness / Å**
first cycle		
0.5 (no hold)	607	7
0.5	876	10
0.6	1050	12
0.8	1803	21
1.0	2062	24
Second cycle		
0.5	682	8
0.6	628	7
0.8	598	7
1.0	308	4

Table 6.2: Dependence of coverage on hold potential.

almost linear decay.

6.2 Discussion

6.2.1 Growth of $Ni(OH)_2$ Layer

Table 6.2 shows the thickness of the layer(s) of $Ni(OH)_2$ formed by holding at different potentials between 0.5 V and 1.0 V for 2 minutes. The thickness (d) of $Ni(OH)_2$ formed during the potential sweep and hold was estimated using the formula

$$d = \frac{QM\rho}{2F} \tag{6.1}$$

where Q is the charge density, M is the molar mass of $Ni(OH)_2$ (92.708 g mol^{-1}), ρ is the density of $Ni(OH)_2$ (4.10 g cm^{-3}) and F is Faraday's constant. Note that this method inherently assumes that the $Ni(OH)_2$ formed is a film of bulk material.

The charge density was obtained by integrating the entire anodic charge in the first cycle of each sweep in Origin®. In the case of the 0.5 V (no hold) value, the charge was only integrated up to 0.5 V without the inclusion of the two minute

hold. Table 6.2 shows that $Ni(OH)_2$ grows as the potential is swept and held at increasingly anodic potentials in the first cycle. The number of monolayers observed here is consistent with coverage suggested elsewhere when the potential is kept below 0.5 V [34, 36, 101]. Beden and coworkers deduced that 4 -5 monolayers of $Ni(OH)_2$ forms during the transformation of α- to β-$Ni(OH)_2$ between 0.5 V and 1.0 V [34]. Additionally, Alsabet et al. obtained a thickness of ca. 25 Å for polycrystalline nickel electrodes held at 0.8 V for 100 seconds [37].

In the second cycle, the reduction in current density at the α-$Ni(OH)_2$ peak is counteracted by the additional current contributed by hydrogen desorption between 0 and 0.1 V (fig. 6.1 and fig. 6.2) [15, 23–25, 54, 57–61]. Hence, although the current density decreases at the α-$Ni(OH)_2$ peak, it is only at 1.0 V where the catalysis of the hydrogen evolution appears to stall, that the expected reduction in current density is attained.

Therefore, comparison of the charge between 0 and 0.5 V between the first and second cycles is misleading at first glance. However, once the charge was integrated over a smaller range (0.15 and 0.3 V), where the contribution from the hydrogen desorption is minimized, the reduction in the anodic charge was more evident. The reduction in the capacitance and the evolution of the charge transfer resistance in the second cycle provided justification for this assumption (fig. 6.3b,c and fig. 6.3).

6.2.2 Nature of $Ni(OH)_2$ Layer

Comparison of the thicknesses obtained in table 6.2 to those previously reported in the literature (table 2.1) suggests only a few monolayers were formed between 0.5 V and 1 V at 5 mV s^{-1}. Estimation of the number of monolayers formed at 1 V, assuming one monolayer is equivalent to 8.0 Å (the length of the c lattice parameter of α-$Ni(OH)_2$ [1]), suggests that only about 2.8 monolayers were formed. With so few monolayers, it is unlikely that $Ni(OH)_2$ adsorbed on the nickel surface between 0.5

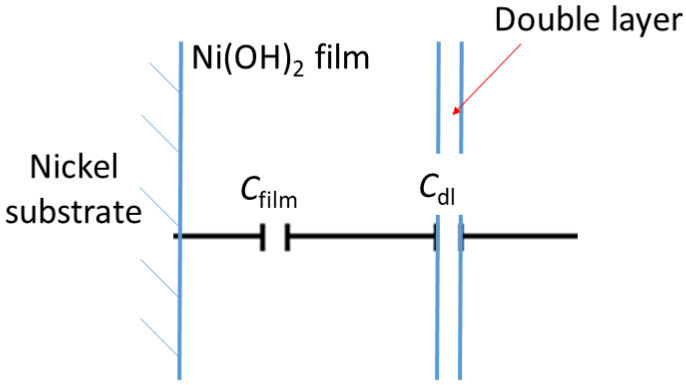

Figure 6.7: Modelling of the $Ni(OH)_2$ as a film.

V and 1 V coalesces to form a film. Nonetheless, the suitability of this model to the experimental data is discussed next.

Film model

Fig. 6.7 is an equivalent circuit describing the relationship between the pseudo-capacitance of $Ni(OH)_2$ ($C_{Ni(OH)_2}$) and the double layer capacitance (C_{dl}). In order to decide if the film model explains the experimental data, $C_{Ni(OH)_2}$ was estimated from the dielectric constant using eq. 6.2.

$$C_{Ni(OH)_2} = \frac{\varepsilon_{film}\varepsilon_0}{d} \tag{6.2}$$

$$\frac{1}{C} = \frac{1}{C_{Ni(OH)_2}} + \frac{1}{C_{dl}} \tag{6.3}$$

Here C is the capacitance per unit area (as elsewhere in the thesis), ε_{film} is the dielectric constant of the film, ε_0 is the permittivity of vacuum, while d is the thickness of the film. In the absence of tabulated dielectric constants for $Ni(OH)_2$, the dielectric constant of NiO (11.9) [120, 121] was assumed be a good approximation of ε_{film}.

When ε_{film} was assumed to be 11.9 (no contributions from intersheet water in

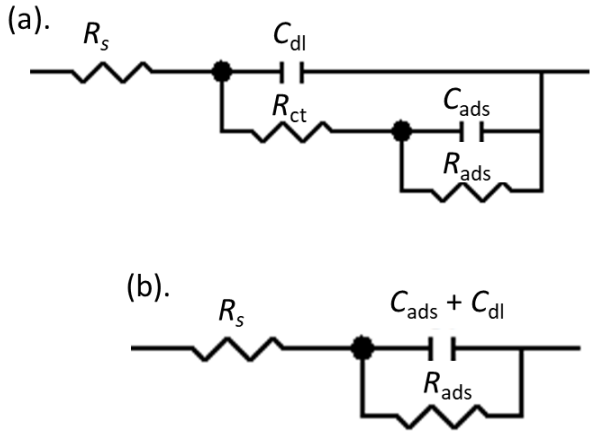

Figure 6.8: Modelling the adsorption of $Ni(OH)_2$. (a) Armstrong and Henderson circuit. (b) Simplification of the Armstrong and Henderson circuit when R_{ct} is small.

$Ni(OH)_2$), the capacitances obtained were 10 μF cm^{-2} and 5 μF cm^{-2} after two minute holds at 0.5 V and 0.8 V respectively. On the other hand, when the ε_{film} was assumed to be 80 (dominated by the intersheet water in $Ni(OH)_2$), 69 μF cm^{-2} and 34 μF cm^{-2} were obtained, having held at 0.5 V and 0.8 V respectively.

These estimates need to be combined in series with the double layer capacitance, which is estimated at 15 $\pm$ 4 μF cm^{-2} from fig. 6.3. Since the series combination is smaller than the of the two capacitors, the resulting capacitance must be much less than the measured value of 120 μF cm^{-2} obtained at 0.15 V (fig. 6.3a). Hence, the proposition of a film based on this model fails to account for the experimental data. The suitability of an adsorption model is investigated next.

Adsorption model

The adsorption of $Ni(OH)_2$ may be modelled using the fig. 6.8a, where, R_s is the solution resistance, C_{dl} is the double layer capacitance, R_{ct} is the charge transfer resistance across the electrode / electrolyte interface while C_{ads} and R_{ads} are the

pseudocapacitance and pseudoresistance due to the $Ni(OH)_2$ adsorbate.

If R_{ct} is assumed to be small such that the capacitances can be combined in parallel, fig. 6.8a simplifies to fig. 6.8b. In practice, the parameters extracted from fig. 6.8b are indistinguishable from those obtained from circuit 5.1 which was used to fit all the impedances in this work.

If the adsorption of hydroxide is assumed to be an irreversible adsorption reaction as in eq. 6.4, then the peak current density may be estimated using eq. 6.5 [122].

$$Ni + OH^- \rightarrow Ni - OH(ads) \tag{6.4}$$

$$j_p = \left(\frac{\sigma_m (1-\beta) F}{\exp(1) RT} \right) v \tag{6.5}$$

where j_p is the peak current density at a sweep rate v (5 mV s^{-1}), β is the symmetry factor (assumed to be 0.5 here) and σ_m is 514 μC cm^{-2}.

The j_p obtained from this analysis was 18 μA cm^{-2}. This value is similar to the peak density 11 $\pm$ 4 μA cm^{-2}, obtained in this work. This suggests that the adsorption model is a plausible approximation of the nature of the surface film. Hence the adsorption model was accepted.

6.2.3 Reduction of β-$Ni(OH)_2$ and surface blocking

Earlier, the interconversion of α- to β-$Ni(OH)_2$ was studied using cyclic voltammetry (fig. 6.1 and fig. 6.2) and capacitance (fig. 6.3 and fig. 6.6). On face value both methods show the same information. In summary, α-$Ni(OH)_2$ was converted to β-$Ni(OH)_2$ between 0.5 V and 1.0 V but was only reduced completely once the potential was held at -0.2 V or lower. When the potential was held at -0.1 V or simply swept to -0.15 V, the β-$Ni(OH)_2$ persisted. In the case of α-$Ni(OH)_2$ that was formed below 0.6 V, sweeping the potential to -0.15 V was sufficient to regenerate the species in subsequent sweeps without any need for holding.

However, the capacitance offers additional information about the mechanism of reduction of β-Ni(OH)$_2$ which cannot be obtained using cyclic voltammetry. Initially, the capacitance decreased to 15 $\pm$ 4 μF cm^{-2} around 0.6 V, as the Ni(OH)$_2$ coverage increased (Table 6.2). However, it is equally important to note that during the cathodic scan, the capacitance plateau was maintained until 0 V. When the hold potential was kept $<$ 0.6 V in the previous anodic scan, the capacitance increased to 45 $\pm$ 1 μF cm^{-2} between 0 V and -0.15 V (fig. 6.3a). Recall that at this potential, no significant α- to β-Ni(OH)$_2$ conversion is expected. Hence, α-Ni(OH)$_2$ dominates.

On the other hand, when the potential was held at 0.8 V or 1.0 V in the previous anodic scan, the capacitance only increased to 29 μFcm^{-2} and 16 μFcm^{-2} respectively at -0.15 V in the subsequent cathodic scan. This suggests that the mechanisms of reduction of the α-Ni(OH)$_2$ formed below 0.6 V and the β-Ni(OH)$_2$ formed at higher potentials are different.

Since the formation of α-Ni(OH)$_2$ on the bare nickel substrate resulted in an increase in capacitance at 0.2 V, by extension, the increase in capacitance between 0 V and -0.15 V is probably due to a separate adsorption phenomenon. Hence, hydrogen adsorption on nickel metal substrate was proposed. Since α-Ni(OH)$_2$ reduces in this potential range (fig. 6.1a, fig. 6.1b, fig. 6.3a and fig. 6.5a), it is assumed that it reduces prior to the adsorption of hydrogen. However, when covered by β-Ni(OH)$_2$, the capacitance hardly increases between 0 V and -0.15 V (fig. 6.3b, fig. 6.3c). This suggests that β-Ni(OH)$_2$ saturates or blocks the surface in this potential range thereby preventing the adsorption of hydrogen unto the nickel substrate. Nonetheless, the hydrogen evolution current increased between 0 V and -0.15 V (figs. 6.1b-d and figs. 6.2a-c) compared to its value when α-Ni(OH)$_2$ was present (fig. 6.1a). This not only suggests that hydrogen evolution at β-Ni(OH)$_2$ occurs via a different mechanism to the α phase, it shows β-Ni(OH)$_2$ is more active for hydrogen evolution.

Additionally, fig. 6.2a and fig. 6.3e showed that limiting the hydrogen evolution by holding at -0.1 V resulted in only a partial reduction of β-Ni(OH)$_2$. This suggests

that the reduction of β-Ni$(OH)_2$ occurs in the hydrogen evolution region. Hence, when the potential was held at -0.2 V (Fig. 6.2d and fig. 6.3b), the current densities and capacitances returned to their initial peak values prior to anodic polarization at 0.8 V.

6.2.4 Catalysis of HER by β-Ni$(OH)_2$

Gradually increasing the holding potential from 0.5 V to 0.8 V resulted in an increase in the HER current density at negative potentials (fig. 6.1 a-c and fig. 6.2 a-b). Additionally, fig. 6.5 shows that the conductance increased in a similar fashion as the initial anodic polarization potential increased. These results show that the generation of more monolayers of β-Ni$(OH)_2$ at higher anodic potentials is linked to the increase in hydrogen evolution acitivity.

Fig. 6.5d and fig. 6.2b most vividly depict the differences in the HER activities of α- and β-Ni$(OH)_2$. In fig. 6.5d, the conductance was about three times higher at -0.15 V in the first cycle where β-Ni$(OH)_2$ dominates compared to the second cycle following the reduction of β-Ni$(OH)_2$ at -0.25 V. Similarly, in fig. 6.2b the current at -0.15 V was about three times higher in the first cycle after holding at 0.8 V compared to the second cycle following the reduction of the β phase at -0.2 V. This implies that the hydrogen evolution was three times faster when the surface was saturated by β-Ni$(OH)_2$.

The increase in the HER current density seems to stall after holding at 1 V (fig. 6.1d and fig. 6.2c). In fact, the current density either remained the same or decreased. Note that it still remained higher compared to experiments where the potential was held at 0.5 V (Table 6.3). Note that in table 6.3, the current densities (j) * and ** shown for the potential hold at 1 V were taken from fig. 6.1d and fig. 6.2c respectively. Similarly, the peak capacitances (C_p) during the anodic sweep were taken from fig. 6.3c (*) and fig. 6.3d (**). The current densities (j) at -0.15 V were also compared

Initial holding potential / V	**0.5**	**0.6**	**0.8**	**1.0**
j at -0.15 V / μAcm^{-2} (first cycle)	-53	-92	-209	-58*, -77**
C_{p} during first cycle / μFcm^{-2}	120±5	126±5	135±4	126±4*, 136 ± 4**
C_{p} during second cycle / μFcm^{-2}	126±5	131±5	101±4	36±2*, 112±5**

Table 6.3: Comparison of trends in current density and capacitance. C_{p} is the maximum value of the capacitance for the α-Ni(OH)$_2$ peak.

to show the increase in HER activity with initial holding potential.

Two possibilities are suggested in order to explain these results. One is that the β-Ni(OH)$_2$ is being further oxidized at 1 V to a species which is less active for hydrogen evolution. The other possibility is that bubble coverage as a result of hydrogen evolution at the electrode limited the active surface area during the measurements.

The first possibility is highly unlikely for two reasons. From fig. 6.1d and fig. 6.2c, there is no evidence that another redox reaction is emerging. In fact, the conversion of β-Ni(OH)$_2$ to β-NiOOH does not begin until 1.2 V (fig. 1.2). Secondly, fig. 6.3c shows that holding at 1 V resulted in the biggest decrease in the peak capacitance in the second cycles. Hence, although cyclic voltammetry results shows a reduction in current density, from the capacitance it is evident that more β-Ni(OH)$_2$ was formed at 1 V.

The second possibility is more likely but is more difficult to estimate. Bubble adhesion during the hydrogen evolution may decrease in the electrochemically active surface area and hinder mass transport [123]. Consequently, this may result in a decrease in the current density measured. Since more monolayers of β-Ni(OH)$_2$ were formed at 1 V, the catalysis of the HER, and hence bubble formation at the electrode, is expected to be more vigorous. The departure of the trend of the HER current at 1 V as fig. 6.1d and fig. 6.2c show, suggests that the current is being impeded.

6.2.5 Proposed mechanism for the reduction of β-Ni(OH)$_2$

Elsewhere, stronger hydrogen bonding interactions were observed between the adsorbed OH^- groups of β-Ni(OH)$_2$ and the surrounding water molecules (HER reactants) compared to α-Ni(OH)$_2$ [26]. Separately, Floner et al. proposed that the H_2 electrooxidation was dependent on the coverage of OH(ads) between 0 V and 0.2 V. Hence they proposed eq. 6.6 to explain their observations [54]. While their suggestion that new nickel sites were being generated during the initial stages of anodic polarization is difficult to justify, the relationship between $Ni - OH(ads)$ coverage and hydrogen adsorption is applicable here to the reduction of β-Ni(OH)$_2$. Note that, β-Ni(OH)$_2$ was treated as though it were two OH(β) adsorbed on the nickel substrate. Here, this was represented as $Ni - OH(ads)$.

$$Ni - OH(ads) + Ni - H(ads) \rightarrow 2Ni + H_2O \tag{6.6}$$

During the reduction of α-Ni(OH)$_2$, desorption of OH^- is fast and probably occurs first since holding at negative potential was not required (fig. 6.1a and b). Subsequently, hydrogen is adsorbed prior to hydrogen evolution [26, 48, 54]. Hence, unoccupied nickel sites catalyze the HER. However for β-Ni(OH)$_2$, its reduction is slow (fig. 6.6b). Therefore, it is proposed here that the adsorption of hydrogen probably occurs first, since capacitance retains its minimum value of 15 ± 4 μFcm^{-2} throughout the cathodic sweep when the potential is held at > 0.6 V. This is based on the assumption that the increase in capacitance at negative potentials is due to hydrogen adsorption.

Fig. 6.6a and b show that the time constant for the conversion of α- to β-Ni(OH)$_2$ at 0.8 V is about 1.5 times slower than the reduction of β-Ni(OH)$_2$ at -0.2 V. Despite the slow reduction of β-Ni(OH)$_2$, the HER evidently proceeds at a much faster rate. Therefore, a separate mechanism must be proposed to account for the apparent surface blocking and the subsequent increase in HER current.

Additionally, figs. 6.6b and c show that the capacitance increased when the potential was held at -0.1 V or -0.2 V. Based on prior knowledge, it was assumed that $Ni(OH)_2$ was reduced by holding at these potentials thereby making new nickel sites available for hydrogen adsorption.

The following mechanism is proposed for the reduction of β-$Ni(OH)_2$ (-0.1 V$< E <$ -0.25 V in 0.5 M KOH at 5 mV s^{-1}) and its relationship to hydrogen evolution;

$$Ni - OH(ads) + H_2O + 2e^- \rightarrow Ni - H(ads) + 2OH^- \quad \text{"Volmer"} \tag{6.7}$$

$$2Ni - H(ads) \rightarrow 2Ni + H_2 \quad \text{Tafel} \tag{6.8}$$

$$Ni - H(ads) + H_2O + e^- \rightarrow Ni + H_2 + OH^- \quad \text{Heyrovsky} \tag{6.9}$$

The adsorption of hydrogen in the modified Volmer step is assumed to be rate determining due to the blocking effect of β-$Ni(OH)_2$ (eq. 6.7). Additionally, the reduction of $Ni - OH(ads)$ may also occur via eq. 6.6.

6.2.6 Limitations of this work

The impedance spectra between 0.6 V and 1.0 V only show the beginning of a semicircle. Fitting the impedance to circuit 5.1 (RCR) assumes that the impedance goes on to form a semicircle (like fig. 3.7). However, this is not the only possibility. Processes such as adsorption which cannot be modelled by a resistor may also appear at low frequencies.

Conceptually, the polarization resistance is the impedance at zero frequency [104], which is essentially DC. Hence, the slope of the voltammogram (dj/dE) should be equal to the conductance if all the processes occuring at lower frequencies were captured by the polarization resistance.

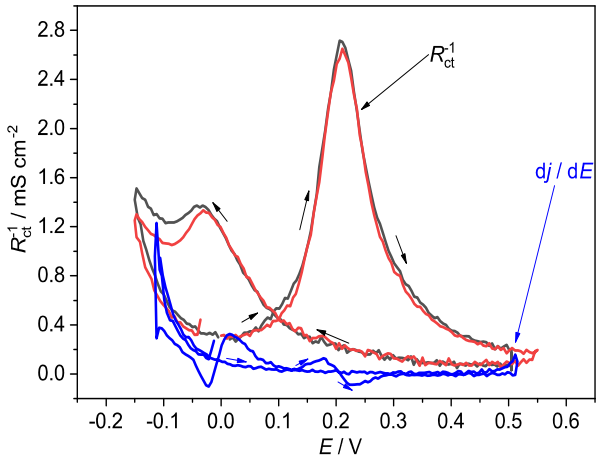

Figure 6.9: Comparison of R_{ct}^{-1} and $\mathrm{d}j/\mathrm{d}E$ between -0.15 V and 0.55 V in 0.5 M KOH at 5 mV s^{-1}.

$$\frac{\mathrm{d}j}{\mathrm{d}E} = \frac{1}{R_{\mathrm{p}}} \tag{6.10}$$

Fig. 6.9 shows that this relationship does not hold true for the data presented in this work. This implies that some slower processes occur at much lower frequencies than the 1 Hz base frequency used in this work. However, going to even lower frequencies may be impractical with dEIS considering the lowest frequency is dictated by the sweep rate. In theory, a sweep rate of 1 mV s^{-1} would allow the user to lower the frequency to 0.1 Hz. However, several disadvantages become apparent. Naturally, data acquisition time will increase. It may also be difficult to maintain the stationarity of the system. Other factors such as impurities in solution which would not be a problem at higher sweep rates may start to affect the quality of the data.

6.2.7 Coverage and surface area correction

As long as one monolayer of $Ni(OH)_2$ persists, 514 $\mu C\ cm^{-2}$, while flawed, models the coverage of the surface oxide adequately. However, as the coverage increases beyond the first monolayer, surface reconstruction is expected [34, 100, 101, 124, 125]. Aptly, as many as 6.5 monolayers were found by Simpraga and Conway at 0.6 V in 0.5 M NaOH (20 mV s^{-1}) [65]. Seyeux et al. characterized oxide nanocrystals forming on Ni (111) using in situ STM. The formation of $Ni(OH)_2$ (001) (hexagonal) in the initial stages of Ni(111) oxidation in 0.1 M NaOH hints at the inadequacy of normalization of using an unreconstructed unit cell [100,101,125]. In that experiment, they measured the lattice parameter of the layer formed and found that 1 ML of that $Ni(OH)_2$ (001) structure would correspond to 367 $\mu C\ cm^{-2}$. They found that 1.6 ML of this structure formed at ca. 0.4 V in 0.1 M NaOH [101]. Furthermore, strong repulsion is expected between electronegative adsorbates [126]. This translates to an expansion of the lattice for the surface layer relative to the bulk phase.

Calculation of the charge density for 1 ML of the (001) hexagonal plane of α-$Ni(OH)_2$ gives 390 $\mu C\ cm^{-2}$ ($a = b = 3.08$ Å) if two electrons per Ni is assumed, with two nickel atoms occupying the unit cell [1, 101] [101]. This calculated value is close to charge density 367 $\mu C\ cm^{-2}$ ($a = b = 3.17$ Å) measured by Seyeux and coworkers and attributed to β-$Ni(OH)_2$ layers [100, 101]. Note that the major reason for the difference in the calculated charge densities is the 0.05 Å contraction of α-$Ni(OH)_2$ and the resulting decrease in its a lattice parameter compared to β-$Ni(OH)_2$ as previously described [1, 19].

Further characterization is required to ascertain the nature of the surface phase. Naturally, other factors such as sweep rate and polarization time affect the thickness of the film. Comparison of 367 $\mu C\ cm^{-2}$ for the surface structure to 514 $\mu C\ cm^{-2}$ (the common literature assumption described earlier) suggests that a revision of the assumptions about the charge density for 1 ML of $Ni(OH)_2$ is required.

However, most of the arguments and conclusions of this thesis do not rely on the exact charge for 1 ML and would be unaffected by revision.

Integration

The ECSA was determined by dividing the anodic charge integrated (up to 0.5 V) by 514 μC cm^{-2} based on previously established methods [36]. However, the integration of the anodic charge to 0.5 V here is clearly arbitrary since the position of the α-Ni(OH)$_2$ peak changes depending on the sweep rate. Furthermore, considering that in the negative-going sweep, residual anodic current is not included in the integration as fig. 6.10 shows, leads to additional inaccuracy in the estimation of charge enclosed by the peak. This error has been estimated to be about 5-10% when the residual anodic charge is included.

Additionally, table 6.2 shows that hydrogen adsorption may contribute significantly to the anodic current, once the potential is scanned through negative potentials. However, this effect is less significant at faster sweep rates (100 mV s^{-1}) [36].

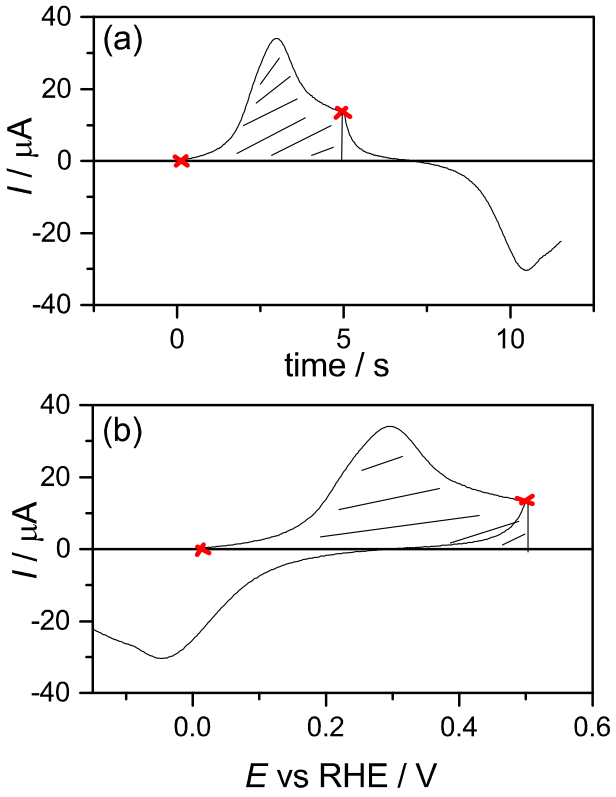

Figure 6.10: Anodic charge integration without double layer correction for nickel cyclic voltammetry in 0.5 M KOH at 100 mV s^{-1}. Shading shows the integrated region.

Chapter 7

Conclusions and future work

7.1 Conclusions

Conventionally, EIS and cyclic voltammetry are performed as separate experiments. However, dEIS significantly decreases the acquisition time required by collecting the data simultaneously. The cyclic voltammograms obtained for the electrooxidation of nickel in this work are comparable to those which already exist elsewhere. However, the capacitances and charge transfer resistances extracted from the impedance spectra provided additional information about the surface kinetics which would otherwise have remained obscure. In this work, the interconversion of nickel hydroxides between -0.25 V and 1.0 V was studied using dEIS. The three research questions stated in section 1.3 were investigated and the conclusions drawn are discussed in the next three paragraphs.

Firstly, this work investigated the conversion of α- to β-$Ni(OH)_2$ between 0.6 and 1.0 V. This potential region is characterized by a small current. The study of the transient current obtained during a potential hold in this region provides little information about the changing state of the surface species. In this work the additional information obtained from the impedance was used to explain the surface processes

which may occur between 0.6 and 1.0 V. It was found that the conversion of α- to β-$Ni(OH)_2$ between 0.6 and 1.0 V proceeds at a faster rate as the potential is increased. A decrease in the peak capacitance in the subsequent cycle as the hold potential in the first cycle is increased from 0.6 V to 1.0 V shows that α- to β-$Ni(OH)_2$ conversion proceeds throughout this potential region. Subsequently, the β-$Ni(OH)_2$ formed catalyzes the HER. Therefore, higher HER current was observed after holds between 0.6 V and 1.0 V compared to 0.5 V.

Secondly, this work sought to study the mechanism of reduction of β-$Ni(OH)_2$ and its catalysis of the HER. Previously, the reduction of β-$Ni(OH)_2$ was often erroneously described as following the same mechanism as the reduction of α-$Ni(OH)_2$. In this work, the dependence of the capacitance between 0 V and -0.15 V on the initial anodic hold potential was used to show that β-$Ni(OH)_2$ reduces via a different mechanism compared to α-$Ni(OH)_2$. The retention of low capacitance values at -0.15 V after holding at > 0.6 V confirms that the slow reduction of β-$Ni(OH)_2$ affects the adsorption of hydrogen. Here, a reaction between NiH(ads) and NiOH(ads) is proposed as the rate determining step for hydrogen evolution at β-$Ni(OH)_2$.

Thirdly, this work sought to extract time constants related to the kinetics of interconversion of $Ni(OH)_2$. Previously, no time constants were proposed in the literature. Therefore, the understanding of the kinetics of interconversion of $Ni(OH)_2$ was limited. In this work, time constants related to the kinetics of interconversion of $Ni(OH)_2$ were successfully extracted. Fitting the current revealed that the processes at -0.2 V were 1.5 times slower than the α- to β-$Ni(OH)_2$ transformation at 0.8 V. This behavior points to a slow reaction inhibiting the HER rate.

However, some limitations were apparent in this work. Comparison of the conductance and the slope of the voltammogram between -0.15 V and 0.5 V at 5 mV s^{-1} suggests that there are slower processes at lower frequencies which were not captured due to the frequency range used (1 Hz to 13 kHz). This limitation presents great opportunities for future work. Nonetheless, the information gathered in this work using

dEIS enhances the understanding of the interconversion of nickel hydroxides beyond what is known in the literature before now. The study of interconversion of nickel hydroxides is arguably one of the more challenging systems dEIS could have been tested on. Therefore, at the very least the great potential of dEIS for the study of surface kinetics has been demonstrated. Additionally, for systems with faster time constants than the interconversion of nickel hydroxides (15-30 seconds), it is anticipated that more detailed analysis of the kinetics may be accessible through dEIS.

7.2 Recommendations

Model circuits were used to study the fastest decay which can be measured during a potential hold in the 1 Hz to 13 kHz frequency range using dEIS. In this system, the frequency range limited the information which could be learned from the impedance spectra obtained for the circuits with slower time constants (models A and B). In the study of the interconversion of nickel hydroxides, it was evident that some slower processes were missed at lower frequencies than the 1 Hz base frequency used in this work. These limitations in both studies suggest that the conditions used in this work need to be optimized to allow for measurements to lower frequencies when needed. For example, the effect of slower sweep rates (than the 5 mV s^{-1} used in this work) may be explored.

On the study of the interconversion of nickel hydroxides, the accurate determination of the ECSA is a stumbling block for interpreting electrochemical studies. The application of in situ techniques may further improve the understanding of the structure of the $Ni(OH)_2$ / NiO layer at different potentials.

References

[1] D. S. Hall, D. J. Lockwood, C. Bock, and B. R. MacDougall, *Proceedings of the Royal Society A: Mathematical, Physical and Engineering Sciences*, 2015, **471**(2174), 20140792.

[2] G. Halpert, *Journal of Power Sources*, 1984, **12**(3-4), 177–192.

[3] ed. C. Daniel and J. O. Besenhard, *Handbook of Battery Materials*, Wiley-VCH Verlag GmbH & Co. KGaA, 2011.

[4] C. S. Yudha, S. U. Muzayanha, H. Widiyandari, F. Iskandar, W. Sutopo, and A. Purwanto, *Energies*, 2019, **12**(10), 1886.

[5] M. Kiani, M. Mousavi, and S. Ghasemi, *Journal of Power Sources*, 2010, **195**(17), 5794–5800.

[6] M. Aghazadeh, M. Ghaemi, B. Sabour, and S. Dalvand, *Journal of Solid State Electrochemistry*, 2014, **18**(6), 1569–1584.

[7] Y. Wang, L. Yu, and Y. Xia, *Journal of The Electrochemical Society*, 2006, **153**(4), A743.

[8] J. H. Park, O. O. Park, K. H. Shin, C. S. Jin, and J. H. Kim, *Electrochemical and Solid-State Letters*, 2002, **5**(2), H7.

[9] J. Ran, J. Yu, and M. Jaroniec, *Green Chemistry*, 2011, **13**(10), 2708.

[10] M. Gao, W. Sheng, Z. Zhuang, Q. Fang, S. Gu, J. Jiang, and Y. Yan, *Journal of the American Chemical Society*, 2014, **136**(19), 7077–7084.

[11] S. I. Cordoba-Torresi, *Journal of The Electrochemical Society*, 1991, **138**(6), 1548.

[12] H. Bode, K. Dehmelt, and J. Witte, *Electrochimica Acta*, 1966, **11**(8), 1079–1087.

[13] P. Oliva, J. Leonardi, J. Laurent, C. Delmas, J. Braconnier, M. Figlarz, F. Fievet, and A. Guibert, *Journal of Power Sources*, 1982, **8**(2), 229–255.

[14] Y. Mo, *Journal of The Electrochemical Society*, 1996, **143**(1), 37.

[15] M. Dmochowska and A. Czerwiski, *Journal of Solid State Electrochemistry*, 1998, **2**(1), 16–23.

[16] T. Ohligschläger and G. Schwitzgebel, *Physical Chemistry Chemical Physics*, 2001, **3**(23), 5290–5296.

[17] S. L. Medway, C. A. Lucas, A. Kowal, R. J. Nichols, and D. Johnson, *Journal of Electroanalytical Chemistry*, 2006, **587**(1), 172–181.

[18] M. E. Lyons and M. P. Brandon, *International Journal of Electrochemical Science*, 2008, **3**(12), 1425–1462.

[19] K. I. Pandya, W. E. O'Grady, D. A. Corrigan, J. McBreen, and R. W. Hoffman, *Journal of Physical Chemistry*, 1990, **94**(1), 21–26.

[20] M. Grdeń, K. Klimek, and A. Czerwiński, *Journal of Solid State Electrochemistry*, 2004, **8**(6), 390–397.

[21] R. S. McEwen, *The Journal of Physical Chemistry*, 1971, **75**(12), 1782–1789.

[22] C. Faure, C. Delmas, and M. Fouassier, *Journal of Power Sources*, 1991, **35**(3), 279–290.

[23] J. Y. Huot and L. Brossard, *International Journal of Hydrogen Energy*, 1987, **12**(12), 821–830.

[24] Y. Choquette, L. Brossard, and H. Menard, *International Journal of Hydrogen Energy*, 1990, **15**(8), 551–555.

[25] K. Schultze and H. Bartelt, *International Journal of Hydrogen Energy*, 1992, **17**(9), 711–718.

[26] X. Yu, J. Zhao, L. R. Zheng, Y. Tong, M. Zhang, G. Xu, C. Li, J. Ma, and G. Shi, *ACS Energy Letters*, 2018, **3**(1), 237–244.

[27] T. Holm and D. A. Harrington, *ECS Transactions*, 2018, **85**(12), 167–176.

[28] D. A. Harrington, *Journal of Electroanalytical Chemistry*, 1993, **355**(1-2), 21–35.

[29] R. L. Sacci and D. Harrington In *ECS Transactions*. ECS, 2009.

[30] J. L. Ord, *Surface Science*, 1976, **56**(C), 413–424.

[31] W. Visscher and E. Barendrecht, *Electrochimica Acta*, 1980, **25**(5), 651–655.

[32] L. Burke and T. Twomey, *Journal of Electroanalytical Chemistry and Interfacial Electrochemistry*, 1984, **162**(1-2), 101–119.

[33] L. M. De Souza, F. P. Kong, F. R. McLarnon, and R. H. Muller, *Electrochimica Acta*, 1997, **42**(8), 1253–1267.

[34] B. Beden, D. Floner, J. Léger, and C. Lamy, *Surface Science*, 1985, **162**(1-3), 822–829.

[35] J. Van Drunen, B. Kinkead, M. C. Wang, E. Sourty, B. D. Gates, and G. Jerkiewicz, *ACS Applied Materials and Interfaces*, 2013, **5**(14), 6712–6722.

[36] M. Alsabet, M. Grden, and G. Jerkiewicz, *Electrocatalysis*, 2011, **2**(4), 317–330.

[37] M. Alsabet, M. Grden, and G. Jerkiewicz, *Electrocatalysis*, 2014, **5**(2), 136–147.

[38] I. Faria, R. Torresi, and A. Gorenstein, *Electrochimica Acta*, 1993, **38**(18), 2765–2771.

[39] G. T. Cheek and W. E. O'Grady, *Journal of Electroanalytical Chemistry*, 1997, **421**(1-2), 173–177.

[40] H.-W. Hoppe and H.-H. Strehblow, *Surface and Interface Analysis*, 1989, **14**(3), 121–131.

[41] W. Paik and Z. Szklarska-Smialowska, *Surface Science*, 1980, **96**(1-3), 401–412.

[42] A. Pshenichnikov, L. Burkaltseva, and Z. Kudryavtseva, *Electrochimica Acta*, 2000, **45**(25-26), 4143–4150.

[43] C. A. Melendres and M. Pankuch, *Journal of Electroanalytical Chemistry*, 1992, **333**(1-2), 103–113.

[44] A. Audemer, *Journal of The Electrochemical Society*, 1997, **144**(8), 2614.

[45] J. Desilvestro, *Journal of The Electrochemical Society*, 1988, **135**(4), 885.

[46] M. Aghazadeh, A. N. Golikand, and M. Ghaemi, *International Journal of Hydrogen Energy*, 2011, **36**(14), 8674–8679.

[47] J. L. Bantignies, S. Deabate, A. Righi, S. Rols, P. Hermet, J. L. Sauvajol, and F. Henn, *Journal of Physical Chemistry C*, 2008, **112**(6), 2193–2201.

[48] A. Lasia and A. Rami, *Journal of Electroanalytical Chemistry and Interfacial Electrochemistry*, 1990, **294**(1-2), 123–141.

[49] A. Rami and A. Lasia, *Journal of Applied Electrochemistry*, 1992, **22**(4), 376–382.

[50] L. Birry and A. Lasia, *Journal of Applied Electrochemistry*, 2004, **34**(7), 735–749.

[51] A. Lasia, *Journal of Electroanalytical Chemistry*, 1989, **266**(1), 57–68.

[52] E. A. Franceschini, G. I. Lacconi, and H. R. Corti, *Electrochimica Acta*, 2015, **159**, 210–218.

[53] G. Kreysa, B. Hakansson, and P. Ekdunge, *Electrochimica Acta*, 1988, **33**(10), 1351–1357.

[54] D. Floner, C. Lamy, and J.-M. Leger, *Surface Science*, 1990, **234**(1-2), 87–97.

[55] F. Hahn, D. Floner, B. Beden, and C. Lamy, *Electrochimica Acta*, 1987, **32**(11), 1631–1636.

[56] G. Briggs and P. Snodin, *Electrochimica Acta*, 1982, **27**(5), 565–572.

[57] A. A. Wronkowska, *Surface Science*, 1989, **214**(3), 507–522.

[58] R. S. Schrebler Guzmán, J. R. Vilche, and A. J. Arvía, *Corrosion Science*, 1978, **18**(8), 765–778.

[59] M. M. Jaksic, J. Brun, B. Johansen, and R. Tunold, *International Journal of Hydrogen Energy*, 1995, **20**(4), 265–273.

[60] Z. I. Kudryavtseva, L. A. Burkaltseva, and A. G. Pshenichnikov, *Russian Journal of Electrochemistry*, 2004, **40**(11), 1208–1213.

[61] M. Grdeń and K. Klimek, *Journal of Electroanalytical Chemistry*, 2005, **581**(1), 122–131.

[62] M. J. Madou, *Journal of The Electrochemical Society*, 1983, **130**(5), 1056.

[63] G. Barral, F. Njanjo-Eyoke, and S. Maximovitch, *Electrochimica Acta*, 1995, **40**(17), 2815–2828.

[64] W. Visscher and E. Barendrecht, *Surface Science*, 1983, **135**(1-3), 436–452.

[65] R. Simpraga and B. Conway, *Journal of Electroanalytical Chemistry and Interfacial Electrochemistry*, 1990, **280**(2), 341–357.

[66] D. S. Hall, C. Bock, and B. R. MacDougall, *Journal of The Electrochemical Society*, 2013, **160**(3), F235–F243.

[67] B. MacDougall and M. Cohen, *Journal of The Electrochemical Society*, 1974, **121**(9), 1152.

[68] P. V. Kamath, *Journal of The Electrochemical Society*, 1994, **141**(11), 2956.

[69] R. Barnard, G. T. Crickmore, J. A. Lee, and F. L. Tye, *Journal of Applied Electrochemistry*, 1980, **10**(1), 61–70.

[70] X. Wang, H. Luo, P. V. Parkhutik, A. C. Millan, and E. Matveeva, *Journal of Power Sources*, 2003, **115**(1), 153–160.

[71] G. Larramona, *Journal of The Electrochemical Society*, 1990, **137**(2), 428.

[72] M. Gonsalves and A. R. Hillman, *Journal of Electroanalytical Chemistry*, 1998, **454**(1-2), 183–202.

[73] B. Payne, M. Biesinger, and N. McIntyre, *Journal of Electron Spectroscopy and Related Phenomena*, 2009, **175**(1-3), 55–65.

[74] N. Kitakatsu, V. Maurice, C. Hinnen, and P. Marcus, *Surface Science*, 1998, **407**(1-3), 36–58.

[75] A. P. Grosvenor, M. C. Biesinger, R. S. Smart, and N. S. McIntyre, *Surface Science*, 2006, **600**(9), 1771–1779.

[76] B. P. Payne, A. P. Grosvenor, M. C. Biesinger, B. A. Kobe, and N. S. McIntyre, *Surface and Interface Analysis*, 2007, **39**(7), 582–592.

[77] M. C. Biesinger, B. P. Payne, L. W. Lau, A. Gerson, and R. S. C. Smart, *Surface and Interface Analysis*, 2009, **41**(4), 324–332.

[78] M. Rajamathi, G. N. Subbanna, and P. V. Kamath, *Journal of Materials Chemistry*, 1997, **7**(11), 2293–2296.

[79] I. Hotovy, J. Huran, and L. Spiess, *Journal of Materials Science*, 2004, **39**(7), 2609–2612.

[80] M.-S. Kim, *Journal of The Electrochemical Society*, 1998, **145**(2), 507.

[81] C. Tessier, *Solid State Ionics*, 2000, **133**(1-2), 11–23.

[82] G. X. Tong, F. T. Liu, W. H. Wu, J. P. Shen, X. Hu, and Y. Liang, *CrystEngComm*, 2012, **14**(18), 5963–5973.

[83] P. Hermet, L. Gourrier, J. L. Bantignies, D. Ravot, T. Michel, S. Deabate, P. Boulet, and F. Henn, *Physical Review B - Condensed Matter and Materials Physics*, 2011, **84**(23), 1–10.

[84] L. Guerlou-Demourgues and C. Delmas, *Journal of Power Sources*, 1994, **52**(2), 275–281.

[85] M. Rajamathi and P. V. Kamath, *Journal of Power Sources*, 1998, **70**(1), 118–121.

[86] M. B. Freitas, *Journal of Power Sources*, 2001, **93**(1-2), 163–173.

[87] S. Deabate, F. Henn, S. Devautour, and J. C. Giuntini, *Journal of The Electrochemical Society*, 2003, **150**(6), J23.

[88] D. S. Hall, D. J. Lockwood, S. Poirier, C. Bock, and B. R. MacDougall, *ACS Applied Materials & Interfaces*, 2014, **6**(5), 3141–3149.

[89] B. Mani, *Journal of The Electrochemical Society*, 1988, **135**(4), 800.

[90] D. S. Hall, D. J. Lockwood, S. Poirier, C. Bock, and B. R. MacDougall, *Journal of Physical Chemistry A*, 2012, **116**(25), 6771–6784.

[91] W. Visscher and E. Barendrecht, *Journal of Electroanalytical Chemistry and Interfacial Electrochemistry*, 1983, **154**(1-2), 69–80.

[92] L. Chen, *Journal of The Electrochemical Society*, 1991, **138**(11), 3321.

[93] B. E. Conway, M. A. Sattar, and D. Gilroy, *Electrochimica Acta*, 1969, **14**(8), 711–724.

[94] S. Trasatti and O. A. Petrii, *Pure and Applied Chemistry*, 1991, **63**(5), 711–734.

[95] D. S. Hall, C. Bock, and B. R. MacDougall, *Journal of The Electrochemical Society*, 2014, **161**(12), H787–H795.

[96] M. Lukaszewski, M. Soszko, and A. Czerwiński, *International Journal of Electrochemical Science*, 2016, **11**(6), 4442–4469.

[97] M. Dupont, A. F. Hollenkamp, and S. W. Donne, *Electrochimica Acta*, 2013, **104**, 140–147.

[98] S. A. Machado and L. A. Avaca, *Electrochimica Acta*, 1994, **39**(10), 1385–1391.

[99] J. L. Weininger and M. W. Breiter, *Journal of The Electrochemical Society*, 1963, **110**(6), 484.

[100] A. Seyeux, V. Maurice, L. H. Klein, and P. Marcus, *Journal of Solid State Electrochemistry*, 2005, **9**(5), 337–346.

[101] A. Seyeux, V. Maurice, L. H. Klein, and P. Marcus, *Journal of The Electrochemical Society*, 2006, **153**(11), B453.

[102] L. Bai, D. A. Harrington, and B. E. Conway, *Electrochimica Acta*, 1987, **32**(12), 1713–1731.

[103] J. C. Ho and D. L. Piron, *Journal of Applied Electrochemistry*, 1996, **26**(5), 515–521.

[104] A. Lasia, *Electrochemical Impedance Spectroscopy and its Applications*, Springer New York, 2014.

[105] M. E. Orazem and B. Tribollet, *Electrochemical Impedance Spectroscopy*, John Wiley & Sons, Inc., 2008.

[106] C.-T. Chen, *Linear System Theory and Design*, Oxford University Press, Inc., USA, 3rd ed., 1998.

[107] D. D. Macdonald, *Electrochimica Acta*, 2006, **51**(8-9), 1376–1388.

[108] A. S. Bandarenka, *The Analyst*, 2013, **138**(19), 5540.

[109] R. L. Sacci, F. Seland, and D. A. Harrington, *Electrochimica Acta*, 2014, **131**, 13–19.

[110] G. S. Popkirov and R. N. Schindler, *Review of Scientific Instruments*, 1993, **64**(11), 3111–3115.

[111] J. Garland, C. Pettit, and D. Roy, *Electrochimica Acta*, 2004, **49**(16), 2623–2635.

[112] S. O. Engblom, J. C. Myland, K. B. Oldham, and A. L. Taylor, *Electroanalysis*, 2001, **13**(8-9), 626–630.

[113] B. A. Boukamp, *Journal of The Electrochemical Society*, 1995, **142**(6), 1885.

[114] D. A. Harrington, Complex nonlinear least squares fitting of immittance data https://www.maplesoft.com/applications/view.aspx?SID=154540, 2019.

[115] J. Macdonald, J. Schoonman, and A. Lehnen, *Journal of Electroanalytical Chemistry and Interfacial Electrochemistry*, 1982, **131**, 77–95.

[116] P. R. Bevington and D. K. Robinson, *Data reduction and error analysis for the physical sciences*, McGraw-Hill, Boston, 2003.

[117] M. Ingdal, R. Johnsen, and D. A. Harrington, *Electrochimica Acta*, 2019, **317**, 648–653.

[118] G. Glatting, P. Kletting, S. N. Reske, K. Hohl, and C. Ring, *Medical Physics*, 2007, **34**(11), 4285–4292.

[119] F. Ciucci, *Current Opinion in Electrochemistry*, 2019, **13**, 132–139.

[120] K. V. Rao and A. Smakula, *Journal of Applied Physics*, 1965, **36**(6), 2031–2038.

[121] A. Kashir, H.-W. Jeong, G.-H. Lee, P. Mikheenko, and Y. H. Jeong, *Journal of the Korean Physical Society*, 2019, **74**(10), 984–988.

[122] S. Srinivasan and E. Gileadi, *Electrochimica Acta*, 1966, **11**(3), 321–335.

[123] Y. Bao, K. Nagasawa, Y. Kuroda, and S. Mitsushima, *Electrocatalysis*, 2020, **11**(3), 301–308.

[124] L. Verheij, J. V. D. Berg, and D. Armour, *Surface Science*, 1979, **84**(2), 408–426.

[125] A. Seyeux, V. Maurice, L. H. Klein, and P. Marcus, *Electrochimica Acta*, 2008, **54**(2), 540–544.

[126] D. Kandaskalov, D. Monceau, C. Mijoule, and D. Connétable, *Surface Science*, 2013, **617**, 15–21.